

Chemical Vapor Deposition Growth of Two-Dimensional Transition Metal
Dichalcogenides and Related Heterostructures

A Dissertation

SUBMITTED TO THE FACULTY OF THE
UNIVERSITY OF MINNESOTA

BY

Zachary Patrick DeGregorio

IN PARTIAL FULFILLMENT OF THE REQUIREMENTS
FOR THE DEGREE OF
DOCTOR OF PHILOSOPHY

Advisor

James E. Johns

September 2018

Copyright © 2018

Zachary Patrick DeGregorio

Acknowledgements

The completion of this dissertation and the research within would not have been possible without the help and support of many people in my life.

I am grateful to my advisor, James, for the immeasurable guidance and knowledge passed down over these five years.

I am grateful to my numerous collaborators, whose work and advice helped open doors I would not have thought possible.

I am grateful to my fellow Johns lab members, past and present, whose helpful suggestions and light-hearted jokes offered refreshing perspectives no one else could. I am especially grateful for the hard work and mentorship of Dr. Youngdong Yoo.

I am grateful to my wife and family for the unconditional love and support. Your care and consideration helped me to feel pride during the brighter times and hope during the dark. It is through your guidance that, during this time, I was able to continue practicing the seven principles that I hold most dear: kindness, compassion, openness, freedom, conscience, peace, and respect.

I am grateful to my friends, new and old, for the years of cheer and camaraderie. It has been said that games are a mirror we hold to life – they reflect the subtle turning of the world, and as such, a well-played game reveals the moving of a mind. There is a beauty to them for those with eyes to see it, and I have been fortunate to be among company with such keen eyes.

Abstract

Two-dimensional (2D) transition metal dichalcogenides (TMDCs) are atomically thin, layered materials with unique physical and electronic properties relative to their bulk forms. Due to these properties, 2D TMDCs show promise for many applications, including catalysis, nanoelectronics, optoelectronics, and spin- and valleytronics. To utilize TMDCs for these applications, they must first be reproducibly isolated. Much previous work in this area has resulted in material batches with low yield, small crystal sizes, and little control over the crystal morphology and orientation. Here, I present the reproducible chemical vapor deposition (CVD) growth of a wide array of 2D TMDCs, including MoS₂, WS₂, MoTe₂, NbS₂, and WSe₂. Control of the growth of these materials is achieved through the optimization of many parameters, including substrate surface chemistry and synthetic growth parameters. Through the optimization of these parameters, I demonstrate control over the resulting material thickness, phase, and morphology.

These high-quality TMDCs are subsequently used to grow many relevant heterostructures, including MoS₂/WS₂ lateral and vertical heterostructures, MoO₂/MoS₂ core/shell plates, 2H-1T' MoTe₂ few-layer homojunctions, and WS₂/NbS₂ lateral heterostructures, and the utility of these heterostructures is assessed. MoS₂/WS₂ heterostructures show promise as a semiconductor-semiconductor heterostructure in which the nature of the alignment is controlled by the initial MoS₂ seed crystal. MoO₂/MoS₂ core/shell plates are freestanding and show epitaxial alignment with the underlying crystal substrate, with potential applications in catalysis. 2H-1T' MoTe₂ few-layer homojunctions are grown using a patternable phase engineering procedure, and devices fabricated from these homojunctions show reduced contact resistance relative to 2H MoTe₂ devices with

noble metal contacts. Finally, WS_2/NbS_2 lateral heterostructures show promise as an alternative metal-semiconductor heterostructure system for creating 2D TMDC devices with low contact resistance. The controlled CVD growth of these materials and heterostructures bolsters their future use for relevant applications.

Table of Contents

Acknowledgements.....	i
Abstract.....	ii
Table of Contents.....	iv
List of Tables.....	viii
List of Figures.....	ix
List of Abbreviations.....	xv
Chapter 1. Introduction.....	1
1.1 Structure and Properties of 2D Materials.....	2
1.1.1 2D Materials History and Definition.....	2
1.1.2 Physical Properties and Applications.....	2
1.1.3 Transition Metal Dichalcogenides.....	3
1.1.4 TMDC Electronic Structure.....	4
1.2 Isolating 2D Materials.....	7
1.2.1 Exfoliation.....	7
1.2.2 Chemical Vapor Deposition.....	9
Chapter 2. Substrate Effects.....	19
2.1 Preface.....	20
2.2 Introduction.....	20

2.2.1 Epitaxy.....	20
2.3 Experimental	24
2.3.1 SiC Passivation.....	24
2.3.2 Sapphire Annealing	25
2.3.3 GaN Polishing.....	26
2.3.4 CVD Growth of MoS ₂ on Various Substrates	27
2.3.5 NbS ₂ CVD Growth	28
2.3.6 WSe ₂ CVD Growth and Selenization.....	30
2.4 Results and Discussion.....	32
2.4.1 SiC Passivation.....	32
2.4.2 Sapphire Annealing	33
2.4.3 GaN Polishing.....	34
2.4.4 CVD Growth of MoS ₂ on Various Substrates	36
2.4.5 NbS ₂ CVD Growth	41
2.4.6 WSe ₂ CVD Growth and Selenization.....	44
2.5 Conclusion.....	46
Chapter 3. 2D Material Semiconductor Heterostructures.....	49
3.1 Preface.....	50
3.2 Introduction.....	50
3.2.1 Semiconductor Heterostructures.....	50

3.2.2 2D Material Heterostructures	51
3.2.3 MoS ₂ /WS ₂ Ultraclean Heterostructures.....	52
3.3 Experimental	53
3.4 Results and Discussion.....	56
3.5 Conclusion.....	74
Chapter 4. MoO ₂ /MoS ₂ Core/Shell Nanoplates.....	75
4.1 Preface.....	76
4.2 Introduction	76
4.3 Experimental	77
4.4 Results and Discussion.....	80
4.5 Conclusion.....	98
Chapter 5. Metal-Semiconductor Heterostructures.....	100
5.1 Preface.....	101
5.2 Introduction	102
5.2.1 Metal-Semiconductor Heterostructures	102
5.2.2 Device Considerations for 2D Materials	103
5.2.3 In-Plane 2H-1T' MoTe ₂ Homojunctions.....	104
5.2.4 2H-1T' MoTe ₂ Devices	106
5.2.5 WS ₂ /NbS ₂ Heterostructures	107
5.3 Experimental	108

5.3.1 In-Plane 2H-1T' MoTe ₂ Homojunctions	108
5.2.2 2H-1T' MoTe ₂ Devices	111
5.2.3 WS ₂ /NbS ₂ Heterostructures	112
5.4 Results and Discussion.....	114
5.4.1 In-Plane 2H-1T' MoTe ₂ Homojunctions.....	114
5.4.2 2H-1T' MoTe ₂ Devices	125
5.4.3 WS ₂ /NbS ₂ Heterostructures	139
5.5 Conclusions and Future Work.....	147
Chapter 6. Conclusions	150
References.....	155
Appendix A.....	170
A.1 HRTEM Diffusion Analysis MATLAB Script	171

List of Tables

Chapter 5. Metal-Semiconductor Heterostructures

Table 5.1. Comparison of 2H and 1T'-2H-1T' device performance	132
--	-----

List of Figures

Chapter 1. Introduction

Figure 1.1. MoS ₂ crystal structure	4
Figure 1.2. Band structures of bilayer and monolayer MoS ₂	6
Figure 1.3. Schematic illustration of the exfoliation process.....	8
Figure 1.4. General mechanism for CVD growth.....	10
Figure 1.5. General CVD setup schematic.....	11
Figure 1.6. Schematic illustration of adatom sites in the TLK model	15
Figure 1.7. Schematic representations of the three main growth modes	17

Chapter 2. Substrate Effects

Figure 2.1. Schematic illustration of epitaxy	22
Figure 2.2. AFM height images of prepared 4H-SiC surfaces.....	33
Figure 2.3. AFM height images of prepared sapphire surfaces	34
Figure 2.4. AFM height images of SiO ₂ /Si, GaN/Si, and single-crystal GaN surfaces	35
Figure 2.5. SEM and AFM images of CVD-grown ML MoS ₂	37
Figure 2.6. CVD growth of MoS ₂ on annealed sapphire	39
Figure 2.7. SEM images of MoS ₂ and MoO ₂ /MoS ₂ growths on 4H-SiC	40
Figure 2.8. NbS ₂ flakes synthesized from the oxide-based CVD method	42

Figure 2.9. NbS ₂ flakes synthesized from the chloride-based CVD method.....	43
Figure 2.10. CVD-grown ML WSe ₂	45
Figure 2.11. ML WSe ₂ after selenization.....	46

Chapter 3. 2D Material Semiconductor Heterostructures

Figure 3.1. Schematic illustrating the band alignment of the three types of semiconductor heterostructures	51
Figure 3.2. Monolayer MoS ₂ crystals synthesized on <i>c</i> -cut sapphire without and with hydrogen gas	57
Figure 3.3. SEM images of monolayer MoS ₂ grown with and without hydrogen.....	58
Figure 3.4. Raman spectra and Lorentz fitting results for monolayer MoS ₂	59
Figure 3.5. In-plane heteroepitaxial WS ₂ /MoS ₂ monolayers synthesized from monolayer MoS ₂ grown with hydrogen.....	60
Figure 3.6. Raman peak position mapping at the 2LA and A ₁ modes of WS ₂ from in-plane heterostructures	62
Figure 3.7. LFM friction image of the WS ₂ /MoS ₂ heterostructure sample shown in Figure 3.3h	63
Figure 3.8. KPFM analysis of in-plane heteroepitaxial WS ₂ /MoS ₂ monolayers	64
Figure 3.9. Z-Contrast HAADF-STEM images of the in-plane heteroepitaxial WS ₂ /MoS ₂ monolayer.....	66

Figure 3.10. Vertical WS ₂ /MoS ₂ heterostructures synthesized from monolayer MoS ₂ grown without hydrogen	68
Figure 3.11. HAADF-STEM imaging of vertical WS ₂ /MoS ₂ heterostructures	69
Figure 3.12. SEM, PL, and Raman analysis of vertical WS ₂ /MoS ₂ heterostructures heterostructures from low-flux conditions with no WS ₂ ribbons	71
Figure 3.13. HRTEM of MoS ₂ /WS ₂ lateral interface and diffusion quantification	73

Chapter 4. MoO₂/MoS₂ Core/Shell Nanoplates

Figure 4.1. Mechanism schematics and Raman spectroscopy of MoO ₂ /MoS ₂ core/shell plates	81
Figure 4.2. Plots of temperature of sulfur boat position and calculated sulfur vapor pressure as a function of time for MoS ₂ monolayer and MoO ₂ /MoS ₂ core-shell plate growths	83
Figure 4.3. Optical image of MoO ₂ /MoS ₂ core-shell plates	85
Figure 4.4. TEM analysis of MoO ₂ /MoS ₂ core/shell plates	86
Figure 4.5. SEM analysis of MoO ₂ /MoS ₂ core/shell plates	88
Figure 4.6. SEM image of MoS ₂ monolayer flakes grown on SiC	89
Figure 4.7. SEM image of MoO ₂ /MoS ₂ core-shell plates on SiO ₂ /Si	90
Figure 4.8. LEED patterns of prepared 4H-SiC and core/shell nanoplate samples	91
Figure 4.9. Low-energy Auger electron spectra with inset high-resolution spectra of MoO ₂ /MoS ₂ core-shell plates grown on various substrates	92

Figure 4.10. Representative EBSD analysis of core/shell nanoplates	94
Figure 4.11. Structural analysis of MoO ₂ /MoS ₂ core/shell plates	95
Figure 4.12. SEM images of MoO ₂ /MoS ₂ core-shell plates that have been pushed flat using another bare SiC substrate.....	96
Figure 4.13. Top-view, two-dimensional schematics illustrate the crystallographic alignment of MoO ₂ (010) and (001) planes with underlying 4H-SiC ($\sqrt{3}\times\sqrt{3}$)R30° surface reconstruction	97
Figure 4.14. Optical image and Raman maps of MoO ₂ /MoTe ₂ core-shell plate	98

Chapter 5. Metal-Semiconductor Heterostructures

Figure 5.1. AFM of Mo nanoislands and in-plane 2H-1T' homojunctions.....	109
Figure 5.2. Schematic illustration of the fabrication procedure for few-layer 2H-1T' MoTe ₂ patterns.....	110
Figure 5.3. Growth of in-plane 2H-1T' MoTe ₂ homojunctions from Mo nanoislands	115
Figure 5.4. AFM of scratched in-plane 2H-1T' MoTe ₂ films	116
Figure 5.5. XRD patterns of few-layer 2H and 1T' MoTe ₂	117
Figure 5.6. XPS survey spectrum of few-layer 2H and 1T' MoTe ₂	118
Figure 5.7. Flux-controlled phase engineering of few-layer MoTe ₂	120
Figure 5.8. Raman spectra and Lorentzian fitting results of few-layer 2H, mixed 2H-1T', 1T', and defective 1T' MoTe ₂	121

Figure 5.9. Raman mapping and KPFM study of in-plane 2H-1T' MoTe ₂ homojunctions.....	123
Figure 5.10. Fabrication of few-layer 2H-1T' MoTe ₂ patterns.....	124
Figure 5.11. Phase conservation of few-layer 1T' MoTe ₂ during annealing with high Te flux.....	125
Figure 5.12. Schematic illustration and Raman mapping of 1T'-2H-1T' MoTe ₂ devices	126
Figure 5.13. Transfer length measurements and device characteristics.....	127
Figure 5.14. Temperature-dependent transport characteristics of 2H-only and 1T'-2H-1T' MoTe ₂ devices	129
Figure 5.15. Hole mobility as a function of temperature for the 2H and 1T'/2H/1T' MoTe ₂ devices in Figure 5.7 at different values of V_{DS}	131
Figure 5.16. Arrhenius plots and bias-dependent effective barrier heights	134
Figure 5.17. Plot of the slopes of the Arrhenius plot for the 2H-only device in Figure 5.7 vs. V_{DS} at $V_{BG} = -100$ V	135
Figure 5.18. Effective Schottky barrier height of 2H and 1T'/2H/1T' MoTe ₂ devices as a function of bias voltage.....	135
Figure 5.19. Calculated band structures of 5-layer 2H MoTe ₂ and 5-layer 1T' MoTe ₂ with spin-orbit coupling included	137

Figure 5.20. Band gap of 2H MoTe ₂ and barrier height at the 2H/1T' interface as a function of layer number.....	138
Figure 5.21. WS ₂ /NbS ₂ lateral heterostructure characterization.....	140
Figure 5.22. AFM and KPFM analysis of WS ₂ /NbS ₂ heterostructures	142
Figure 5.23. Cross-section TEM and PL mapping analysis of the WS ₂ /NbS ₂ interface	144
Figure 5.24. Preliminary device characteristics and investigation of WS ₂ /NbS ₂ heterostructure devices via Raman and PL mapping.....	146

List of Abbreviations

2D	two-dimensional
AES	Auger electron spectroscopy
AFM	atomic force microscopy
CB	conduction band
CBED	convergent beam electron diffraction
CCD	charge-coupled device
CPD	contact potential difference
CVD	chemical vapor deposition
DFT	density functional theory
EBSD	electron backscatter diffraction
FET	field-effect transistor
FFT	fast Fourier transform
FIB	focused ion beam
FM	Frank-van der Merwe
GGA	generalized gradient approximation
HAADF	high-angle annular dark field
HRTEM	high-resolution transmission electron microscopy

IPA	isopropyl alcohol
KPFM	Kelvin probe force microscopy
LEED	low-energy electron diffraction
LFM	lateral force microscopy
MFC	mass flow controller
ML	monolayer
MOSFET	metal-oxide-semiconductor field-effect transistor
PDMS	polydimethylsiloxane
PBE	Perdew-Berke-Ernzerhof
PL	photoluminescence
PMMA	poly(methyl methacrylate)
RMS	root-mean-squared
SAED	selected area electron diffraction
SEM	scanning electron microscopy
SK	Stranski-Krastanov
SS	sub-threshold swing
STEM	scanning transmission electron microscopy
TEM	transmission electron microscopy

TLK	terrace-ledge-kink
TMDC	transition metal dichalcogenide
TMO	transition metal oxide
VB	valence band
VW	Volmer-Weber
XPS	X-ray photoelectron spectroscopy
XRD	X-ray diffraction

Chapter 1

Introduction

1.1 Structure and Properties of 2D Materials

1.1.1 2D Materials History and Definition

Since the rediscovery of graphene by Novoselov and Geim in 2004,¹ two-dimensional (2D) materials, which are defined as being one or a few molecular layers thick, have seen continually increased interest in the research community.² Many studies have been performed to understand the properties and formation mechanisms of graphene and other 2D materials, given that these materials are unique from their bulk forms. 2D materials are layered, featuring strong, covalent, in-plane bonding and weaker, van der Waals forces between layers. This difference between in-plane and out-of-plane bonding gives rise to many novel physical and electronic properties.³⁻⁵

1.1.2 Physical Properties and Applications

The van der Waals forces between layers in 2D materials have long been used for their low-friction properties, such as for dry lubrication.^{6,7} Given that van der Waals forces are relatively weak and susceptible to cleavage by shear forces, they provide optimally low-friction in some mechanical environments. More recently, however, 2D materials have proven interesting for a number of applications in more active fields of research, including catalysis and optoelectronics.² For example, cobalt-functionalized MoS₂ acts as a common hydrodesulfurization catalyst in the oil industry for the generation of low-sulfur diesel fuel.⁸⁻¹⁰ Catalytic ability of these 2D nanostructures can be enhanced by optimizing their morphology and maximizing the number the active sites. Furthermore, 2D materials are particularly promising in the field of optoelectronics because of their large surface-to-volume ratio, good light sensitivity, and long photocarrier lifetime.¹¹⁻¹⁵

1.1.3 Transition Metal Dichalcogenides

While there are many material families within the umbrella of 2D materials, transition metal dichalcogenides (TMDCs) are possibly the most studied family in this class. TMDCs have the general formula MX_2 , where M is a transition metal (e.g. Mo, W, and Nb) and X is a chalcogen (or a group 16 element, e.g. S, Se, and Te). Many of these materials exhibit a lamellar structure with six-coordinate bonding of the chalcogen atoms around the transition metal.¹⁶ Of the layered TMDCs, one of the most frequently studied materials is MoS_2 . In this chapter, I will frequently use MoS_2 as an example to talk about its specific properties, but many of these properties are common among many other TMDCs. For more detail about the properties of other TMDCs, continue to read the other chapters of this dissertation.

MoS_2 features a MX_6 coordinate structure and can exhibit trigonal prismatic or octahedral coordination around the center molybdenum atoms (Figure 1.1). The 1H phase of MoS_2 , with Mo in trigonal prismatic coordination, is semiconducting, whereas the 1T phase, with Mo in octahedral coordination, is semi-metallic.^{17,18} 2H- MoS_2 is quite similar to the 1H phase, differing only by the fact that 2H requires having two or more layers in the crystal. 1H and 2H- MoS_2 are by far the most common phases of MoS_2 , as they are the most thermodynamically stable. Bulk 2H- MoS_2 belongs to the space group $\text{P6}_3/\text{mmc}$ (point group D^4_{6h}), featuring lattice constant (a) of 3.16 Å, interlayer lattice constant (c) of 12.30 Å, and layer spacing of about 6.5 Å.¹⁶⁻²⁰ The 1T phase, being only a single layer, has a significantly reduced c lattice constant of ~ 7 Å, whereas the 3R phase, being comprised of three MoS_2 layers per unit cell, has a larger c lattice constant of 18.37 Å.¹⁷ In each of

these cases the letter accompanying each phase denotes the crystal symmetry of the structure: T indicates a tetragonal crystal structure (D_{3d} group), H indicates a hexagonal crystal structure (D_{3h} group), and R indicates a rhombohedral crystal structure (C_{5v}^{3-} group).¹⁸

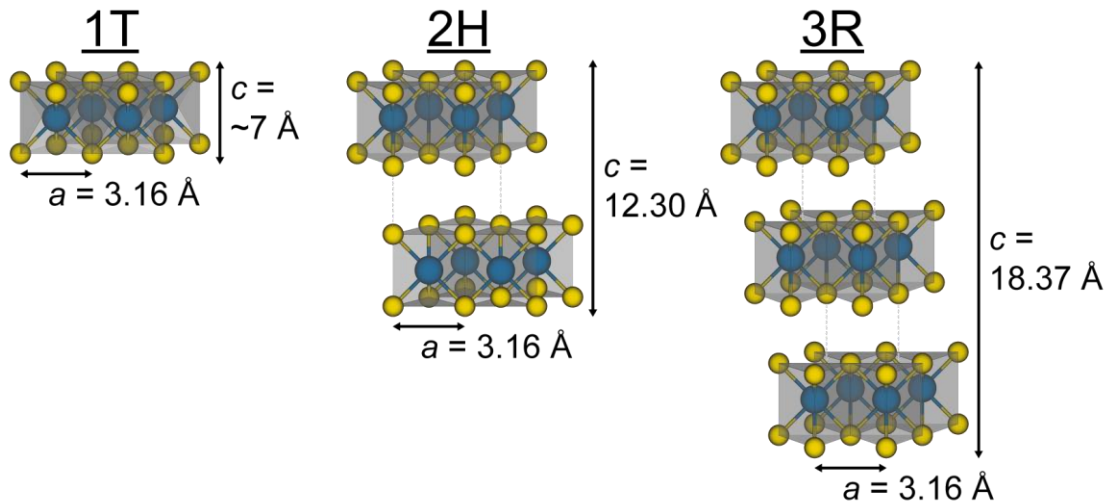


Figure 1.1. MoS₂ crystal structure. Schematic illustration of the three most common phases: 1T, 2H, and 3R. Each structure is labeled with corresponding a and c lattice constants.

1.1.4 TMDC Electronic Structure

The electronic properties of TMDCs are quite interesting, and it is these properties that have driven much of the prevalence of TMDCs in recent research. Bulk 2H-MoS₂ features an indirect band gap of 1.29 eV from the valence band (VB) maximum at the Γ point and the conduction band (CB) minimum at the K point (see Figure 1.2).^{2,5} When reduced to a single layer of 1H-MoS₂, however, this band gap shifts to 1.9 eV and becomes a direct excitation at the Γ point.^{19,21–23} Furthermore, this band gap is tunable based on the

number of layers in the material, with few-layer MoS₂ exhibiting an indirect band gap with magnitude between 1.29 and 1.9 eV, depending on the exact layer number.³ A change in crystal momentum is required for an indirect transition, in addition to the change in energy required for both direct and indirect transitions. Monolayer MoS₂, then, can be excited by a photon alone, given that the transition from valence to conduction band no longer requires an additional change in momentum. This difference allows for the excitation of an electron to be more energetically favorable, because it does not need this change in momentum. Possessing a direct band gap makes monolayer (ML) MoS₂ especially beneficial when applied to optoelectronic applications, because these applications require excitation from incident light. Furthermore, there exists a change in electron mobility of 2D MoS₂ devices between low- and room-temperature conditions. At reduced temperature (where exciton mobility is dominated by acoustic phonons, or in-phase movement of the atomic lattice), a mobility of $\sim 2450 \text{ cm}^2 \cdot \text{V}^{-1} \cdot \text{S}^{-1}$ has been achieved, whereas at room temperature (where exciton mobility is dominated by optical phonons, or out-of-phase movement of the atomic lattice), mobility is limited to $\sim 400 \text{ cm}^2 \cdot \text{V}^{-1} \cdot \text{S}^{-1}$.^{5,24}

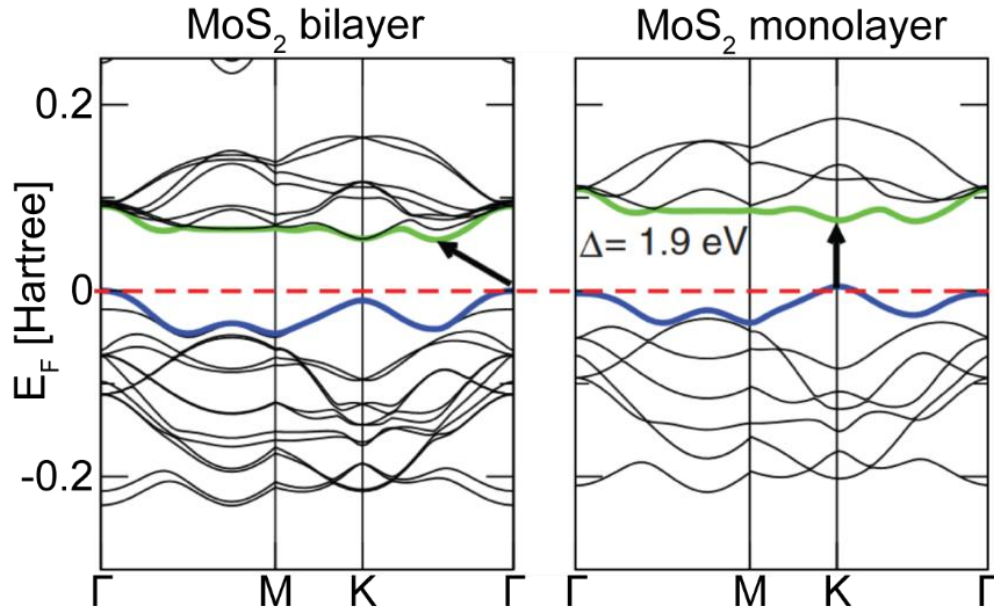


Figure 1.2. Band structures of bilayer and monolayer MoS₂. These band structures were calculated by density functional theory (DFT) using the general gradient approximation (GGA) in the scheme of Perdew-Burke-Ernzerhof (PBE). The blue trace represents the valence band maximum, the green trace represents the conduction band minimum, and the arrow represents the band gap in each case. Reprinted figure with permission from Kuc, A.; Zibouche, N.; Heine, T. *Phys. Rev. B* **2011**, 83 (24), 245213.³ Copyright 2011 by the American Physical Society.

MoS₂ and other TMDCs are also promising for the applications of spin- and valleytronics.²⁵ These fields seek to exploit the unique properties of TMDCs and other materials to control their spin and valley degrees of freedom, as a way of improving the efficiency of data storage and transfer. 2D TMDCs typically possess a lack of inversion symmetry, by nature of their atomically-thin structure, and large spin-orbit coupling. These properties give rise to strong spin-orbit splitting and thereby enable the possibility of valley polarization.²⁶ These properties of TMDCs could allow for significant future advances in the field of valleytronic devices.

Many of the properties of MoS₂ discussed above, including MX₆ coordinate structure, P6₃/mmc space group, and semiconducting band structure with indirect-to-direct transition based on layer number, are common to other well-studied TMDCs. Among these analogs are WS₂, WSe₂, and MoTe₂, which will be discussed in detail later.

1.2 Isolating 2D Materials

1.2.1 Exfoliation

2D TMDCs need to be isolated before they can be used in the various applications for which they prove interesting. Possibly the simplest method for the harvesting of 2D materials is micromechanical exfoliation. This method involves the placement of a bulk crystal of the 2D material of interest between two pieces of adhesive film and repeatedly separating the adhesives (Figure 1.3). The adhesive can be something as simple as Scotch™ tape, hence the casual reference to this technique as the Scotch™ tape method, or a deposited film of poly(methyl methacrylate) (PMMA) or polydimethylsiloxane (PDMS). This process of repeated adhesion and de-adhesion cleaves the layers of the crystal, which is easily achieved due to the weak van der Waals forces between layers.²⁷ Upon adhering one of these pieces of adhesive to a substrate of interest (or dissolving the adhesive in a solvent and drop-casting the resulting solution on a substrate), many mono- and few-layer crystallites can be observed on the substrate. Despite the relative ease and cost-effectiveness of this technique, it has many drawbacks. Micromechanical exfoliation gives little control over the thickness of the resulting flakes, their length and width, the number of flakes isolated, or any other morphological traits (such as flake density or separation between flakes on the substrate).^{10,28} Additionally, the repeated use of sticky

adhesives often leaves polymer residue on the flakes and surrounding substrate, which can interfere with subsequent measurement or deposition steps.²⁹ Because of these drawbacks, micromechanical exfoliation often results in small batches, with resulting flakes varying in size and being difficult to use for device integration.

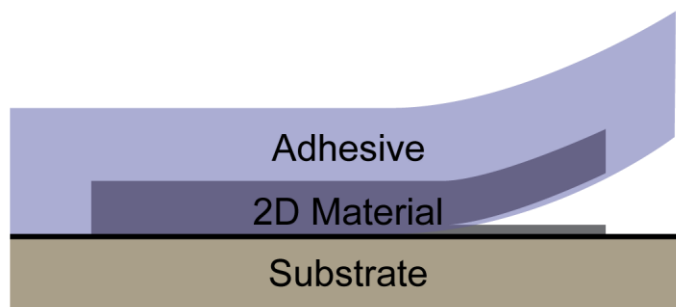


Figure 1.3. Schematic illustration of the exfoliation process. In this illustration, a thin layer of a 2D material is being deposited on a substrate using an adhesive film.

A wide number of modified exfoliation procedures have been published in the literature, including intercalation-assisted exfoliation, in which ions (typically lithium) intercalate between layers of the crystal and allow for easier exfoliation,³⁰ as well as solvent-assisted exfoliation, in which a solvent (such as isopropyl alcohol or *N*-methylpyrrolidone) helps exfoliate the layers.³¹ Modified exfoliation methods such as these have produced 2D TMDCs for many works dating back to the 1960's.^{2,20} Larger batch sizes can be accomplished by intercalation- and solvent-assisted exfoliation methods, but these methods share many of the morphological drawbacks of micromechanical exfoliation. Furthermore, intercalation- and solvent-assisted exfoliation can promote unintended

chemical changes in the material, including crystallographic phase changes in the crystal structure,^{32,33} sometimes resulting in metallic (1T) character in isolated flakes of MoS₂.^{16,31}

1.2.2 Chemical Vapor Deposition

1.2.2.1 CVD Mechanism

Chemical vapor deposition (CVD) is a synthetic technique that has been used to grow nanomaterials and thin films with a variety of morphologies.^{34,35} CVD is often described mechanistically by the adsorption of a gas-phase reactant to the substrate surface, a chemical reaction on the surface resulting in the deposition of a solid material (the desired growth material), followed by the desorption of chemical byproducts (Figure 1.4).³⁴ To this end, the relative binding energies between chemical components and the surface energy of the substrate are all parameters that can greatly impact the growth conditions.

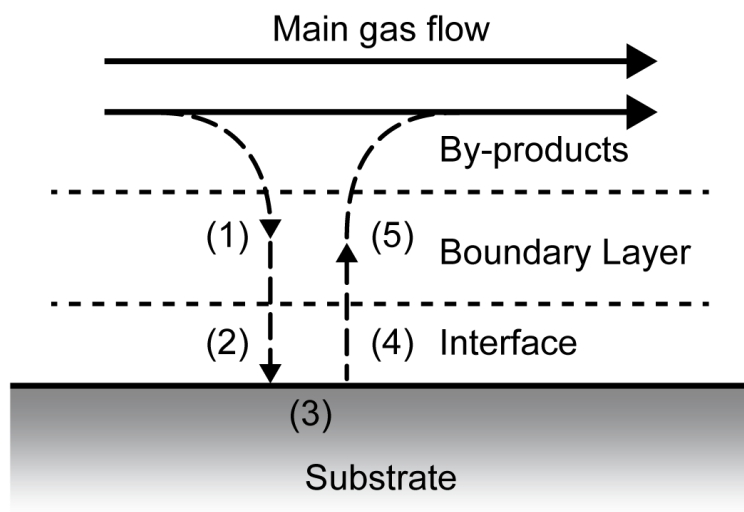


Figure 1.4. General mechanism for CVD growth. (1) Diffusion of reactants through the boundary layer, (2) adsorption of reactants onto the surface of the substrate, (3) diffusion along the surface and subsequent chemical reaction, (4) desorption of adsorbed species, including by-products and unreacted precursors, and (5) diffusion of by-products and unreacted precursors out of the boundary layer, to be exhausted.

In the case of MoS₂ CVD growth, for example, the gas flow is composed predominantly of an inert gas (such as Ar or N₂) containing partial pressures of H₂ gas and S vapor. This reducing atmosphere leads to the partial reduction of the transition metal oxide (TMO) precursor, MoO₃, to the more volatile MoO_{3-x} species.³⁶ Then, both vapor phase precursors, MoO_{3-x} and S, diffuse through the boundary layer and adsorb onto the surface of the substrate, subsequently reacting to form MoS₂ units. Oxygen is then left as a by-product to desorb from the substrate and diffuse out of the boundary layer into the carrier gas flow region.

CVD growth of 2D materials generally involves the radiative heating of a quartz tube in a tube furnace with gas flow and volatile precursors (Figure 1.5).³⁵ The flow of each

gas is controlled by a regulator and mass flow controller (MFC). Most CVD methods provide uniform coverage across the substrate and allow for rational control of precursor deposition and scalability, provided sufficient reaction kinetics. The rate-limiting step of CVD reactions is usually determined by surface reaction kinetics, typical for reactions with low temperature and pressure conditions, or by mass transport, typical for reactions with high temperature and pressure conditions.³⁴ Tuning the temperature, pressure, and vapor-phase concentration of precursors can all affect the rate of the reaction.

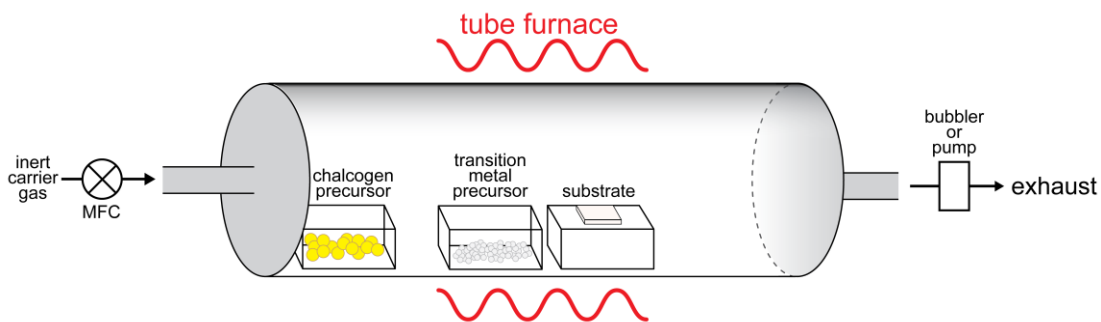


Figure 1.5. General CVD setup schematic. The quartz tube is heated by a tube furnace, indicated by the red waves. An inert carrier gas flows through the tube, as controlled by a mass flow controller. As the chalcogen and transition metal precursors volatilize in this example of TMDC growth, the precursors are carried by the inert carrier gas flow and delivered to the substrate for the reaction. By-products and unreacted precursors are exhausted by a bubbler or roughing vacuum pump.

Practically, there are many ways to control most of the variables present in a CVD reactor. The chamber pressure can be coarsely controlled by the method of exhausting the gas, specifically whether the setup uses a low-pressure method, such as a roughing vacuum

pump (typically operating with a chamber pressure between 1 mTorr and 1 Torr) or an ambient pressure mechanism, such as a mineral oil bubbler, which allows excess carrier gas and gas byproducts to leave the chamber without air backstreaming into the reaction vessel. The chamber pressure can further be controlled by the gases used and their respective flow rates. High flow rates will lead to higher chamber pressures when a roughing pump is used, but high flow rates should not change the chamber pressure with an ambient pressure method, such as when using a mineral oil bubbler.

The temperature of the reaction chamber can be controlled by the furnace's programmed temperature ramp (in which subtleties of ramping rate, dwell times, and cooling rate all affect the reaction kinetics), and the local temperature of the precursors and substrates can be adjusted by their individual placement inside the tube. The tube furnace creates a temperature gradient with the peak temperature located at the center of the furnace, and the upstream and downstream ends of the quartz tube being significantly cooler, especially the parts of the tube that are exposed to air outside of the furnace. If a precursor has a relatively low vapor pressure, the boat containing this precursor should be placed close to the center of the furnace to facilitate a greater vapor-phase concentration of this precursor during the reaction. If a precursor has a relatively high vapor pressure, the boat containing the precursor should be placed farther upstream such that the temperature it feels at the peak of the furnace program is less than the peak temperature in the center of the furnace. This time in which the furnace is at its peak temperature is often referred to as the "reaction time," and it is during this time that the precursors are likely at their peak vapor pressures and the adsorbed precursors are undergoing a reaction on the surface. For some precursors, such as sulfur and most other chalcogens, there will be a solid-to-liquid

phase transition that will dramatically increase the vapor pressure of the precursor. It is important to consider the timing of this phase transition, as melting too early can result in contamination and conversion of other precursors prior to the intended reaction time, whereas melting too late can result in no reaction at all. Other details related to precursor timing will be discussed in Chapter 2, in the context of general CVD growth of TMDCs, and in Chapter 4, in the context of MoO₂/MoS₂ core/shell plates.

1.2.2.2 Fick's Laws of Diffusion

The flux of a vapor-phase material in a CVD system can be expressed by Fick's laws of diffusion, which describe the net diffusion of atoms in a concentration gradient. They are expressed by:

$$J = -D \frac{d\phi}{dx} \quad (1.1)$$

$$\frac{d\phi}{dt} = D \frac{d^2\phi}{dx^2} \quad (1.2)$$

where J is the flux, D is the diffusion constant, ϕ is the concentration of the material, x is position, and t is time.^{37,38} These laws manifest themselves in CVD reaction systems in many ways. The flux, J , of a given precursor is directly proportional to the concentration gradient of precursor vapor (Equation 1.1). Thus, increasing the mass or concentration of a precursor in a CVD reaction will directly increase the flux of the material in the system by increasing the magnitude of the concentration gradient. Similarly, increasing the temperature or decreasing the pressure of the system will increase precursor mass transfer due to the increased concentration of precursor in the vapor phase.³⁴ As was discussed in

the previous section, changing the peak temperature and overall reaction pressure affects all species in the chamber, whereas local precursor temperature can be changed by moving the position of the precursor to different points along the temperature gradient. By changing the location of a given precursor within the temperature gradient, the vapor phase concentration of the precursor, and thus the magnitude of the concentration gradient, will change. These effects are all manifested in Fick's laws of diffusion. Quantitative effects of these changes on the CVD system can be calculated using Fick's laws of diffusion and other derived expressions.

1.2.2.3 Terrace-Ledge-Kink Model

The terrace-ledge-kink (TLK) model describes the thermodynamics of crystal growth and reformation, and it can be applied to CVD growth of 2D materials.³⁹⁻⁴¹ This model suggests that the atoms removed or dislocated during a reconstruction event will be those with binding energy of the smallest magnitude, and similarly, those with the greatest binding energy will remain after the reaction is finished. A molecular unit that diffuses across the surface of a growing crystal will have a variety of locations to which it can bind, all of which have different energetics based on coordination to other nearby molecular units. Molecular units, or adatoms, that initially bind to the terrace of a crystal will likely diffuse along the surface, due to relatively low binding energy, until it either finds a site with greater binding energy, such as a ledge or kink, or it desorbs and reenters the gas stream (see Figure 1.6).

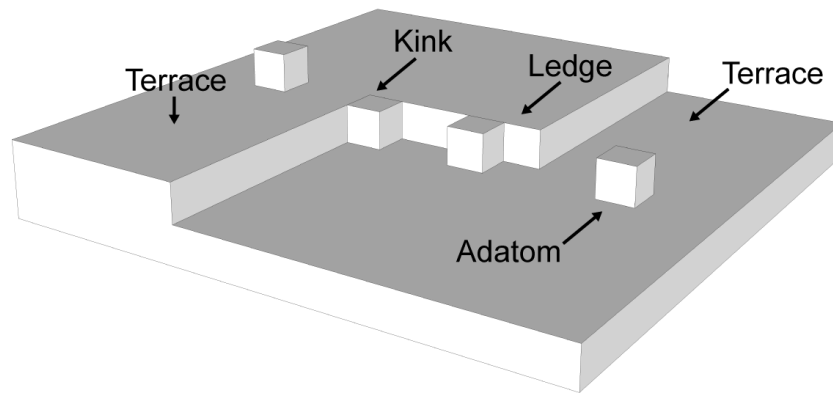


Figure 1.6. Schematic illustration of adatom sites in the TLK model. The least thermodynamically stable locations are terrace sites, as they are only stabilized by binding on one edge. Increasingly stable locations are ledge and kink sites, which are stabilized by binding on two and three edges, respectively. Bulk sites are the most energetically stable, as they feature complete coordination within the crystal lattice.

The TLK model nominally describes the defects present in a single crystal growth or reconstruction event, but it can also be used to educate the CVD growth of 2D materials and TMDCs on a substrate. In the general TLK model, all binding directions are equally stabilizing, and thus an adatom will be more stable with a greater degree of coordination. This is generally still true for 2D materials, but the covalent bonding between two atoms in the same layer is stronger than the van der Waals forces between a layer and nucleating units above or the substrate below. This anisotropy in the binding forces makes adatoms on a terrace site relatively less stable than those of single crystal growth, and similarly, adatoms in a kink site relatively more stable. Because of this, it can be difficult to nucleate 2D material growth on a clean surface, but once nucleated, growth can occur quite rapidly. Furthermore, ultraclean growth of 2D materials can select toward monolayer growth, by nature of the weaker van der Waals surface forces.

1.2.2.4 Film Growth Modes

Once growth begins, there are three main growth modes that can dictate the resulting film structure: Volmer-Weber (VW), Frank-van der Merwe (FM), or Stranski-Krastanov (SK). Schematic depictions of these growth modes can be seen in Figure 1.7. Each of these three modes differs by the surface tensions between the growth material, substrate, and growth medium (in this case, gas stream).⁴⁰⁻⁴³ Each of these growth modes can be understood by the following relationship describing the equilibrium condition,

$$\gamma_S = \gamma_{S-F} + \gamma_F \cos \varphi \quad (1.3)$$

where γ_S is the surface tension of the interface between the substrate surface and the growth medium, γ_F is the surface tension of the interface between the film and the growth medium, γ_{S-F} is the surface tension of the interface between the film and substrate, and φ is the island wetting angle.

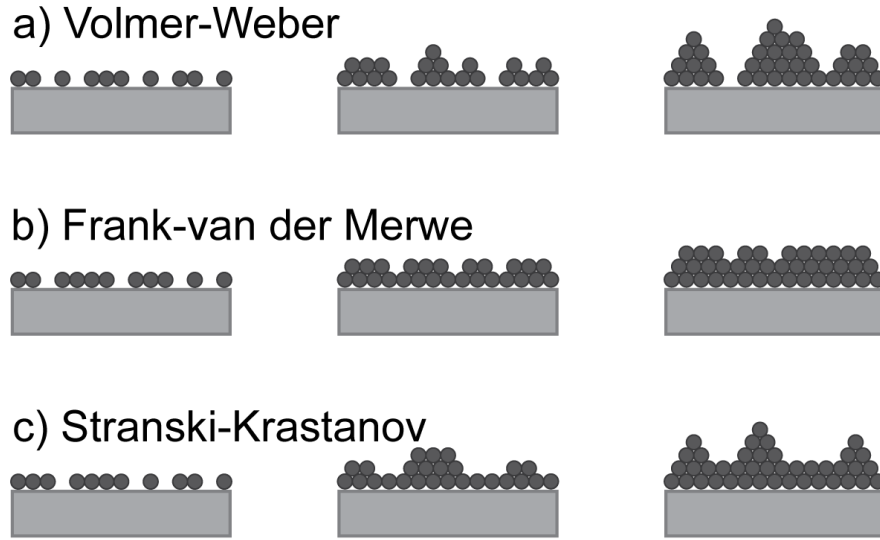


Figure 1.7. Schematic representations of the three main growth modes: (a) Volmer-Weber growth, resulting in island growth, (b) Frank-van der Merwe growth, resulting in layer-by-layer growth, and (c) Stranski-Krastanov growth, resulting in initial layer-by-layer growth and subsequent island growth.

In VW growth, the cohesive force between two incoming adatoms is stronger than the adhesive force of the adatom to the substrate, which results in the aggregation of islands or particles on the surface of the substrate, with little to no film growth.⁴²⁻⁴⁴ Because of this, $\varphi > 0$, and the corresponding condition can be written as

$$\gamma_S < \gamma_{S-F} + \gamma_F . \quad (1.4)$$

In FM growth, the exact opposite is true: the adhesive force between the adatom and the substrate in this case is greater than the cohesive force between two adatoms, resulting in uniform film growth, where each layer wets the surface. Because each subsequent layer maintains complete contact with the substrate (or the surface of the growth layer directly

preceding the incoming layer), $\varphi = 0$ in this case, and the surface tensions can be described by

$$\gamma_S > \gamma_{S-F} + \gamma_F . \quad (1.5)$$

SK growth is a balance of these previous two cases, in which growth is originally dominated by the FM growth mode, forming complete wetting layers. After the initial layer is complete, the surface tension values of γ_S and γ_{S-F} change and the cohesive forces between adatoms become greater than that of layer wetting on the surface. Subsequent growth is then dominated by a VW-like mechanism, with islands or particles forming on top of the deposited wetting layers.⁴⁵

In the context of the general mechanism of CVD growth, the TLK growth model, or the different growth modes, the choice of growth substrate can have many effects on the resulting material growth. The following chapter will describe many considerations when choosing a growth substrate, as well as experiments I have performed to control the CVD growth of TMDCs by controlling the substrate surface.

Chapter 2

Substrate Effects

2.1 Preface

When considering the CVD growth of 2D TMDCs and related heterostructures, the choice of substrate is very important. In this chapter, fundamental parameters related to epitaxial growth are considered and subsequently applied to synthetically relevant substrates. The surface preparation of 4H-SiC, *c*-cut sapphire, SiO₂/Si, GaN/Si, and GaN substrates are pursued via passivation, annealing, and electrochemical polishing methods. These substrates are then used for the CVD growth of MoS₂, NbS₂, and WSe₂, and the resulting crystals are analyzed. The growth of NbS₂ is investigated via two different precursors, Nb₂O₅ and NbCl₅, and the resulting crystals generated from these methods show different morphologies. As-grown WSe₂ is shown to be symmetrical and monolayer in nature, but it also degrades in air, thus a selenization procedure is performed. These CVD-grown 2D TMDCs show promise for large-area growth and the growth of relevant heterostructures.

2.2 Introduction

2.2.1 Epitaxy

There are many considerations when choosing a substrate for growth. As was discussed in the context of the TLK model and the different film growth modes in Chapter 1, the surface energy of the substrate is a crucial parameter that determines if an incoming molecular unit is likely to bind upon adsorption and the subsequent nature of film growth. Additionally, the crystallinity of the substrate surface is an important property. Epitaxy, the deposition of one crystalline material on another with crystallographic registry between the materials, is very sensitive to the crystal structure (e.g. space group) and lattice parameters

of both materials.^{41,46,47} Heteroepitaxy, in which the oriented growth of one crystalline material is grown on a different crystalline material, can allow for the fabrication of high-quality heterostructures without interfacial contamination.

Many factors must be considered if one is to achieve successful heteroepitaxial growth. Foremost is the crystal structure of the two materials. Two materials with similar crystal structures are more likely to facilitate heteroepitaxial growth than those with different crystal structures, because similar crystal symmetries allow for better geometric alignment at the interface. Another main consideration, even among materials of the same crystal structure, is the lattice mismatch between the two materials. The lattice mismatch is defined as the difference between the lattice parameters of the deposited material relative to the substrate,⁴⁷ demonstrated here:

$$\varepsilon = \frac{a_A - a_B}{a_B} \quad (2.1)$$

where a_A is the lattice parameter of the deposited material and a_B is the lattice parameter of the substrate or previously grown material. This concept is schematically illustrated in Figure 2.1. A small lattice mismatch generally leads to a greater likelihood of successful heteroepitaxy, due to reduced strain at the interface. Large lattice mismatch in heteroepitaxially grown materials typically results in increased interfacial strain, more dangling bonds and defects, and reduced adhesion between layers.^{34,40,47} There is no definitive lattice mismatch limit, below which heteroepitaxial growth is permitted and above which heteroepitaxial growth is forbidden, as some material systems allow for heteroepitaxial growth with larger lattice mismatch than other materials. However, a general rule of thumb is that material systems with smaller lattice mismatch are more likely

to allow for uniform heteroepitaxial growth. In systems with large lattice mismatch that can still achieve heteroepitaxial growth, factors such as small energetic penalties or large bond strengths can allow for the compensation of large strain values.^{48,49} Additionally, some heteroepitaxial systems with exceedingly large lattice mismatch values can form supercells, in which a certain number of unit cells of the deposited layer overlaps perfectly with a different number of unit cells of the substrate.⁵⁰⁻⁵²

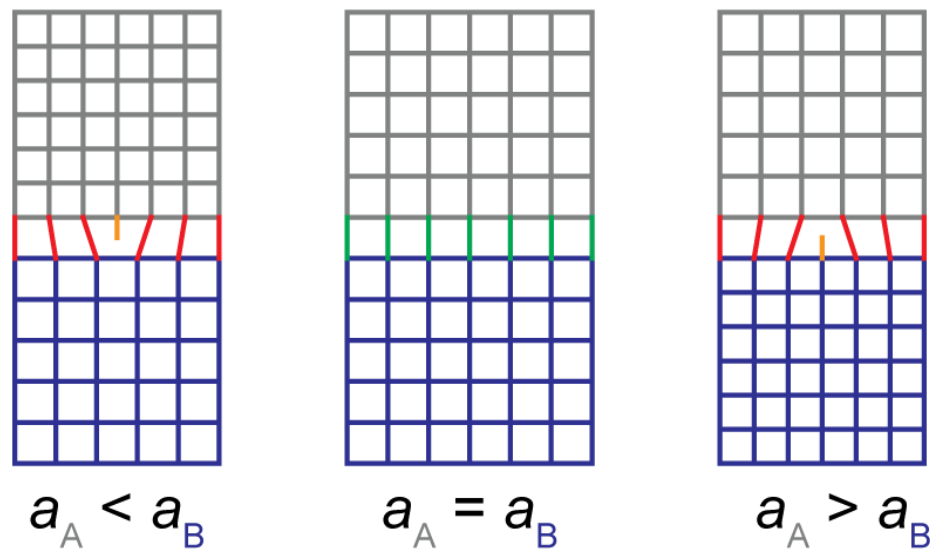


Figure 2.1. Schematic illustration of epitaxy. In this example, epitaxy is formed between two materials (grey and blue lattices) with three hypothetical lattice parameter relations. When the lattice constants are the same ($a_A = a_B$), unstrained covalent bonding (green lines) can occur at the interface with minimal strain and no dangling bonds. When the lattice constants are dissimilar ($a_A > a_B$ or $a_A < a_B$), bonding at the interface is likely to be strained (red lines) and dangling bonds (orange lines) are likely to occur.

Other factors can affect the success of epitaxial growth. The surface roughness of the substrate plays a key role, as large physical bumps and kinks can impede the growth of

another material. Contaminants and adatoms on the substrate surface can impose other physical or chemical barriers to ideal growth on the surface. The stability of the exposed crystal surface of the substrate is important, because an unstable surface may react under the growth conditions of the deposited material and reconstruct to a more stable crystal surface.^{41,53} This more stable crystal surface may have different lattice parameters or a different crystal structure, which would thereby change the crystallographic alignment of the materials. Additionally, specific surface reconstructions can be selectively achieved by inducing the desired crystal surface prior to growth of the second material, which can be used to aid the growth.

Epitaxy can also exist between 2D materials and crystalline 3D substrates. The van der Waals forces above and below the 2D material induce a van der Waals gap with no covalent bonding between the material and substrate, which changes the epitaxial relation of the two materials. By nature of these van der Waals forces, this mode of epitaxy is termed van der Waals epitaxy.⁵⁴⁻⁵⁶ The crystallographic relationship between the 2D material and 3D substrate is still important, but the van der Waals gap at the interface in these systems allows for a significant relaxation of the lattice mismatch requirement for standard epitaxy between 3D crystals.⁵⁷ Thus, it can be significantly easier to grow uniform 2D materials on pristine, crystalline substrates with larger lattice mismatch than would be possible between two 3D crystals with the same lattice mismatch.

2.3 Experimental

2.3.1 SiC Passivation

Early experiments in my thesis work sought to take advantage of the van der Waals epitaxy of 2D materials on crystalline substrates to facilitate large-area growth. The main system of study in these experiments is the CVD growth of MoS₂ on hydrogen-passivated 4H-SiC(0001).^{58,59} SiC is a wide band gap semiconductor that is regularly used in the electronics industry. The (0001) surface of 4H-SiC has a hexagonal lattice (space group P6₃mc) with relatively small lattice mismatch between it and MoS₂ (2.83%), thus would be an ideal substrate for growth.^{60,61} The surfaces of commercially available SiC substrates have a native oxide surface layer, but it has been shown that the surface oxide layer can be removed and the SiC surface can be passivated with hydrogen bonds by high-temperature (greater than 1000 °C) annealing in a pure H₂ atmosphere. I performed experiments to achieve hydrogen-passivated 4H-SiC(0001) surfaces, which involved the use of a CVD tube furnace setup with pure H₂ gas being supplied by a mass flow controller. Quartz tubes were used at temperatures below ~1200 °C and alumina tubes were used for reactions between 1200 °C and 1500 °C, because quartz softens above ~1250 °C. A pair of 4H-SiC substrates were placed in the center of the tube, with one on top of the other and the chemically polished surface of each facing one another to limit the concentration of H₂ reaching the SiC surface. Prior to the annealing, each substrate was rinsed and sonicated in acetone, isopropyl alcohol (IPA), and nanopore milli-Q water for 10 min each. Cylindrical graphite blocks were used inside the tube near both tube adapters to prevent any tube softening or silicone o-ring degradation in the tube adapters. The resulting offgas from this passivation was simply evacuated through a ¼” corrosion-resistant stainless-steel tube and

exhausted by an open flame. This offgas is composed primarily of H₂ gas, so lighting it aflame in ambient conditions results in clean byproducts largely consisting of gaseous water.

Ultimately, the goal of these passivation experiments was to generate a system in which the highly ordered surfaces of electronically relevant crystalline substrates could be used to facilitate large-area 2D material growth. To this end, another set of experiments was performed to achieve well-ordered, crystalline sapphire surfaces.

2.3.2 Sapphire Annealing

Sapphire is an inexpensive and commercially available substrate that is frequently used for material growth. Sapphire features a significantly larger lattice constant than MoS₂ and other TMDCs and has a different space group, but MoS₂ can form a coincident hexagonal superlattice of (3 × 3) MoS₂ on (2 × 2) Al₂O₃(0001). This coincident superlattice has a lattice mismatch of only 0.21%, which is favorable for van der Waals epitaxy. Thus, I investigated the annealing of *c*-cut sapphire substrates for the growth of large-area, ML MoS₂. Prior to the annealing, each *c*-cut sapphire substrate was rinsed and sonicated in acetone, isopropyl alcohol (IPA), and nanopore milli-Q water for 10 min each. The substrates were then annealed to 1400 °C in an alumina tube for up to 5 hours. During this annealing, the alumina tube was open to air to facilitate surface oxidation and step flow.

2.3.3 GaN Polishing

GaN, a direct bandgap semiconductor commonly used for device fabrication, is another crystalline material that has previously been used as a growth substrate for 2D materials.^{60,62} GaN has very small lattice mismatch with MoS₂ (0.64%), thereby making it an inherently favorable substrate for van der Waals epitaxy. It has also been demonstrated that one can induce a smooth GaN surface reconstruction by electrochemical polishing on a Pt plate in deionized water.⁶³ Thus, I performed a set of experiments attempting to polish commercially available, epitaxially grown GaN films on Si, such that they could be used as a cost-effective way of growing large-area, high-quality CVD MoS₂ on GaN.

I constructed a home-built polishing apparatus using aluminum stock and a counterweight for structural support, a micrometer for applying pressure to the substrate, and a level mounting platform to hold the GaN sample flat on the surface of the Pt foil. In this setup, the Pt foil was fixed to a petri dish on a standard polishing wheel and the GaN sample was held face-down onto the Pt foil and immersed in nanopore milli-Q water while the polishing wheel rotates. Per the previous report, the GaN polishing needed to be performed at a pressure of 40 kPa to achieve the desired surface reconstruction. To calibrate the pressure that would be applied by the micrometer, I aligned the polishing apparatus above a digital balance and tared the mass with the mounting platform flush to the balance platform. A 1 cm² piece of SiO₂/Si was adhered to the surface of the mounting platform with Crystalbond epoxy, to ensure comparable surface area to the intended GaN samples.

Once the pressure applied by the polishing apparatus was calibrated, I performed some initial polishing tests using SiO₂/Si samples and Cu foil, to measure the effect of physical abrasion from this polishing setup on a non-interacting pair of surfaces, as well as

to ensure the apparatus could remain stable amid the mechanical rigors of the polishing. To perform these initial tests, the polishing apparatus with mounted SiO₂/Si sample was placed above a polishing wheel fitted with a petri dish to hold nanopore milli-Q water and the Cu foil, all of which were mounted using double-sided tape. After successive tests with fractional pressures being applied to the sample, polishing of the SiO₂/Si substrate on Cu foil was performed at full pressure for one hour.

With the polishing apparatus stable under the desired conditions, I performed electrochemical polishing using Pt foil and epitaxially grown GaN/Si (MTI Corp.). This GaN/Si wafer was rinsed in acetone, IPA, and milli-Q water prior to being adhered to the bottom of the mounting platform of the polishing apparatus using Crystalbond epoxy. Pt foil was adhered to the bottom of a petri dish using double-sided tape, and the petri dish was filled with nanopore milli-Q water. This electrochemical polishing procedure was also performed on single-crystal GaN wafers, to serve as a comparison to the GaN/Si samples and to offer another possibility for an electrochemically reconstructed surface for the subsequent CVD growth of 2D TMDCs.

2.3.4 CVD Growth of MoS₂ on Various Substrates

With a variety of substrates to grow on, I began the process of optimizing the CVD growth of ML MoS₂. MoS₂ monolayers were synthesized in a horizontal hot-wall three-zone tube furnace (ThermoFisher Blue M, with only the center zone being heated), equipped with a vacuum pump (Edwards RV-8) and mass flow controllers (MTI Corp.). An alumina boat (50 × 20 × 20 mm, MTI Corp.) containing 100 mg MoO₃ powder (99.999%, Acros Organics) was placed at the center of the furnace in a 3-inch diameter

quartz tube. A substrate was placed face-up on an upside-down alumina boat placed directly downstream from the boat containing MoO₃ powder. Initial ML MoS₂ growths were performed on 90 nm SiO₂/Si and *c*-cut sapphire substrates, but subsequent growths were performed on annealed sapphire and 4H-SiC. 800 mg S powder (99.999%, Alfa Aesar) was located upstream, maintained at a reduced temperature during the reaction (approximately 280 °C at the peak of the reaction). After loading, the tube was evacuated to less than 100 mTorr, and Ar and H₂ gases were supplied at rates of 30 and 5 sccm (standard cubic centimeters per minute), respectively. The reaction was carried out under atmospheric pressure. The center of the furnace (and thus the substrate and MoO₃ powder precursor) was heated to 730 °C at a rate of approximately 22 °C/min and kept at 730 °C for 5 min. After the reaction, the furnace was rapidly cooled by opening the lid of the furnace. At this point, the Ar gas flow was increased to 200 sccm, to purge any toxic vapors.

2.3.5 NbS₂ CVD Growth

NbS₂ is another 2D TMDC with P6₃mc crystal structure, and, in this way, it is similar to other TMDCs, including MoS₂ and WS₂. However, NbS₂ is metallic and even shows superconductivity at low temperatures.⁶⁴⁻⁶⁷ Metallic TMDCs are less well-studied than their semiconducting counterparts, thus there is much room for future work in the field of metallic 2D TMDCs. In the remainder of this chapter, I will discuss the work I have performed to grow 2D NbS₂ via CVD.

Initial CVD growths of NbS₂ involved a similar reaction scheme to that of the MoS₂ growths I discussed previously and other TMDC growths adapted from the literature. This scheme involves the use of transition metal oxide and chalcogen precursors evolved into a

gas stream comprised of Ar and H₂ carrier gases. However, the vapor pressure of Nb₂O₅, the most stable form of niobium oxide, is significantly lower than that of other transition metal oxides. Because of this reduced vapor pressure, initial NbS₂ growths required temperatures as high as 1500 °C, and thus required the use of a high-temperature tube furnace and an alumina tube.

To perform these initial oxide-based NbS₂ growths, 600 mg of Nb₂O₅ powder was placed at the center of a 2” alumina tube in a single-zone, high-temperature tube furnace. 1.0 g S precursor was placed upstream from the hot zone, at a position such that it melted during the peak of the reaction but was not completely exhausted after the reaction (some sulfur remained in the boat when unloading from the tube after the reaction). *c*-cut sapphire substrates were placed polished face-up on an upside-down alumina boat downstream from the hot zone, so as to receive optimal precursor flux and nucleation. After loading, the tube was purged with inert Ar gas, followed by the introduction of H₂ gas. The furnace was then ramped to 1470 °C at a rate of ~10 °C/min, held at 1470 °C for 5 hours, cooled to 800 °C at a rate of ~5 °C/min, and then cooled to room temperature naturally. This slow cooling procedure was used to prevent fracturing of the alumina tube at high temperatures.

I also pursued the CVD growth of NbS₂ through the use of a chloride-based procedure using NbCl₅ precursor. NbCl₅ is significantly more volatile than Nb₂O₅, which makes the chloride-based synthesis more amenable to growth at lower temperatures. However, the volatility of NbCl₅ warrants extra consideration when handling. NbCl₅ left open to the air reacts with water to form Nb₂O₅ within an hour, thus NbCl₅ stock must be kept in an inert environment, such as a glovebox. ~100 mg quantities of NbCl₅ were

allocated into Teflon-capped vials inside a glovebox and these vials were removed from the glovebox prior to growth.

To perform the chloride-based NbS₂ growths, substrates were placed at the center of a 2” quartz tube in a split-hinge furnace. 1.0 g S precursor was placed in a precursor boat upstream from the furnace’s center zone, again, such that the sulfur was molten during the peak of the reaction but was not completely exhausted after the reaction. NbCl₅ was placed in an alumina boat located farther upstream, such that the temperature experienced by the NbCl₅ during the reaction was even lower than that of the sulfur. Due to the volatility of NbCl₅, it was always the last component to be loaded into the tube, and Ar gas was flowed at a rate of 200 sccm prior to sealing the tube, in an effort to create a more inert environment in the tube upon NbCl₅ loading. Once the seal on the vial was broken, the NbCl₅ was loaded into an alumina boat, placed in the tube at the appropriate position, and the tube was sealed to begin pumping and purging within 100 seconds. After pumping and purging, the carrier gases were equilibrated to 60 sccm Ar and 1 sccm H₂, and the reaction was carried out at low pressure (~400 mtorr). The furnace was then heated to 1000 °C at an average rate of ~12 °C/min. To gauge the length of the reaction, the physical state of the S precursor was monitored. Once the surface of the S precursor remained completely molten for 7 minutes, the furnace was shut off and rapidly cooled by opening the lid of the furnace.

2.3.6 WSe₂ CVD Growth and Selenization

WSe₂ is unique to many of the other semiconducting TMDCs in that it is intrinsically p-type, with a bulk indirect band gap of ~1.2 eV and a monolayer direct bandgap of ~1.65 eV.⁶⁸ WSe₂ also shows unique spin orbit splitting and is a single photon

emitter, making WSe₂ quite promising for future work in the fields of spintronics and quantum optoelectronics.^{25,69} Given the potential for these exciting physical properties, I began to optimize the CVD growth of ML WSe₂.

The growth procedure for WSe₂ is similar to that of MoS₂ described above, involving the use of a horizontal hot-wall three-zone tube furnace equipped with a vacuum pump and mass flow controllers. An alumina boat containing 800 mg WO₃ powder (99.999%, Alfa Aesar) was placed at the center of the furnace in a 2-inch diameter quartz tube. A substrate was placed face-up on an upside-down alumina boat placed immediately downstream from the alumina boat containing WO₃ powder. 200 mg Se slug (99.998%, Alfa Aesar) was placed in an alumina boat located upstream, maintained at a reduced temperature during the reaction. After loading, the tube was evacuated to less than 100 mTorr, and the tube was repeatedly purged and pumped down to rid the chamber of ambient contaminants. Ar and H₂ gases were then supplied at rates of 40 and 1 sccm, respectively and the subsequent reaction was carried out under atmospheric pressure. The furnace was heated to 1050 °C at an average rate of approximately 10 °C/min and kept at 1050 °C for 5 min. During these last five minutes of the reaction, the H₂ flow rate was increased to 6 sccm to prevent additional nucleation on the substrate surface and at the edges of the ML WSe₂ crystals. After the reaction, the furnace was rapidly cooled by opening the lid of the furnace. At this point, the Ar gas flow was increased to purge any toxic vapors and prevent mineral oil from flowing back into the chamber from the bubbler during the rapid cooling.

I investigated the selenization of as-grown WSe₂ crystals to prolong their stability in air. Selenization reactions were set up in a fresh 2" quartz tube with no WO₃ precursor

present. As-grown WSe₂ was placed face-up on an alumina boat near the center of the furnace and selenium shot was placed in an alumina boat upstream from the substrates. After loading, the chamber was pumped down and purged repeatedly, and the reaction was performed at ambient pressure. The furnace was heated to 550 °C at an average rate of approximately 18 °C/min and kept at 550 °C for 2 hrs. The furnace was then cooled slowly by allowing the furnace lid to remain closed for 30 min until the furnace reached a temperature of 375 °C, at which point the lid was opened to allow the furnace to cool to room temperature.

2.4 Results and Discussion

2.4.1 SiC Passivation

Initial hydrogen passivation of 4H-SiC surfaces at 1000 °C in a quartz tube results in rough but regular, near-parallel terraces indicative of successful passivation (Figure 2.2b). However, when comparing these passivated 4H-SiC(0001) substrates with 4H-SiC(0001) substrates that were simply cleaned using a solvent rinsing and sonication procedure (Figure 2.2a), the root-mean-squared (RMS) surface roughness only decreased by 32% after passivation (RMS roughnesses are 1.7 and 2.5 Å, respectively), as measured by atomic force microscopy (AFM). Because this RMS roughness reduction is not as great as would be expected for fully hydrogen-passivated surfaces, passivation was attempted at higher temperatures using alumina tubes. Passivation at 1500 °C in an alumina tube results in surfaces with an observable layer of deposited particles approximately 30 nm in size (Figure 2.2c). X-ray photoelectron spectroscopy (XPS) reveals that the sample passivated at 1500 °C shows the presence of unexpected metals (including Mg and Al) and a

considerably larger oxygen peak. These elemental inclusions were concluded to be a result of etching of the inside walls of the alumina tube due to the high temperature, reducing H₂ environment, followed by the deposition of condensed vapor phase contaminants on the SiC surface. Furthermore, the underlying surface structure of the samples passivated at 1500 °C shows a very similar surface structure to non-passivated SiC substrates (Figure 2.2a), leading to the conclusion that the 4H-SiC surface passivation is impeded by the deposited particles from the alumina tube.

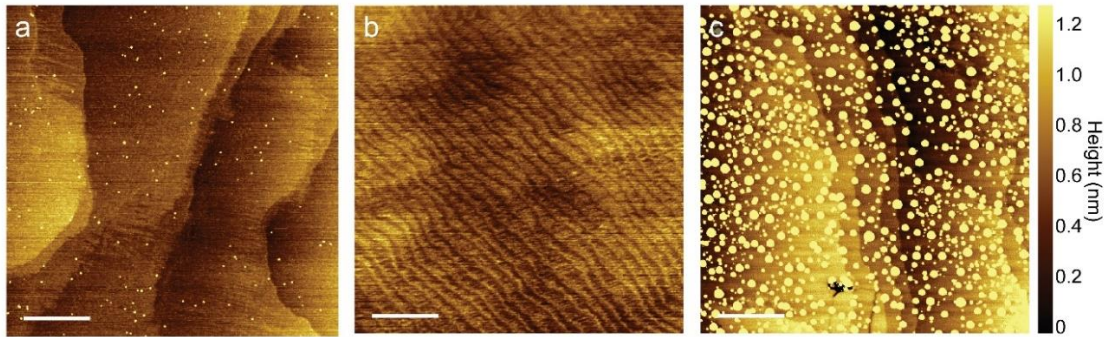


Figure 2.2. AFM height images of prepared 4H-SiC surfaces. (a) Bare 4H-SiC after solvent rinsing and sonication, (b) 4H-SiC after hydrogen passivation at 1000 °C in a quartz tube, and (c) 4H-SiC after hydrogen passivation at 1500 °C in an alumina tube. Scale bars are 1 μm .

2.4.2 Sapphire Annealing

Annealed *c*-cut sapphire substrates show sharp surface terraces with greater alignment than the passivated 4H-SiC substrates, as well as wider steps and greater height differences between terraces, as indicated by AFM imaging (Figure 2.3). The RMS roughness of this surface increases from 1.4 to 5.5 Å after annealing, but the RMS roughness of an individual terrace is reduced to approximately 0.5 Å. This is significantly

lower than the previous SiC surfaces, and corresponds to a RMS roughness reduction of over 60% between the bare and annealed substrates. Furthermore, the surface of the annealed sapphire substrate shows none of the adsorbed particles observed on SiC after H₂ passivation performed at 1500 °C, which supports the assertion that these particles visible in Figure 2.2c evolve from the alumina tube under a reducing atmosphere. Each of these observations suggest a greater degree of step flow on the sapphire surface relative to the H₂-passivated SiC.

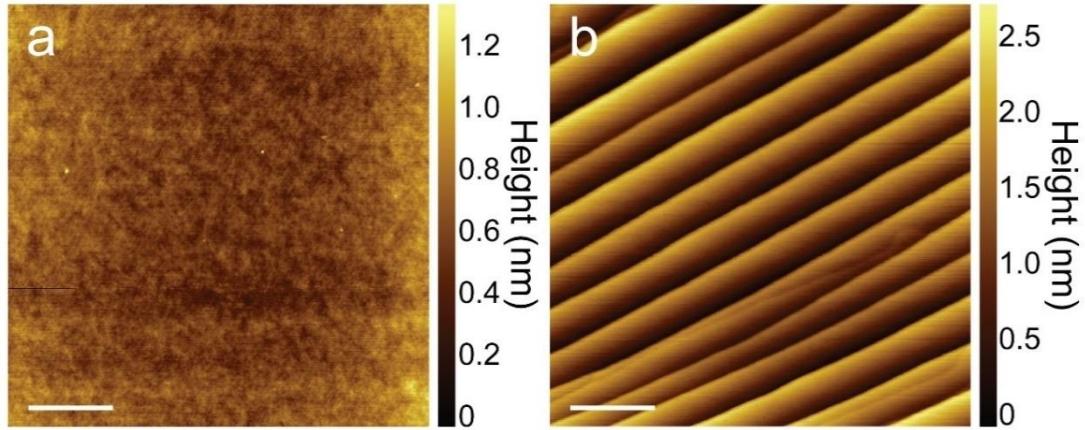


Figure 2.3. AFM height images of prepared sapphire surfaces. (a) Bare *c*-cut sapphire after solvent rinsing and sonication and (b) *c*-cut sapphire after 1500 °C annealing for 5 hours. Scale bars are 1 μm.

2.4.3 GaN Polishing

Optical observations and AFM images of the SiO₂/Si surface after initial testing of the polishing setup showed that the wear was not completely uniform (see Figure 2.4b). This induced roughness could be due to the reduced thickness and increased roughness of the Cu foil relative to the Pt foil.

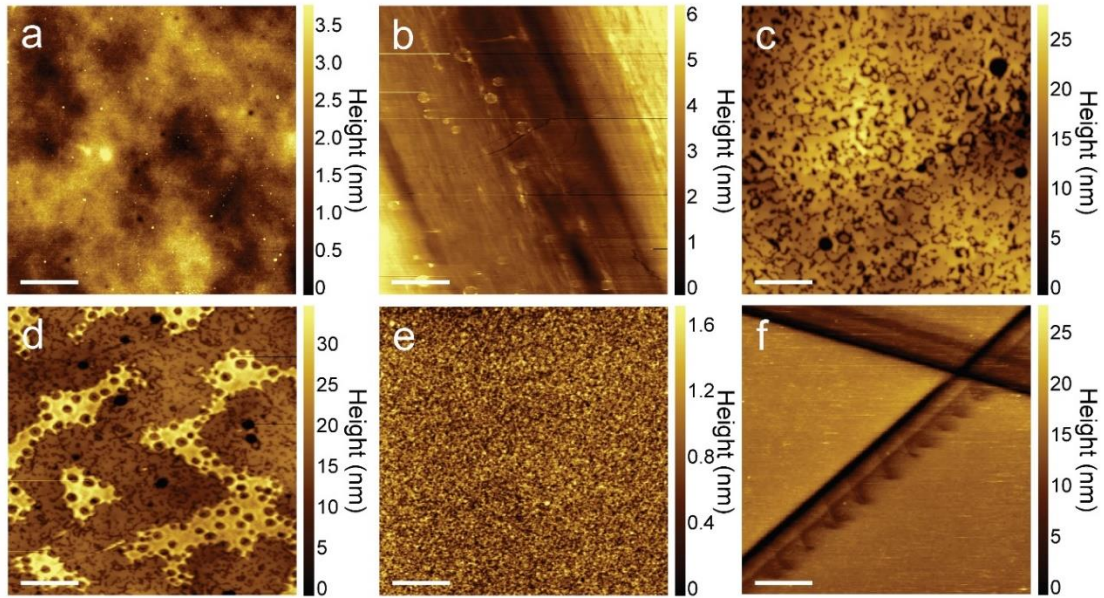


Figure 2.4. AFM height images of SiO₂/Si, GaN/Si, and single-crystal GaN surfaces. (a) SiO₂/Si before and (b) after test polishing on Cu foil, (c) GaN/Si before and (d) after electrochemical polishing on Pt foil, and (e) single-crystal GaN before and (f) after electrochemical polishing on Pt foil. All scale bars are 1 μm.

Electrochemical polishing experiments with increasing pressures and increasing polishing times show no reconstructed surface on the GaN/Si substrate, as measured by AFM. The only visible changes in the GaN/Si samples were increasing size and number of etch pits on the surface, with some areas showing large swaths of decreased height, likely due to entire regions of GaN being removed from the Si substrate beneath (Figure 2.4d). Due to these apparent problems with the stability of the GaN layer of GaN/Si substrates, I decided to repeat the electrochemical polishing using a single crystal of GaN. While GaN is not a cost-effective alternative to other CVD growth substrates, successful electrochemical polishing would allow for another reconstructed, crystalline substrate to

pursue the high-quality, large-area CVD growth of monolayer TMDCs. After cleaning and mounting the GaN substrate on the polishing apparatus, polishing was performed at the calibrated pressure for a total of one hour. AFM analysis shows that no surface reconstruction was observed on these GaN substrates. The only change observed on the surface after polishing was the presence of deep trenches, likely mechanically etched by the Pt foil.

Given the unsuccessful nature of these electrochemical polishing attempts, the use of GaN as a growth substrate was not pursued. It was concluded that previously reports of electrochemical polishing of GaN on Pt foil likely require the use of a highly sensitive and adjustable polishing setup to successfully induce the desired surface reconstruction.

2.4.4 CVD Growth of MoS₂ on Various Substrates

Scanning electron microscope (SEM) images of CVD-grown ML MoS₂ on SiO₂/Si show sharp, symmetrical, triangular flakes (Figure 2.5), but there is no detectable alignment between grains. This lack of rotational alignment is expected for growth on an amorphous surface oxide like SiO₂/Si. However, this also limits the use of SiO₂/Si as a substrate for large area ML MoS₂, because rotational misalignment prevents grain coalescence and promotes the formation of defects between merging grains. MoS₂ grown on *c*-cut sapphire shows similarly sharp and symmetrical grains, but the flakes in this case are significantly larger, up to 50 μm in length. This increase in flake length is likely a result of the hexagonal surface oxide of the Al₂O₃ allowing for van der Waals epitaxy through the coincident hexagonal superlattice of (3 × 3) MoS₂ on (2 × 2) Al₂O₃. AFM images confirm that the MoS₂ flakes on both substrates are truly monolayer in nature (Figure

2.5c–d), showing flake heights of approximately 7 Å. Furthermore, many ML MoS₂ flakes on sapphire are visibly aligned with the surface terraces visible in the sapphire after growth, suggesting that van der Waals epitaxy is present in this MoS₂ growth.

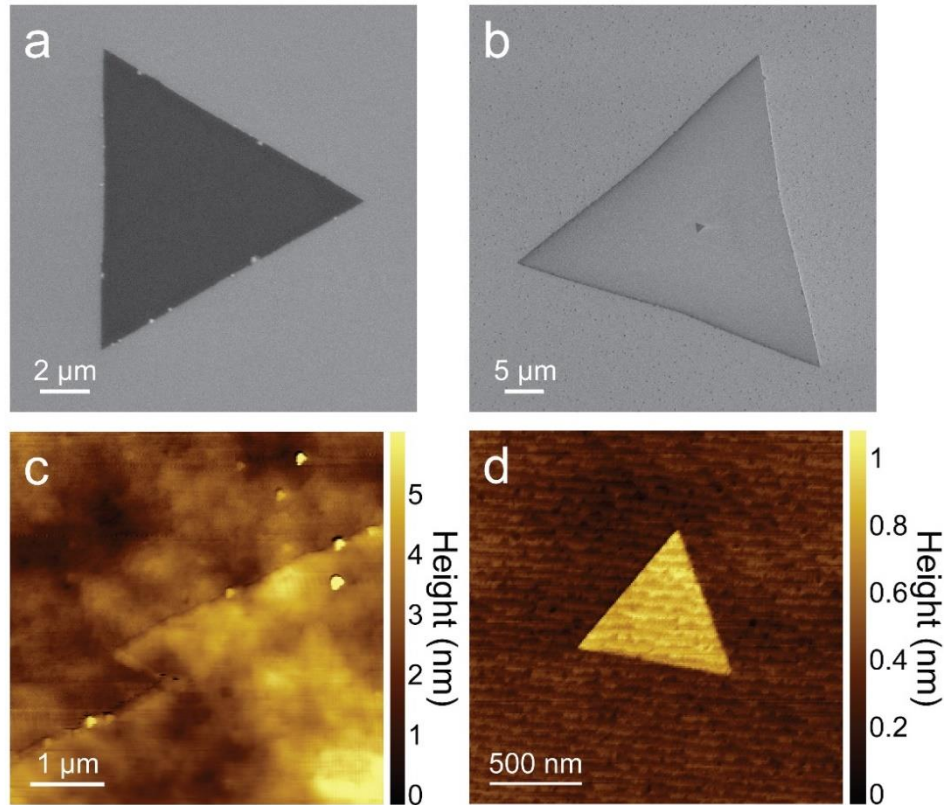


Figure 2.5. SEM and AFM images of CVD-grown ML MoS₂. ML MoS₂ is grown on (a) 90 nm SiO₂/Si and (b) *c*-cut sapphire. AFM height images of MoS₂ grown on (c) SiO₂/Si and (d) *c*-cut sapphire show that the MoS₂ is monolayer.

ML MoS₂ grown on annealed sapphire substrates shows a completely different morphology than that grown on SiO₂/Si or non-annealed sapphire (see Figure 2.6). Optical images show linear patterns of light contrast, and these samples show both the Raman and photoluminescence (PL) peaks for MoS₂, indicating the sample is monolayer in nature.

While AFM height analysis shows no distinguishable height differences corresponding to MoS₂, MoS₂ is confirmed to be present by lateral force microscopy (LFM). LFM allows for identification of materials with different magnitudes of surface adhesion, because these materials tilt the AFM cantilever laterally to different degrees, which is detectable by the instrument. LFM images in Figure 2.6d show dark regions of lower friction, which correspond to the smooth, van der Waals surfaces of the MoS₂ layers. The MoS₂ flakes grown in this system are aligned along the terrace edges of the annealed sapphire and seem to be confined to these terraces, with few flakes spreading across multiple terrace steps. It seems that the energetic penalty of growing over an edge of an annealed sapphire terrace is too large to support uniform, large-area MoS₂ growth, so the MoS₂ grows in the confined regions between terrace edges. Because of this, I used non-annealed *c*-cut sapphire wafers for all subsequent MoS₂ and TMDC growths on sapphire.

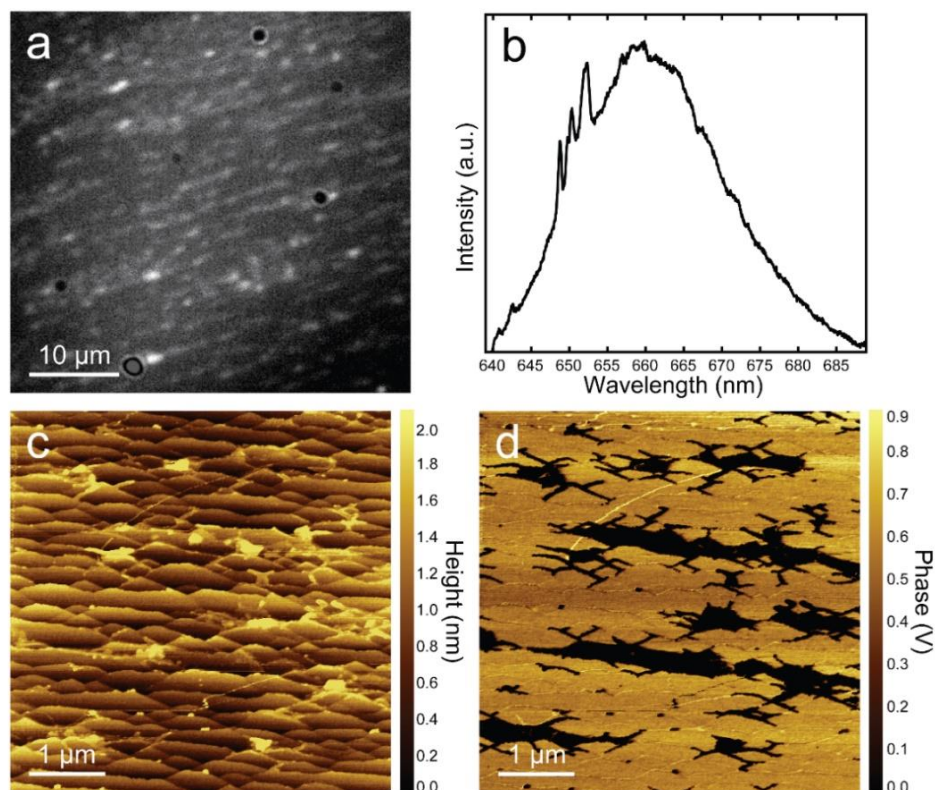


Figure 2.6. CVD growth of MoS₂ on annealed sapphire. (a) Optical image, (b) PL spectrum showing the additional presence of MoS₂ Raman peaks, (c) AFM height image, and (d) LFM friction image, acquired simultaneously with the height image, of CVD MoS₂ on annealed sapphire.

Alongside these experiments of CVD MoS₂ on annealed sapphire, I performed MoS₂ growths on bare 4H-SiC(0001). The optimized CVD growth of MoS₂ growth on SiC results in triangular flakes similar to those grown on SiO₂/Si. However, many MoS₂ flakes feature additional MoS₂ nucleated domains on the surface of the flakes, as visible in SEM images (Figure 2.7a). In the process of optimizing the CVD growth of MoS₂ on 4H-SiC, some experiments resulted in freestanding particles and platelets (Figure 2.7b). Some of these platelets appear to have different material contrast on the interior and exterior (Figure 2.7c), leading to the identification of these as core/shell plates comprised of MoO₂ cores

and MoS₂ shells. This intermediate growth condition, in which both MoS₂ and core/shell plates are observed, was also achieved on *c*-cut sapphire substrates (Figure 2.7d), but these samples are notably more difficult to image in SEM, given that sapphire is an insulating substrate and is prone to charging effects. Given the intriguing core/shell nature of these plates and their apparent alignment, I subsequently optimized the CVD growth process to select for these platelets grown on SiC and analyzed their composition and structure. The growth and mechanism of these MoO₂/MoS₂ core/shell plates will be discussed in further detail in Chapter 4.

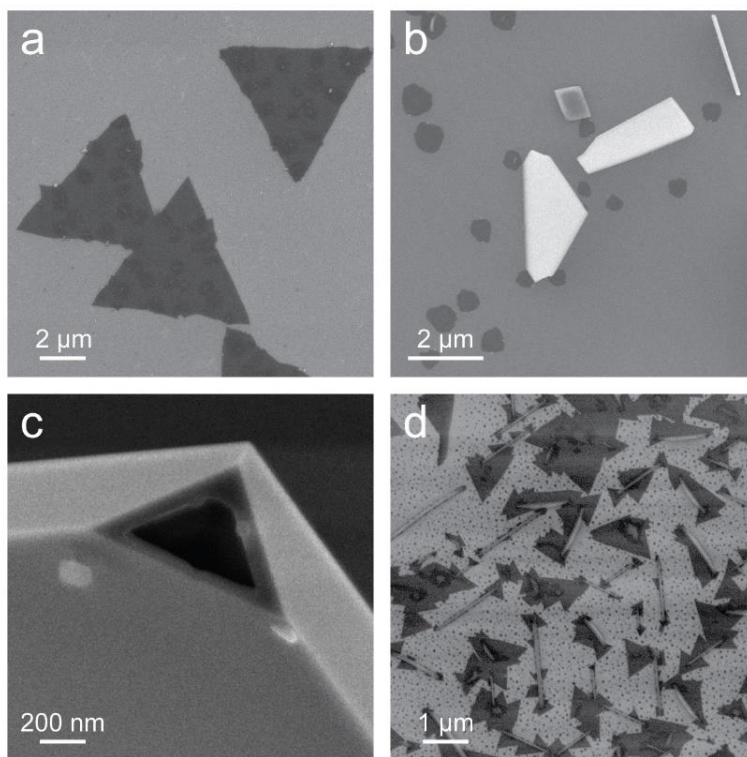


Figure 2.7. SEM images of MoS₂ and MoO₂/MoS₂ growths on 4H-SiC. (a) CVD growth of MoS₂ on 4H-SiC, (b) CVD growth of MoS₂ on 4H-SiC using slightly altered reaction conditions, showing presence of freestanding plates, (c) core/shell plate with truncated corner, showing the core/shell nature of these plates, and (d) MoS₂ and core/shell plates as grown on *c*-cut sapphire.

2.4.5 NbS₂ CVD Growth

Representative NbS₂ flakes synthesized on *c*-cut sapphire from oxide precursor can be seen in Figure 2.8. Optical images show symmetrical, triangular flakes with bright optical contrast. This contrast is significantly brighter than other mono- or few-layer TMDCs, which implies that the materials are much thicker. This is supported by AFM height image and profile traces, which show that the flakes are ~50 nm in thickness. The Raman spectra of representative NbS₂ flakes synthesized from Nb₂O₅ show the E₁ and E₂ modes for NbS₂, but none of the other expected Raman modes are present. The absence of other Raman modes in these NbS₂ flakes is likely due to a large concentration of defects, but more research would need to be done to confirm this.

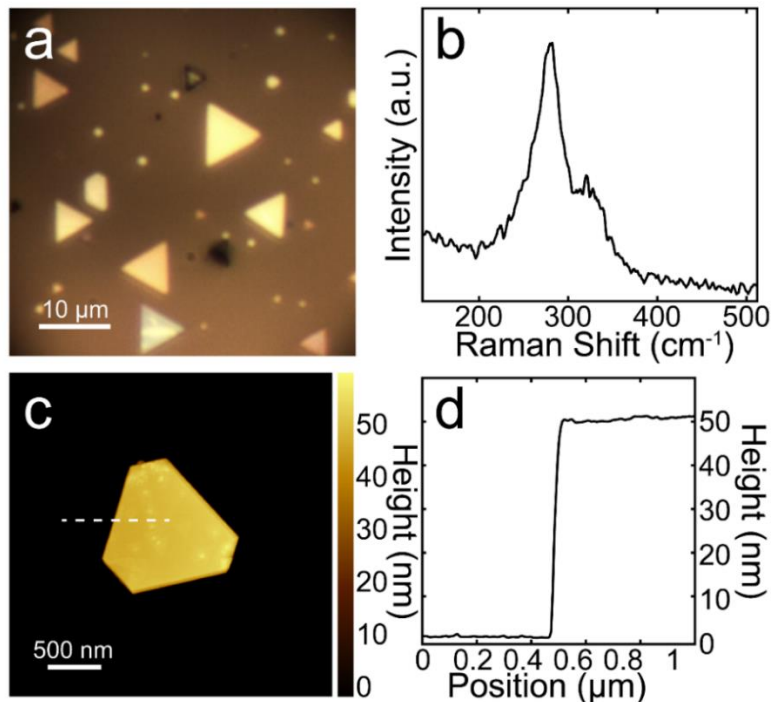


Figure 2.8. NbS₂ flakes synthesized from the oxide-based CVD method. (a) Optical image, (b) Raman spectrum, (c) and AFM height image of representative oxide-based NbS₂ flakes. (d) AFM profile trace along the dashed line in (c).

Many optimization experiments were performed with the intention of decreasing the thickness of these bulk-like NbS₂ flakes, but ultimately none were successful. The thickness of these flakes is likely related to the extreme temperatures required to evolve the Nb₂O_{5-x} precursor. I then decided to pursue the growth of 2D NbS₂ using a significantly more volatile chloride-based precursor, NbCl₅.

Representative NbS₂ flakes synthesized on *c*-cut sapphire from chloride precursor can be seen in Figure 2.9. Optical images show that many flakes have rough, asymmetrical morphologies with stripes of higher optical contrast than most of the flake. The low contrast of most of the flake surface is expected for flakes that are mono- or few-layer, whereas the high contrast of the stripe region likely indicates local regions of multi-layer NbS₂. The

localization of these multi-layer stripes and the rough, asymmetrical morphology of the flakes are likely due to poor surface diffusion at the reduced temperature of 900 °C. Raman spectra of these flakes clearly show all expected Raman modes for 3R NbS₂, but additional structural analysis is needed to confirm the phase (see Section 5.4.3). AFM height images and profile traces show that these flakes are ~2 nm in height, indicative of few-layer NbS₂ (~3–4 layers). Furthermore, the surface of the flakes are somewhat rough, with apparent grain boundaries and gaps in the flake structure. This surface structure is likely a result of insufficient surface diffusion and in-situ etching from residual chlorine-based species resulting from the use of NbCl₅ precursor.

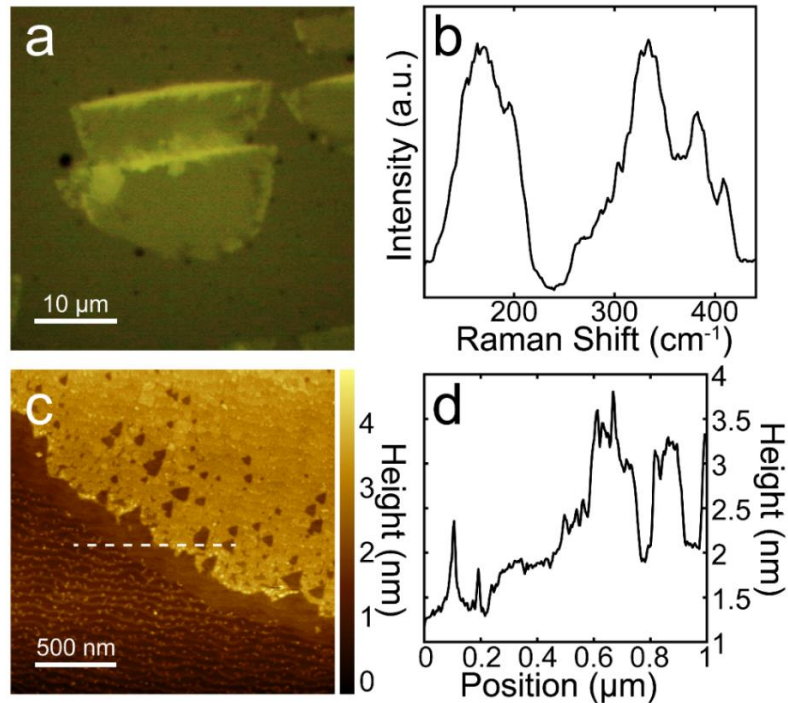


Figure 2.9. NbS₂ flakes synthesized from the chloride-based CVD method. (a) Optical image, (b) Raman spectrum, (c) and AFM height image of representative chloride-based NbS₂ flakes. (d) AFM profile trace along the dashed line in (c).

With this data, I have demonstrated the successful CVD growth of few-layer NbS₂ on *c*-cut sapphire substrates. However, it is apparent that the resulting flakes from both techniques are not nearly as thin or uniform as those of other TMDCs I have grown, including the ML MoS₂ described above and the ML WS₂ that will be described in the following chapters. The quality of both the oxide-based and the chloride-based NbS₂ is likely limited by the precursor in each of these growth schemes. In the oxide-based growth, the low vapor pressure of Nb₂O₅ requires the use of sufficiently high reaction temperatures at which bulk NbS₂ flakes are unavoidable. In the chloride-based growth, the high reactivity of NbCl₅ and other chlorine-based byproducts likely results in film etching that appears to compete with the surface diffusion and flake growth. To perform more uniform, high-quality growth of ML NbS₂, future experiments should use alternative niobium-containing precursors, as they may allow for more control over the growth morphology.

2.4.6 WSe₂ CVD Growth and Selenization

Initial growths of ML WSe₂ can be seen in Figure 2.10. Optical images show clear triangular flakes, and representative Raman and PL spectra show Raman peaks and strong PL signal expected for monolayer WSe₂. These WSe₂ flakes are further confirmed to be monolayers by AFM height imaging. Height profiles show that the flakes have thickness of ~ 7 Å, indicative of the monolayer thickness. However, the as-grown WSe₂ monolayers are quite air sensitive, generally decomposing in less than one day in air. The beginning stages of this decomposition can be observed in the AFM image in Figure 2.10d, indicated by the small bumps on the WSe₂ surface and the larger particles at the WSe₂ edges. Thus,

I performed experiments to stabilize the as-grown WSe₂ through the use of a selenization procedure.

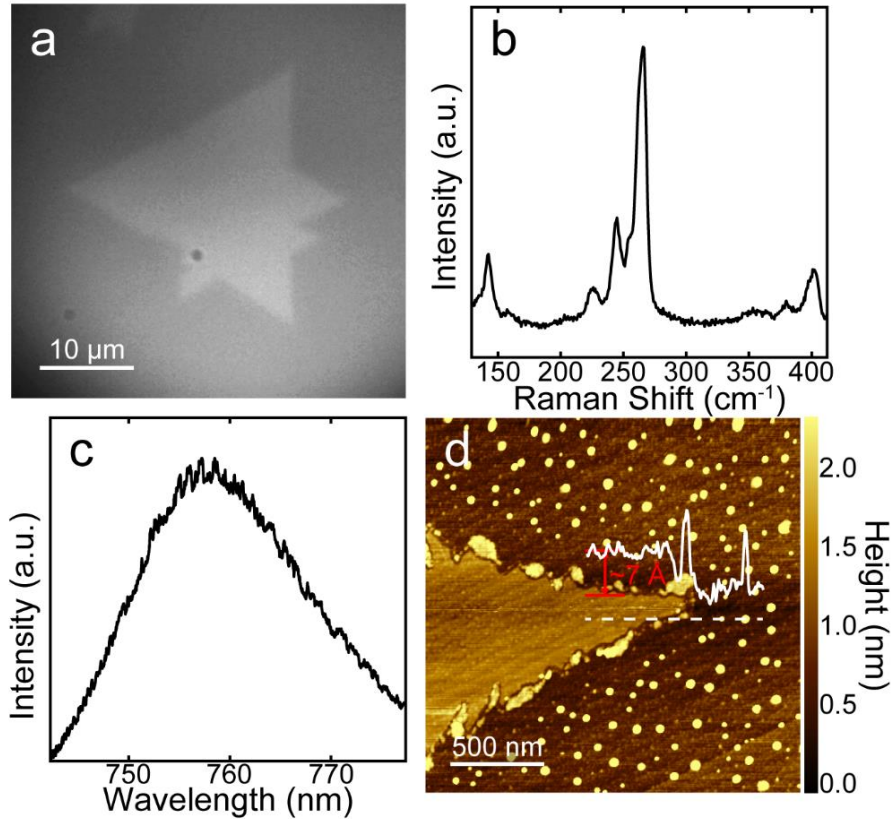


Figure 2.10. CVD-grown ML WSe₂. (a) Optical image, (b) Raman spectrum, (c) PL spectrum, and (d) AFM height image of monolayer WSe₂. Inset profile trace in (d) corresponds with the white dashed line in (d).

The results of WSe₂ selenization can be seen in Figure 2.11. After selenization, the WSe₂ flakes appear to be quite stable in air, retaining shape and Raman/PL character after more than 20 days in air. However, selenization appears to induce some undesirable effects in the resulting WSe₂ morphology. The resulting flakes show asymmetrical shape, and some higher-contrast regions are visible among the otherwise uniform flake surface in

optical images. These higher-contrast regions are corroborated in AFM images, appearing to show local few-layer thicknesses of ~ 3 nm, compared to the otherwise uniformly monolayer ~ 7 Å thickness. Despite the non-ideal flake morphologies of these selenized WSe₂ flakes, they should prove suitable for future applications and study.

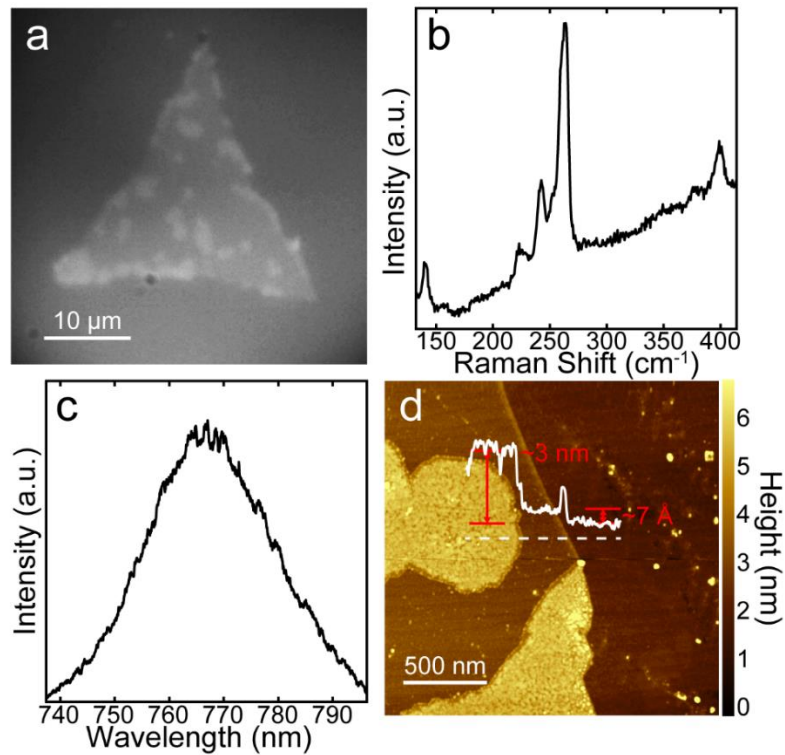


Figure 2.11. ML WSe₂ after selenization. (a) Optical image, (b) Raman spectrum, (c) PL spectrum, and (d) AFM height image of monolayer WSe₂ after selenization. Inset profile trace in (d) corresponds with the white dashed line in (d).

2.5 Conclusion

Here, I demonstrate the investigation into the preparation of a variety of synthetically relevant substrate surfaces, including 4H-SiC, *c*-cut sapphire, SiO₂/Si, GaN/Si, and GaN. These substrate surfaces were modified with passivation, annealing, and

electrochemical polishing methods, respectively. 4H-SiC was shown to exhibit a small amount of step flow under moderate passivation conditions, but higher temperature passivation resulted in no observable step flow due to obstruction by contaminants from the tube under the high-temperature, reducing environment. *c*-cut sapphire shows a great deal of step flow after high-temperature ambient annealing, with the resulting terraces showing very smooth surfaces and large step heights. SiO₂/Si, GaN/Si, and GaN show some rough etching as a result of the polishing, but no surface reconstruction or smoothing is observed. Few of the surface preparation methods discussed here resulted in ideal substrates for large-area TMDC growth, but they demonstrate ways in which substrate surfaces can be modified and tailored for specific applications.

After preparing these substrate surfaces, some were used for the CVD growth of a variety of 2D TMDCs, including MoS₂, NbS₂, and WSe₂. MoS₂ growth on bare SiO₂/Si and *c*-cut sapphire substrates show large area, monolayer flakes in both cases, but MoS₂ grown on sapphire shows that the grains are generally aligned to the surface terraces of the substrate. MoS₂ grown on annealed *c*-cut sapphire shows irregular, asymmetrical flakes confined to terrace step edges. MoS₂ grown on 4H-SiC shows rotationally disordered grains with few-layer regions, and with some minor synthetic modifications, the presence of core-shell plates, which will be discussed in more detail in Chapter 4. NbS₂ grown on *c*-cut sapphire via Nb₂O₅ precursor show bulk-like flakes, whereas NbS₂ grown via NbCl₅ precursor show asymmetrical but few-layer flakes. WSe₂ grown on *c*-cut sapphire shows sharp, symmetrical, monolayer flakes that degrade quickly in air. Subsequent selenization of these WSe₂ flakes improves their stability in air and retains monolayer thickness in some regions, despite inducing regions of few-layer thickness in other regions. With this data, I

show that these high-quality materials can be reproducibly synthesized through optimization and synthetic control on relevant substrates. It is also demonstrated that the choice of substrate and surface preparation can have a dramatic effect on the resulting TMDC growth. The TMDCs grown here will be extended to a variety of novel heterostructures in the subsequent chapters of this dissertation.

Chapter 3

2D Material Semiconductor Heterostructures

3.1 Preface

Atomically thin, TMDC semiconductor heterostructures show promise for next-generation electronics and optoelectronics, and control of these heterostructures without interfacial contamination is essential for utility. Here, I describe a controllable, two-step CVD process for lateral and vertical heteroepitaxy between ML WS₂ and ML MoS₂ on *c*-cut sapphire. Lateral and vertical heteroepitaxy can be selectively achieved in this system by careful control of the ML MoS₂ growth that is used as a 2D seed crystal. Ultraclean MoS₂ monolayers are grown using hydrogen as a carrier gas, which enables lateral heteroepitaxial growth of ML WS₂ from the MoS₂ edges, thereby creating atomically coherent, in-plane WS₂/MoS₂ heterostructures. When no hydrogen is used, the as-grown ML MoS₂ is decorated with small particles along the edges, inducing vertical heteroepitaxial growth of ML WS₂ on top of the MoS₂ to form vertical WS₂/MoS₂ heterostructures. This lateral and vertical atomic layer heteroepitaxy steered by seed defect engineering opens a new avenue toward atomically controlled fabrication of 2D heterostructure architectures.

3.2 Introduction

3.2.1 Semiconductor Heterostructures

Semiconductor heterostructures are material systems in which two or more semiconducting materials are directly interfaced. By nature of interfacing two different semiconductors, the band structure position can be independently controlled in each material, thereby offering new possibilities for device functionality. These materials can align their bands in one of three different ways (Figure 3.1).⁷⁰ In type I heterostructures,

the conduction band (CB) and valence band (VB) of one semiconductor entirely straddle that of the CB and VB of the second. In type II heterostructures, the CB and VB of the first semiconductor are staggered relative to the CB and VB of the second, such that the CB and VB of one semiconductor are above the CB and VB of the other semiconductor but neither VB is above either CB. In type III heterostructures, the CB and VB of one semiconductor are above both the VB *and* CB of the other semiconductor, with no overlap between the two band gaps. The relative and absolute positions of these bands dictate the properties of the heterostructure and the applications for which the heterostructure can prove technologically useful.

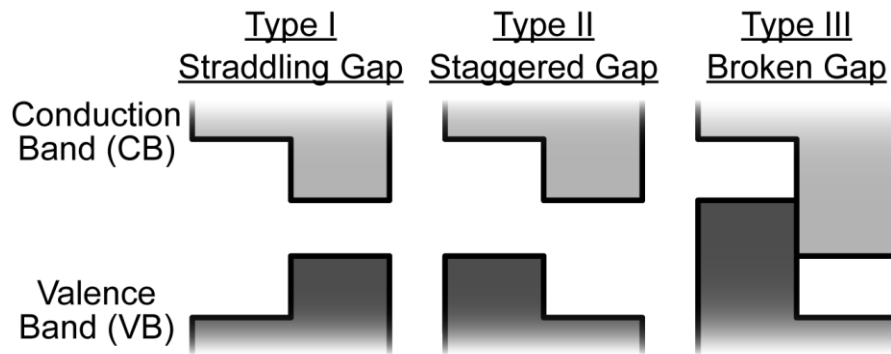


Figure 3.1. Schematic illustrating the band alignment of the three types of semiconductor heterostructures.

3.2.2 2D Material Heterostructures

Heterostructures composed of 2D TMDCs show promise as building blocks for a variety of device applications.² 2D semiconductor heterostructures are quite different than 3D semiconductor heterostructures because the 2D materials act both as the bulk material and interface, simultaneously. This reduces the amount of charge displacement within each

layer, but allows for interesting possibilities in the context of band-structure engineering.⁷¹ Furthermore, the mechanical flexibility and low material thickness of 2D materials are enticing in the context of novel device fabrication.

Some of the first 2D TMDC heterostructures were fabricated by micromechanical exfoliation of bulk crystals followed by vertical stacking of the layers.^{72,73} Vertical stacking of WS₂/MoS₂ or WSe₂/MoS₂ creates type II heterostructures, as described above, but the electronic properties of these heterostructures are quite sensitive to many subtle details of the transfer process, including twist angle and the presence of interfacial debris.⁷²⁻⁷⁵ It has also been reported that both vertical and in-plane heterostructures of monolayer WS₂/MoS₂ can be grown via a single-step CVD process, which allows for a greater degree of control over the heterostructure morphology and properties.⁷⁶

3.2.3 MoS₂/WS₂ Ultraclean Heterostructures

Heteroepitaxy, as described in Chapter 2, can be used to grow in-plane TMDC heterostructures unobtainable by any exfoliation or transfer-based techniques. In-plane junctions created using this method have appealing optoelectronic properties, including a linearly abrupt p-n junction.⁷⁶ Previous reports of these heterostructures feature only a single synthetic step, which limits the amount of control one can exert over important physical features, such as particle size, shape location, and junction width.^{76,77} To this end, a two-step process is desirable, as it could allow for patterned 2D heterostructures and independent growth control of each individual material. Multi-step growth procedures such as these have been reported for graphene and hexagonal boron nitride heterostructures.⁷⁸⁻

Creating in-plane (lateral) heterostructures can be difficult due to challenges with preventing contamination of the seed crystal. Adsorbates, defects, or particles persisting after the growth of the first material can function as unintended nucleation sites when depositing the second material and can induce additional material growth in undesirable locations.⁸³ Thus, a two-step process for fabricating lateral heterostructures composed of monolayer WS₂/MoS₂ demands meticulous care in preparing clean surfaces and edges of the 2D seed crystals.

We show that a two-step CVD process can be used to selectively achieve lateral and vertical heteroepitaxy between monolayer WS₂ and MoS₂ through careful growth control of monolayer MoS₂ seed crystals. Including H₂ in the carrier gas results in ultraclean MoS₂ monolayers. These ultraclean MoS₂ flakes suppress the nucleation and growth of additional vertical layers and facilitate the lateral heteroepitaxial growth of monolayer WS₂, culminating in atomically coherent in-plane WS₂/MoS₂ heterostructures. Without the use of H₂, CVD-grown MoS₂ monolayers are decorated with small particles along the edges. These particles nucleate vertical heteroepitaxial growth during subsequent growth of WS₂, thereby forming vertical WS₂/MoS₂ heterostructures with perfect alignment. This work is reproduced with permission from Yoo, et al.⁸⁴

3.3 Experimental

Ultraclean MoS₂ monolayers were synthesized in a horizontal hot-wall three-zone tube furnace (ThermoFisher Blue M, with only the center zone being heated), equipped with a vacuum pump (Edwards RV-8) and mass flow controllers (MTI Corp.). An alumina boat (50 × 20 × 20 mm, MTI Corp.) containing 400 mg MoO₃ powder (99.999%, Acros

Organics) was placed at the center of the furnace in a 3-inch diameter quartz tube. A *c*-cut sapphire substrate (MTI Corp.) was placed polished-face-up on an upside-down alumina boat placed directly downstream from the boat containing MoO₃ powder. 800 mg S powder (99.999%, Alfa Aesar) was located upstream, maintained at a reduced temperature during the reaction (approximately 280 °C at the peak of the reaction). After loading, the tube was evacuated to less than 100 mTorr, and Ar and H₂ gases were supplied at rates of 20 and 4 sccm (standard cubic centimeters per minute), respectively. The reaction was carried out under atmospheric pressure. The center of the furnace (and thus the substrate and MoO₃ powder precursor) was heated to 710 °C at a rate of 22 °C/min and kept at 710 °C for 5 min. After the reaction, the furnace was rapidly cooled by opening the lid of the furnace. At this point, the Ar gas flow was increased to 200 sccm, to purge any toxic vapors. The experimental conditions for the growth of MoS₂ monolayers decorated with particles are the same as those for the growth of ultraclean MoS₂ monolayers except that no H₂ carrier gas is used.

To synthesize WS₂/MoS₂ heterostructures, monolayer MoS₂ grown on *c*-cut sapphire was used as a substrate for the subsequent growth of WS₂. 500 mg WO₃ powder (99.998%, Alfa Aesar) was placed at the center of the furnace in a 2-inch diameter quartz tube. The substrate was placed a few centimeters downstream from the center of the furnace and the sulfur powder was placed upstream (at temperatures of approximately 940 °C and 160 °C, respectively, during the peak of the reaction). Ar and H₂ gases were introduced at rates of 60 and 5 sccm, respectively, maintaining a chamber pressure of 350 mTorr during the growth. The center of the furnace (and thus the WO₃ powder precursor) was heated to 1050 °C at a rate of 11 °C/min and kept at 1050 °C for 5 min. The furnace was rapidly

cooled down after the reaction by opening the lid of the furnace. In-plane WS₂/MoS₂ heterostructures were synthesized when ultraclean monolayer MoS₂ on sapphire was used as a substrate, while vertical WS₂/MoS₂ heterostructures were synthesized when the monolayer MoS₂ decorated with particles on sapphire was used as a substrate.

The atomic structure of the lateral heterostructure is characterized by Z-contrast STEM imaging using an aberration-corrected STEM (FEI Titan G2) operated at an accelerating voltage of 60 kV. Prior to imaging, samples were transferred onto transmission electron microscopy (TEM) grids using a wet chemical transfer process. First, a 5% solution of poly(methyl methacrylate) (PMMA, MW ~996,000, Sigma Aldrich) in anisole was spin-coated onto WS₂/MoS₂ heterostructures grown on *c*-cut sapphire (3000 rpm rotation for 1 min). After coating, the sample was baked on a hot plate at 50 °C for 10 min. The underlying sapphire substrate was etched in a 30% aqueous solution of KOH (Fisher Scientific) for several hours, etching the top layer of the substrate surface and delaminating the substrate. The PMMA with adhered WS₂/MoS₂ heterostructures was then rinsed in deionized water and transferred onto a TEM grid. To remove the PMMA film residue, the sample was cleaned with ~10 drops of acetone and then annealed in a tube furnace at 350 °C with 100 sccm of H₂ and Ar gas at atmospheric pressure. After subsequent loading into the TEM, samples were annealed at 160 °C for 4 hours under vacuum to avoid hydrocarbon contamination.

AFM measurements were acquired using a Bruker Nanoscope V Multimode 8 scanning probe microscope in the Characterization Facility at the University of Minnesota. Raman and photoluminescence spectra were acquired using a home-built Raman setup

using a 632.8 nm continuous wave laser focused through a 100× objective lens with a beam power of ~30–300 μm .

In this work, I performed the characterization of the MoS₂/WS₂ heterostructures via AFM and KPFM, and HRTEM atomic diffusion analysis. I also contributed intellectually to the realization of these experiments and have since replicated their results. Youngdong Yoo performed the entirety of the synthesis of these heterostructures, as well as characterization via AFM, Raman, PL, SEM, and TEM.

3.4 Results and Discussion

Figure 3.2 shows the comparison between triangular monolayer flakes of MoS₂ grown with and without H₂ included in the carrier gas stream. Under typical CVD conditions (without H₂), the edges of the MoS₂ flakes are decorated by small particles, as shown by AFM. Similar particles to those seen in our flakes have been observed in other reports of MoS₂ synthesis. The inclusion of 4 sccm H₂ into the carrier gas stream during the synthesis prompts the disappearance of these particles. The ultraclean nature of these monolayer MoS₂ flakes is confirmed by AFM height images and line profiles, which show no presence of particles. In both cases (H₂ included and excluded), the flakes are confirmed to be monolayer by AFM, showing flake thicknesses of approximately 0.7 nm, consistent with previous reports of monolayer MoS₂.^{85–92} SEM analysis of ML MoS₂ grown with and without hydrogen is visible in Figure 3.3

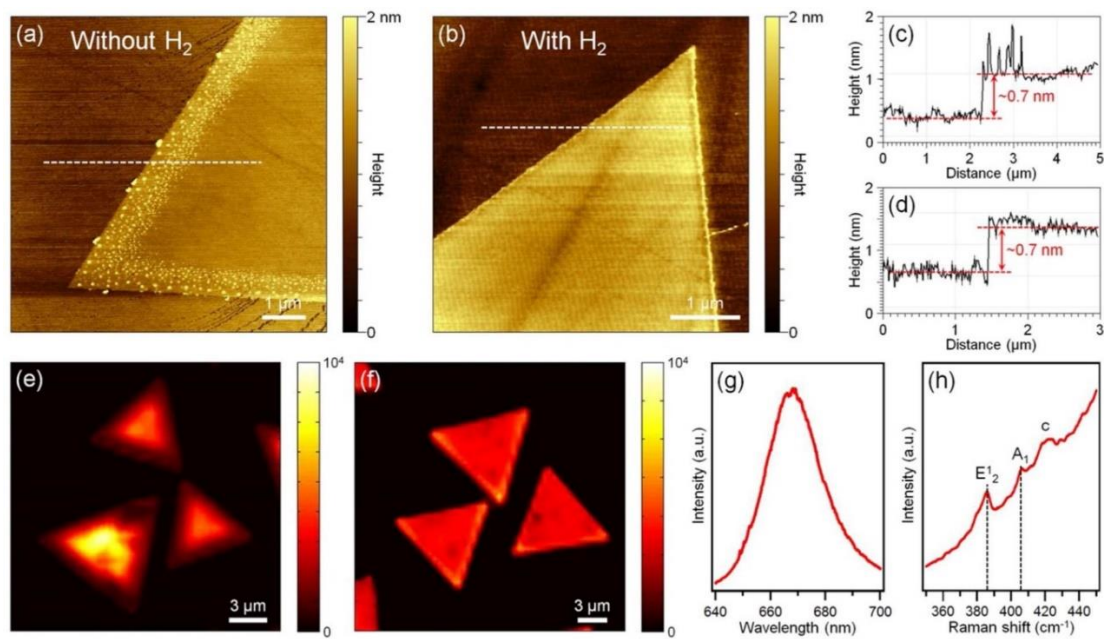


Figure 3.2. Monolayer MoS₂ crystals synthesized on *c*-cut sapphire without and with hydrogen gas. AFM height images of monolayer MoS₂ grown (a) without, and (b) with hydrogen, respectively. (c,d) Height line profiles along the dotted white lines in (a) and (b), respectively. PL intensity maps of monolayer MoS₂ grown (e) without and (f) with hydrogen, respectively. (g) PL and (h) Raman spectra of ultraclean monolayer MoS₂. This figure is reproduced with permission from Yoo, et al. *J. Am. Chem. Soc.* **2015**, *137* (45), 14281–14287.⁸⁴

The monolayer nature of the synthesized MoS₂ seed crystals is also confirmed by Raman spectroscopy. The Raman spectrum of MoS₂ shows two characteristic peaks: the out-of-plane vibration of the S atoms (A₁) and the doubly degenerate in-plane vibrations of the Mo and S atoms (E₂).⁹³ The energy of the phonons associated with these vibrational modes changes with sample thickness, and thus the spectral separation of these two Raman peaks has become a common tool for determining the number of layers in a given sample of MoS₂. In these samples, the MoS₂ flakes exhibit a peak separation of 20.3 cm⁻¹, which is in good agreement with previous reports of monolayer MoS₂ syntheses.

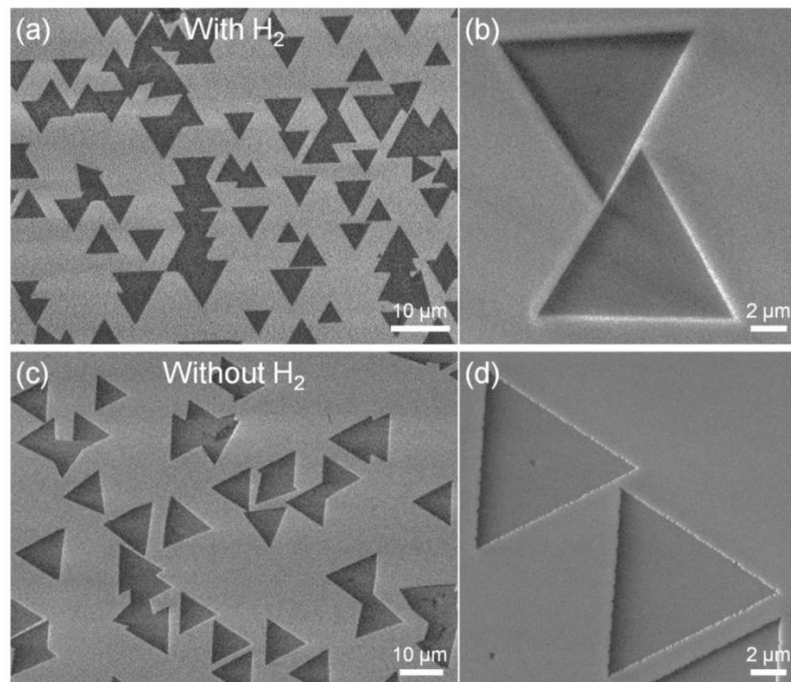


Figure 3.3. SEM images of monolayer MoS₂ grown (a,b) with and (c,d) without hydrogen, respectively. This figure is reproduced with permission from Yoo, et al. *J. Am. Chem. Soc.* **2015**, *137* (45), 14281–14287.⁸⁴

The MoS₂ Raman spectrum shown in Figure 3.2h was acquired on resonance with the B exciton absorption band. Resonance Raman spectra can exhibit spectral changes including line-broadening, large fluorescence backgrounds, and additional non-zone-centered modes. Additional modes are observed in the resonance spectra that are not visible in the off-resonance Raman spectra.^{93,94} To obtain a more accurate measurement of the separation between MoS₂ Raman peaks, spectra were acquired using the off-resonance excitation of a 514.5 nm continuous wave laser. These spectra show no spectral congestion, increased signal-to-noise, and a MoS₂ peak separation of 17 cm⁻¹. The source of this decreased splitting could be due to enhanced substrate interactions, but further study is

needed to confirm this. Raman spectra and Lorentz fitting for ML MoS₂ can be seen in Figure 3.4.

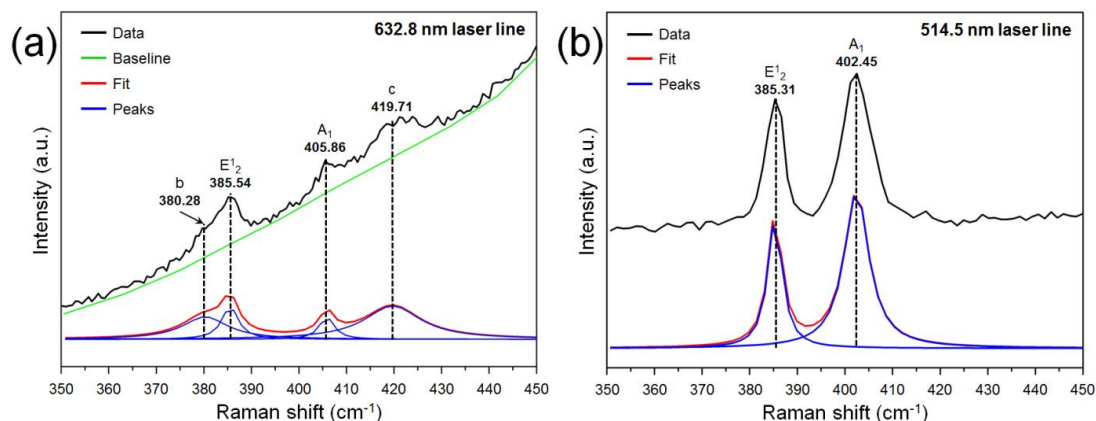


Figure 3.4. Raman spectra and Lorentz fitting results for monolayer MoS₂. (a) Raman spectrum of a monolayer MoS₂ flake excited by a 632.8 nm HeNe laser. (b) Raman spectrum of a monolayer MoS₂ flake excited by a 514.5 nm Ar⁺ ion laser. This figure is reproduced with permission from Yoo, et al. *J. Am. Chem. Soc.* **2015**, *137* (45), 14281–14287.⁸⁴

PL spectroscopy confirms that the inclusion of H₂ gas leads to a cleaner and more homogeneous material. Figure 3.2g shows a PL spectrum acquired at room temperature on ultraclean monolayer MoS₂, exhibiting a strong A-exciton peak at 667 nm stemming from the direct band gap of MoS₂.^{21,95} PL intensity maps of the emission from the A exciton of monolayer MoS₂ grown without H₂ gas is spatially heterogeneous and shows a faint ~1 μm ribbon with reduced intensity, due to partial quenching of the PL. PL intensity maps of MoS₂ grown with H₂ are highly uniform, indicating uniform chemical composition and electronic structure.

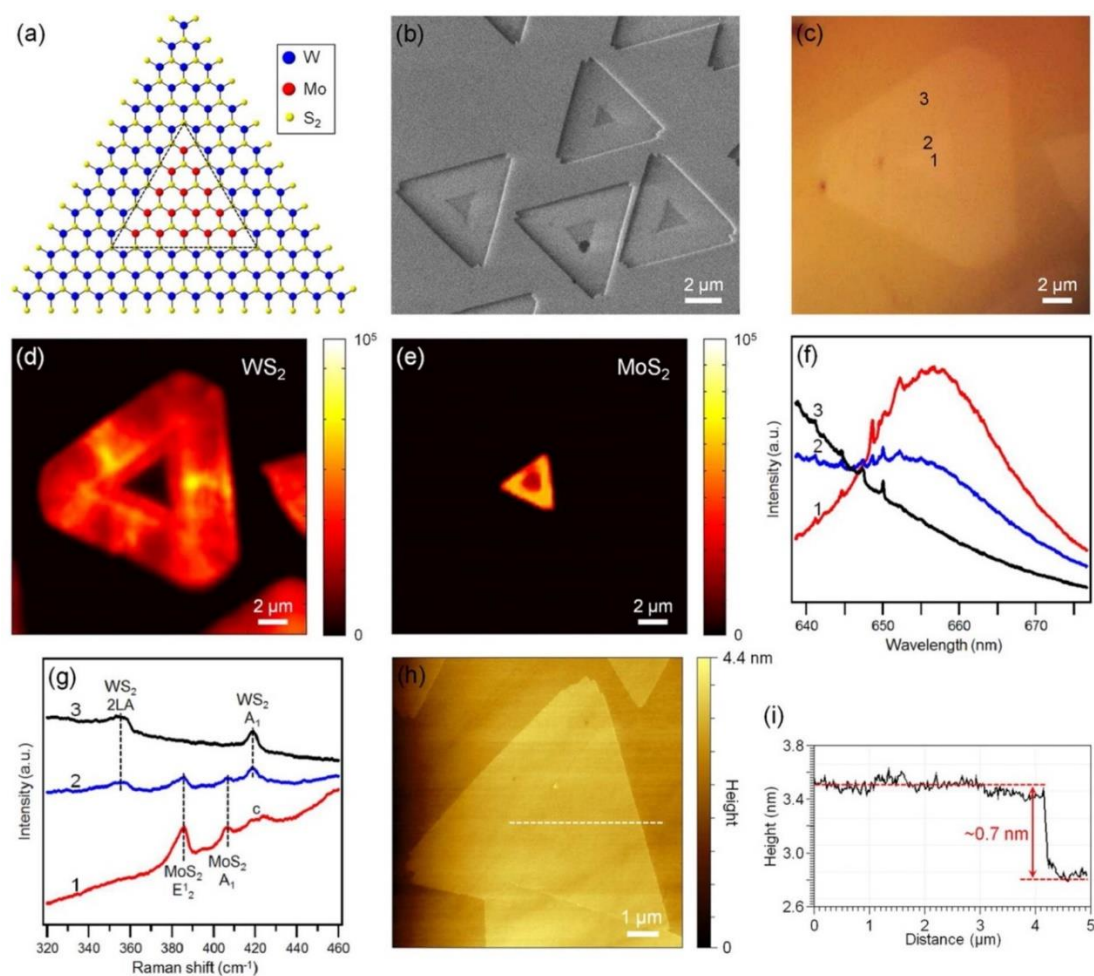


Figure 3.5. In-plane heteroepitaxial WS₂/MoS₂ monolayers synthesized from monolayer MoS₂ grown with hydrogen. (a) Atomic model of an in-plane heteroepitaxial junction between MoS₂ and WS₂. (b) SEM image and (c) optical image of the in-plane heteroepitaxial monolayers. (d,e) PL intensity mapping of WS₂ and MoS₂ from the in-plane heteroepitaxial monolayer, respectively. (f) PL and (g) Raman spectra taken from the points marked by 1–2 in (c). (h) AFM height image of the in-plane heteroepitaxial monolayer, with the height line profile in (i) acquired along the dotted white line in (h). This figure is reproduced with permission from Yoo, et al. *J. Am. Chem. Soc.* **2015**, *137* (45), 14281–14287.⁸⁴

c-cut sapphire is an ideal choice of substrate, because the surface is atomically flat and it has been previously shown to improve the crystallinity of CVD-grown MoS₂ and WS₂.^{96,97} Furthermore, the lattice mismatch between the sapphire substrate and supercells

of MoS₂ and WS₂ is quite low – only 0.42% and 0.64% for (3 × 3) MoS₂ and (3 × 3) WS₂ supercells on (2 × 2) sapphire(0001), respectively. The MoS₂/WS₂ lateral heterostructures are oriented along two preferential directions on the substrate, thereby indicating that the heteroepitaxial monolayers are grown with van der Waals epitaxy on the *c*-cut sapphire surface.

PL spectra acquired from the inner triangle and outer ribbon of lateral heterostructures (Figure 3.5f) show strong PL signals from MoS₂ and WS₂, respectively, due to emission from the lowest energy A excitons of the respective TMDCs.^{21,95,98,99} The interface region between the two TMDCs shows PL signal from both WS₂ and MoS₂, as expected. PL intensity maps of the A exciton from WS₂ and the A exciton from MoS₂ demonstrate that the in-plane junctions are monolayer and have mutually exclusive domains, with no MoS₂ PL present in the WS₂ region and vice versa. The PL intensity variations visible in the maps could be due to nonuniform strain induced by the lattice mismatch between the substrate and MoS₂/WS₂ or the difference in thermal expansion coefficients between the substrate and MoS₂/WS₂.^{100,101} These effects could also lead to the variation of Raman peak positions. In accordance with the PL maps, Raman spectra of the inner triangle of the lateral heterostructures show E₂¹ and A₁ peaks of MoS₂, and Raman spectra of the outer ribbon show peaks corresponding to the 2LA and A₁ phonons of monolayer WS₂. Raman signals of both WS₂ and MoS₂ are observed in the junction region. Raman peak position maps of the 2LA and A₁ modes of WS₂ from in-plane heterostructures are also visible in Figure 3.6.

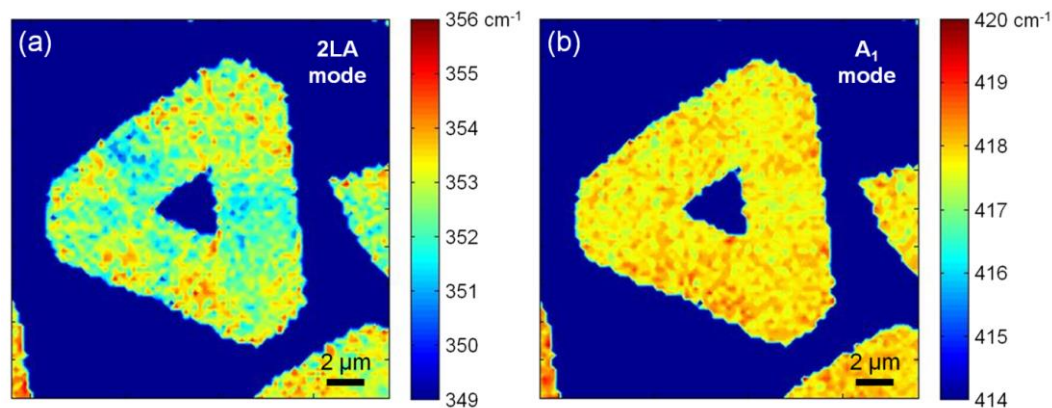


Figure 3.6. (a,b) Raman peak position mapping at the 2LA and A_1 modes of WS_2 from in-plane heterostructures, respectively. This figure is reproduced with permission from Yoo, et al. *J. Am. Chem. Soc.* **2015**, *137* (45), 14281–14287.⁸⁴

AFM height images of the in-plane heterostructure and line profiles across these flakes show that the MoS_2/WS_2 heterostructures are indeed monolayer, with both materials in the same plane and each possessing a height of 0.7 nm (Figure 3.5h). The lateral force microscopy (LFM) friction image clearly shows the lateral junction between the MoS_2 and WS_2 domains, likely due to subtle friction differences in the resulting TMDCs (Figure 3.7). Furthermore, Kelvin probe force microscopy (KPFM) data confirms that as-synthesized heterostructures have high-quality lateral junctions (Figure 3.8), with the MoS_2 and WS_2 domains showing clear contrast corresponding to the difference in work function between the two materials.

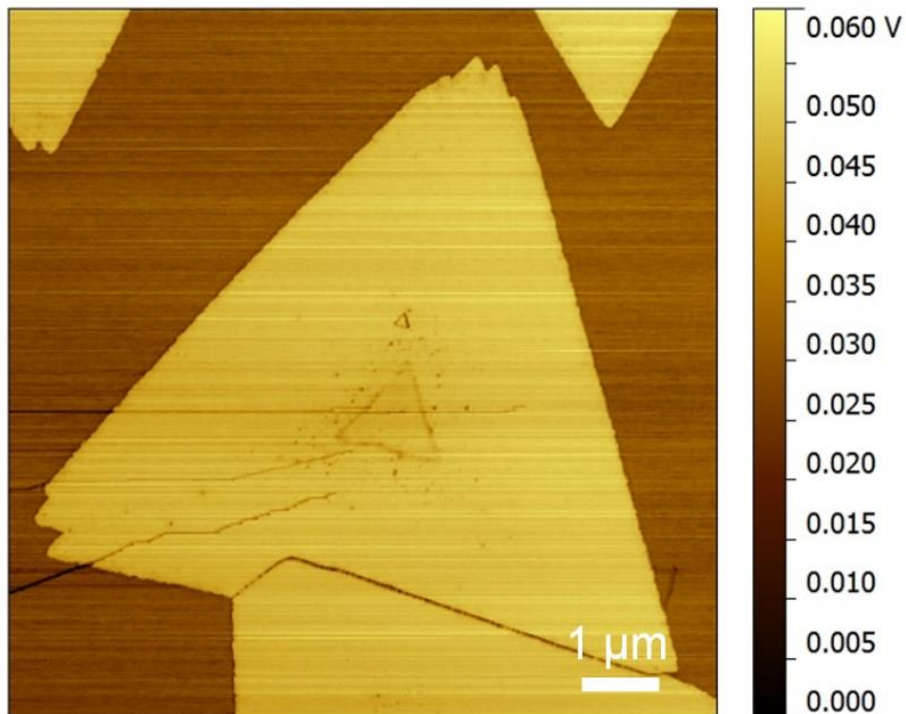


Figure 3.7. LFM friction image of the WS_2/MoS_2 heterostructure sample shown in Figure 3.5h. The height and friction images were acquired simultaneously. The boundary of the interior MoS_2 region is clearly visible. This figure is reproduced with permission from Yoo, et al. *J. Am. Chem. Soc.* **2015**, *137* (45), 14281–14287.⁸⁴

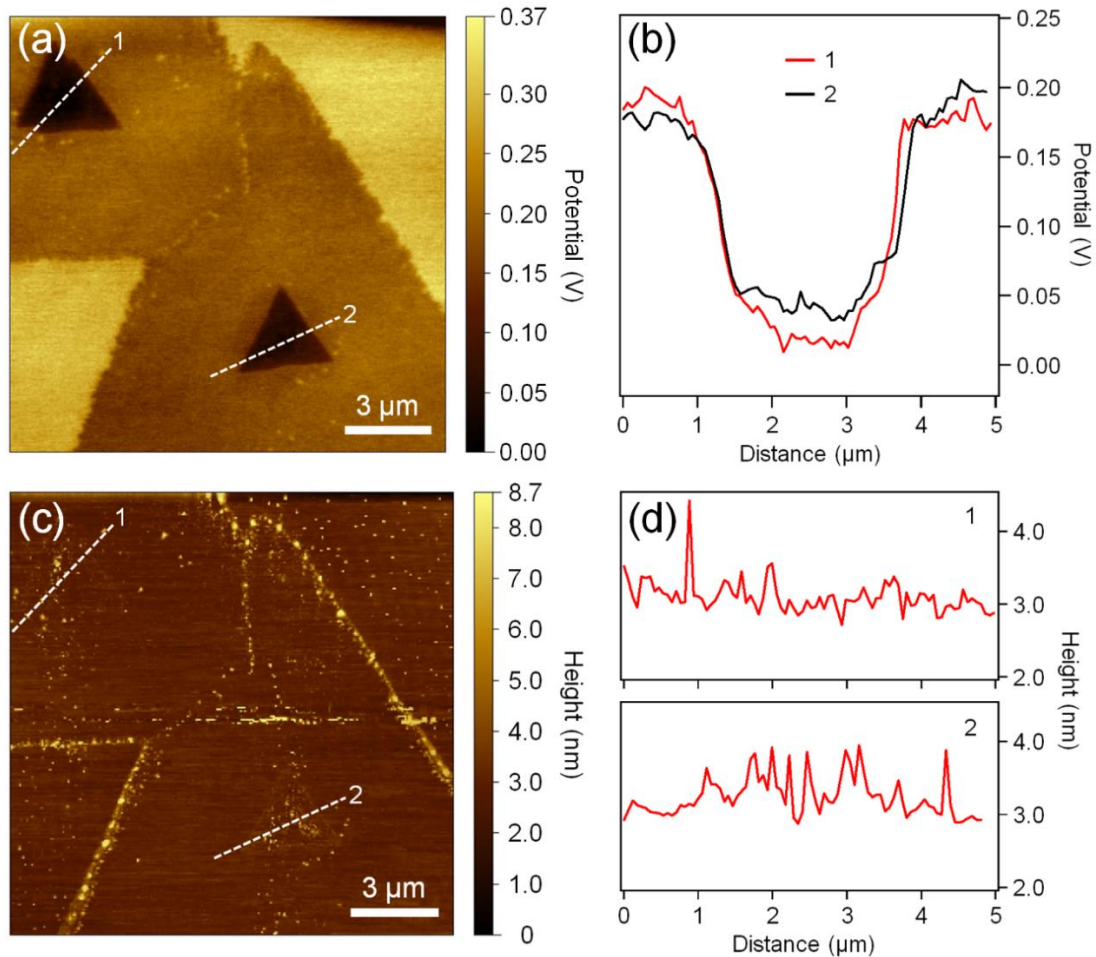


Figure 3.8. KPFM analysis of in-plane heteroepitaxial WS₂/MoS₂ monolayers. (a) KPFM surface potential image of in-plane heteroepitaxial WS₂/MoS₂ monolayers. The distinct contrast between the inner triangles of MoS₂ and the outer ribbons of WS₂ indicates that clear surface potential differences exist across the lateral junction, confirming that the as-synthesized heterostructures have high-quality lateral junctions. (b) Surface potential line profiles along the dotted white lines in (a). (c) Height image of the same flakes shown in (a), which was acquired simultaneously. (d) Height line profiles along the dotted white lines in (a). This figure is reproduced with permission from Yoo, et al. *J. Am. Chem. Soc.* **2015**, *137* (45), 14281–14287.⁸⁴

Scanning transmission electron microscopy (STEM) was used to better characterize the interface between the two materials, MoS₂ and WS₂, and to demonstrate heteroepitaxy. High-angle annular dark field (HAADF) microscopy can provide contrast in STEM images

of these heterostructures based on the scattering cross-sections for Mo and W atoms (also called Z contrast).¹⁰² Low-magnification HAADF-STEM images of in-plane heteroepitaxial monolayers show that the junction between the outer ribbon of WS_2 and the inner triangle of MoS_2 is visible but with relatively low contrast. The magnified image of the dotted orange square in Figure 3.9a shows a clear contrast difference between MoS_2 and WS_2 (Figure 3.9b). The image intensity at a given point in these HAADF-STEM images is determined by the spatial average atomic number and the thickness of the sample. Because the atomic number of WS_2 is larger than that of MoS_2 , the WS_2 appears brighter (higher image intensity) than the MoS_2 in dark-field imaging. Atomic-resolution HAADF-STEM imaging (Figure 3.9c) with associated fast Fourier transform (FFT) pattern of the junction region (inset) of the lateral heterostructure shows the atomically sharp junction between WS_2 and MoS_2 along a zig-zag direction. Even though the WS_2 growth occurs at a high temperature (higher than that of the MoS_2 growth), only minor annealing and elemental mixing is observed across the interface between WS_2 and MoS_2 . Of the elemental mixing that occurs, a larger concentration of W is substituted into the MoS_2 lattice than that of Mo substituted into the WS_2 lattice. This will be discussed in more detail later in this chapter.

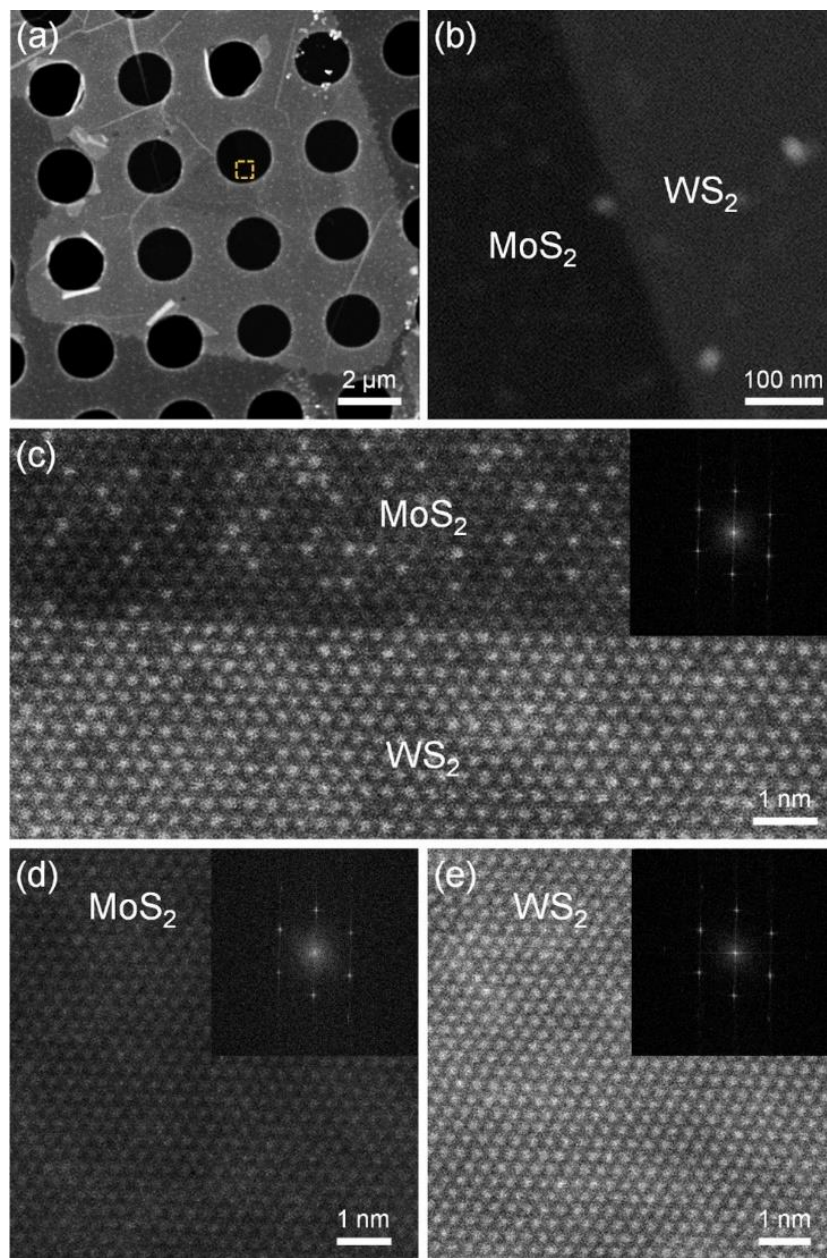


Figure 3.9. Z-Contrast HAADF-STEM images of the in-plane heteroepitaxial WS_2/MoS_2 monolayer. (a) Low-magnification HAADF-STEM image of the in-plane heteroepitaxial monolayer. (b) Magnified image of the dotted orange square in (a). (c) Atomic resolution HAADF-STEM image and its corresponding FFT pattern (inset) of the junction region of the in-plane heteroepitaxial monolayer. (d,e) Atomic-resolution HAADF-STEM images and corresponding FFT patterns (inset) of the MoS_2 region and the WS_2 region, respectively, of the in-plane heteroepitaxial monolayer. This figure is reproduced with permission from Yoo, et al. *J. Am. Chem. Soc.* **2015**, *137* (45), 14281–14287.⁸⁴

The FFT patterns of the MoS₂/WS₂ heterostructure show only one set of hexagonal spots, demonstrating that the WS₂ grows outward from the MoS₂ edges with lattice coherence, likely due to the relatively small lattice mismatch between WS₂ and MoS₂ (0.22%). Atomic-resolution HAADF-STEM images and corresponding FFT patterns of MoS₂ and WS₂ regions show clear hexagonal lattices without any substituted atoms. The orientation of the FFT patterns of the WS₂ region is the same as that of the MoS₂ region, further confirming the lattice coherence across the WS₂/MoS₂ boundary.

When WS₂ is grown using the particle-decorated MoS₂ monolayers as 2D seed crystals, vertically stacked WS₂/MoS₂ heterostructures are created. SEM imaging of these vertical heterostructures also shows a ribbon of WS₂ around the edge of the heterostructure region (Figure 3.10 and 3.11). These structures are confirmed to be vertically stacked by PL and Raman spectroscopy and AFM imaging. PL and Raman spectra taken from the center and edge of the vertical heterostructures show PL and Raman peaks from both WS₂ and MoS₂. The vertical heterostructures show relatively weak PL signal because the PL is quenched by charge transfer between the WS₂ and MoS₂ layers.^{72,103} The small triangular flakes visible in close proximity to the vertical heterostructures are identified as WS₂ monolayers by PL and Raman spectroscopy. These triangular particles exhibit a strong WS₂ PL signal due to the direct band gap of monolayer WS₂, and the Raman spectrum shows only WS₂ peaks (no evidence of MoS₂). AFM height images and line profiles show that the vertical WS₂/MoS₂ heterostructures have a thickness of about 1.4 nm and the monolayer WS₂ ribbons and triangular domains have a thickness of about 0.7 nm.

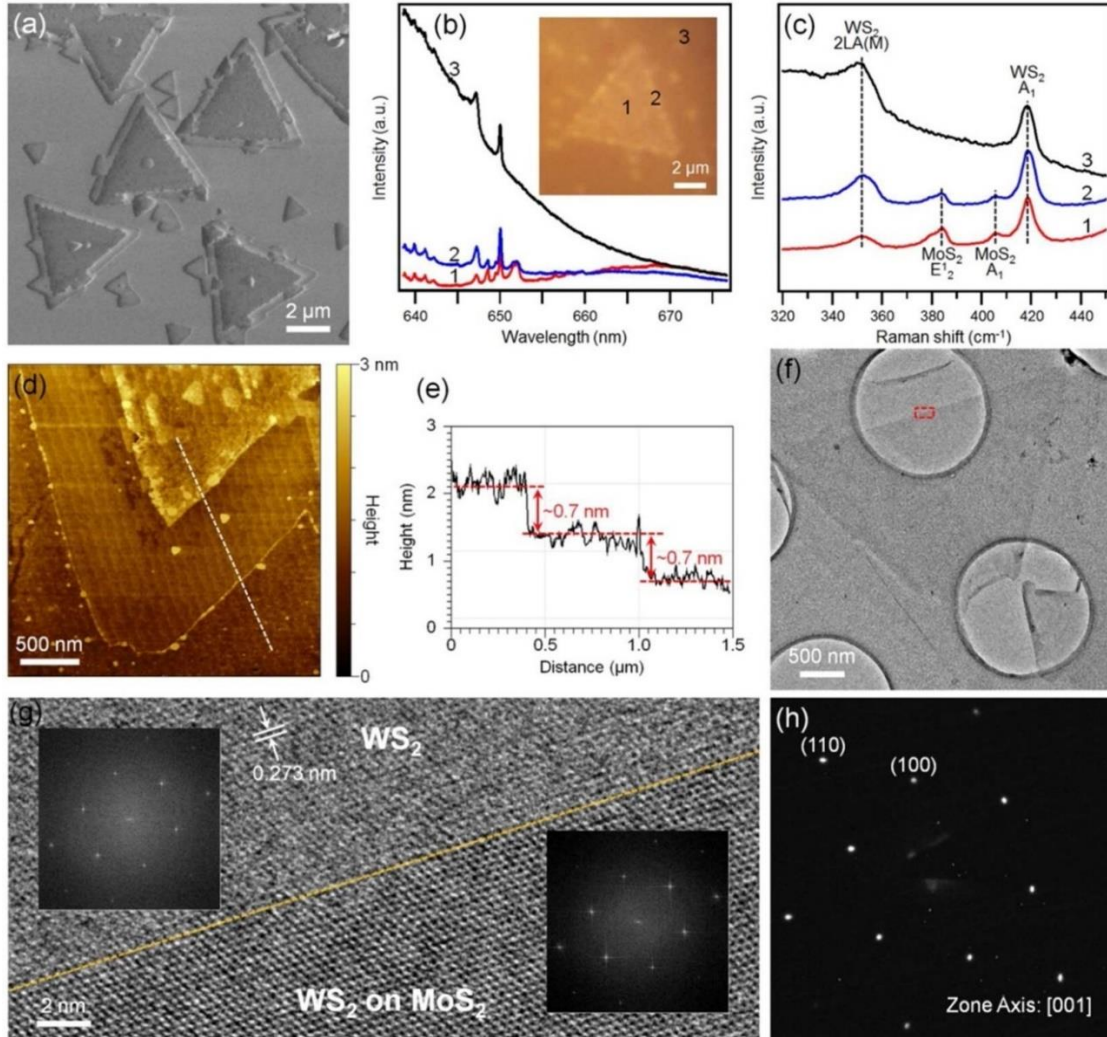


Figure 3.10. Vertical WS_2/MoS_2 heterostructures synthesized from monolayer MoS_2 grown without hydrogen. (a) SEM image of the vertical heterostructures. (b) PL and (c) Raman spectra acquired at points marked 1–3 in the inset in (b). The inset in (b) is an optical microscope image of a vertical heterostructure. (d) AFM height image of a vertical heterostructure. (e) Height line profile along the dotted white line in (d). (f) Bright-field TEM image of the vertical heterostructure. (g) HRTEM image of the dotted red square in (f) with corresponding FFT patterns of the WS_2 region and the WS_2/MoS_2 region, respectively. (h) SAED pattern of the vertical heterostructure. This figure is reproduced with permission from Yoo, et al. *J. Am. Chem. Soc.* **2015**, *137* (45), 14281–14287.⁸⁴

TEM imaging was used to better characterize the detailed crystal structure of the vertical heterostructures. Bright-field TEM images show the contrast between an interior triangle of the vertical WS_2/MoS_2 heterostructure and an exterior monolayer WS_2 ribbon. The contrast in the HAADF-STEM images of the vertical heterostructures is inverse to the contrast of the HAADF-STEM images of the lateral heterostructures (Figure 3.11). High-resolution TEM (HRTEM) images of the junction region between the WS_2 ribbon and WS_2/MoS_2 vertical heterostructure show the hexagonal lattices of both areas. In the WS_2 region, the lattice spacing of the planes perpendicular to the junction is 0.271 nm, consistent with the spacing of the (100) planes of WS_2 . The FFT patterns of the WS_2 region are in the same orientation as that of the WS_2/MoS_2 region, confirming that the monolayer WS_2 ribbon grows epitaxially from the edge of the vertical WS_2/MoS_2 heterostructure (see insets in Figure 3.9c,d). Selected area electron diffraction (SAED) patterns of the vertical WS_2/MoS_2 heterostructure show only a single set of hexagonal diffraction spots, thereby confirming that the WS_2 grows on top of the MoS_2 crystal with crystallographic alignment (vertical van der Waals heteroepitaxy).

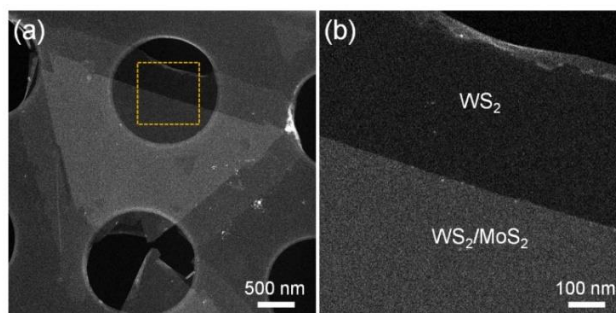


Figure 3.11. (a) HAADF-STEM image of vertical WS_2/MoS_2 heterostructures. (b) Magnified image of the orange dotted square in (a). This figure is reproduced with permission from Yoo, et al. *J. Am. Chem. Soc.* **2015**, *137* (45), 14281–14287.⁸⁴

The in-plane growth of WS₂ ribbons around the monolayer MoS₂ is thought to be kinetically controlled, because vertical heterostructures are known to be more thermodynamically stable than in-plane heterostructures.⁷⁶ The mechanisms for the growth of MoS₂ and WS₂ monolayers from their respective oxide precursors are effectively the same and well accepted in the literature. Thermal reduction of the transition metal trioxide precursor results in a volatile suboxide cluster, which can then adsorb onto, diffuse along, and desorb from the substrate.^{104–106} This occurs until the suboxide cluster encounters a nucleation site, where it will subsequently sulfurize to form MoS₂ or WS₂. The suboxide clusters can be supplied to the MoS₂ seed flakes by direct impingement from the vapor or by surface diffusion from the substrate. It has been previously reported that surface diffusion can be the major factor under high flux conditions, whereas direct impingement can be the major factor under low flux conditions.¹⁰⁷ For lateral growth of WS₂ ribbons around monolayer MoS₂, suboxide clusters supplied by surface diffusion are the largest contribution to the growth, because the anisotropic flow of material can induce the anisotropic material growth.¹⁰⁸ Thus, all WS₂ growths described above were performed under high-flux conditions. In contrast, vertical WS₂/MoS₂ heterostructures possess no WS₂ ribbons under low flux conditions (Figure 3.12). Under kinetically controlled reaction conditions like those shown here, monolayer WS₂ grows laterally from the edges of monolayer MoS₂, because these edge sites are the only sites active for nucleation when ultraclean MoS₂ monolayers are used as seeds.¹⁰⁹ When particle-decorated MoS₂ monolayers are used as seeds, particles on the MoS₂ surface can serve as additional nucleation sites, which leads to the formation of WS₂/MoS₂ vertical heterostructures with a ribbon of monolayer WS₂.

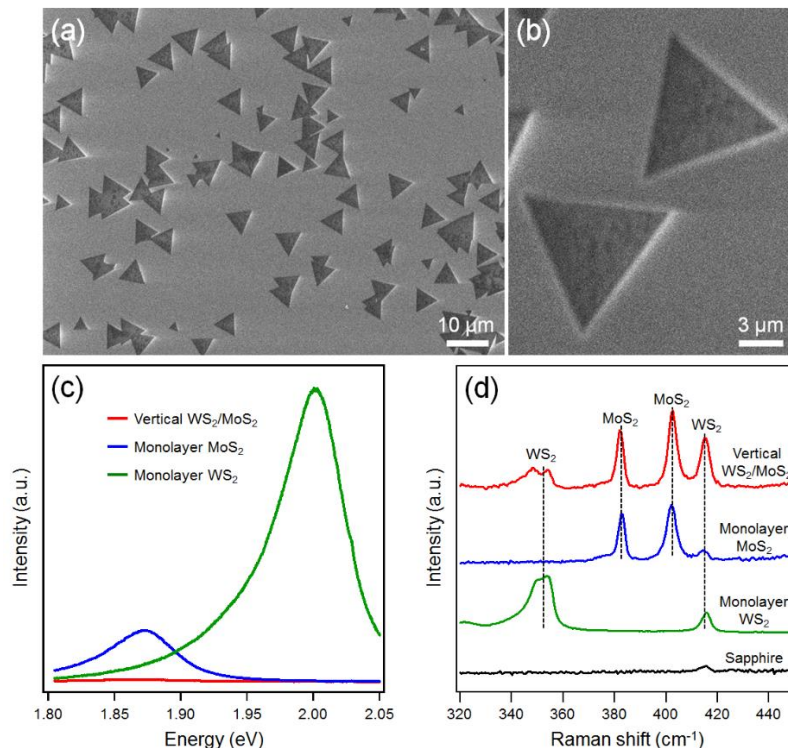


Figure 3.12. SEM, PL, and Raman analysis of vertical WS_2/MoS_2 heterostructures from low-flux conditions with no WS_2 ribbons. (a,b) SEM images of vertical WS_2/MoS_2 heterostructures possessing no WS_2 ribbons synthesized from monolayer MoS_2 grown without hydrogen under low flux conditions. The temperatures of WO_3 powder and MoS_2 seed crystals were about $960\text{ }^\circ\text{C}$ and $940\text{ }^\circ\text{C}$, respectively. (c) PL spectra of the vertical heterostructure (red curve), monolayer MoS_2 (blue curve), and monolayer WS_2 (green curve). (d) Raman spectra of the vertical heterostructure (red curve), monolayer MoS_2 (blue curve), monolayer WS_2 (green curve), and the sapphire substrate (black curve). This figure is reproduced with permission from Yoo, et al. *J. Am. Chem. Soc.* **2015**, *137* (45), 14281–14287.⁸⁴

The cleanliness of the MoS_2 seed flakes dictates the ability to control the competitive growth between lateral and vertical heterostructures. The small particles on the surface and edges of the MoS_2 synthesized without H_2 (Figure 3.2a) should largely be MoS_2 formed by sulfurization of small molybdenum suboxide clusters, which are continually supplied to the substrate during the reaction. Most of the suboxide clusters

contribute to the growth of monolayers or desorb from the substrate due to the high substrate temperature, but some of the suboxide clusters will aggregate and form stable molybdenum oxide particles. During this process, the edge regions of the monolayer MoS₂ can serve as preferential nucleation sites, because the edge regions have previously been shown to be sulfur-deficient when no H₂ is used.¹¹⁰ These molybdenum oxide particles will subsequently react with sulfur vapor to form small particles of MoS₂. The stability of the molybdenum suboxide particles is lowered in the presence of a highly reducing gas, such as H₂. The reduction of suboxide particles by H₂ will thereby revolatilize the precursors, leaving the basal plane of the MoS₂ flake clean of debris. Furthermore, we believe that monolayer MoS₂ synthesized with H₂ has highly homogeneous edges without sulfur deficiencies, because H₂ has been previously shown to drastically improve the quality of monolayer TMDC edges.^{111,112}

The TEM images displayed in Figure 3.9 and Figure 3.13 show atomic resolution of the individual transition metals in each material. This resolution allows for the extraction of important details regarding the local diffusion and atomic mixing across the MoS₂/WS₂ interface. It can be qualitatively seen in a HRTEM image of the interface, such as Figure 3.13a, that more W dopant atoms are visible in the MoS₂ lattice than Mo atoms in the WS₂ lattice. However, the quantitative nature of this elemental mixing and dopant diffusion could provide a better picture of the growth process during the WS₂ growth step. To assess the quantitative diffusion of W and Mo atoms across the MoS₂/WS₂ lateral heterostructure interface, I wrote a MATLAB script (see Appendix A) to count and plot the W and Mo atomic concentration across the MoS₂/WS₂ interface. The results of this analysis on a representative HRTEM image can be seen in Figure 3.13b.

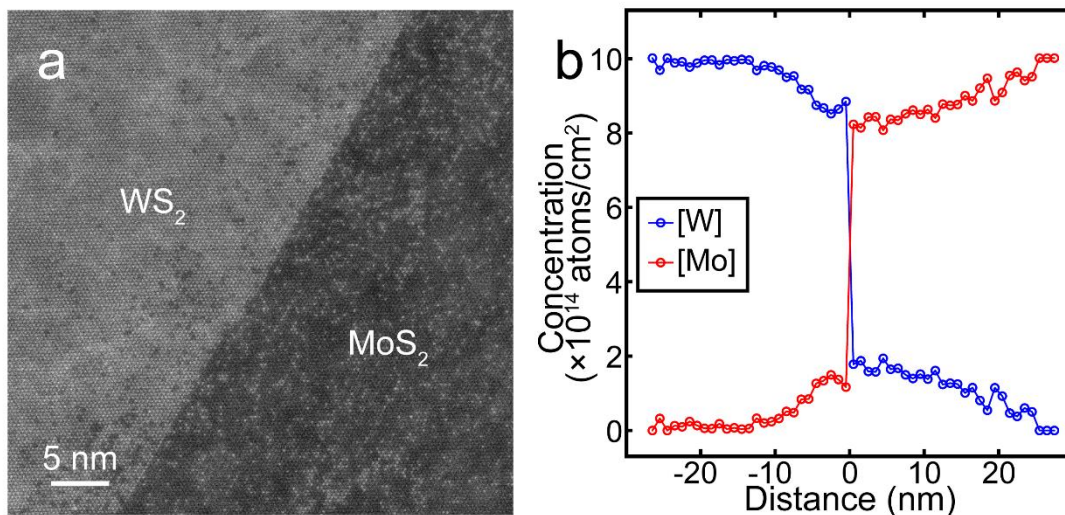


Figure 3.13. HRTEM of MoS₂/WS₂ lateral interface and diffusion quantification. (a) HRTEM image of MoS₂/WS₂ lateral heterostructure interface and (b) plot of the concentration of W and Mo atoms as a function of distance from the interface pictured in (a). In this plot, the blue circles and trace represent W and the red circles and trace represent Mo.

The W inclusions in the MoS₂ lattice are present more than 25 nm from the interface, whereas the Mo inclusions in the WS₂ lattice seem to be minimal beyond 10 nm from the interface. Furthermore, the concentration of W inclusions in the MoS₂ lattice remains greater than the concentration of Mo inclusions in the WS₂ lattice at any given respective position from the interface. This data suggests that W diffuses into the MoS₂ crystal to a significant degree during the WS₂ growth step, likely filling vacancies and defects that form in the MoS₂ as a result of the high-temperature, reducing WS₂ growth conditions. This data also suggests that some Mo diffuses away from the crystal edge and becomes incorporated into the WS₂ ribbon during the WS₂ growth step, but the concentration of Mo that is incorporated into the WS₂ ribbon is much lower than W that is incorporated into the MoS₂ crystal. These observations could be a result of relatively large

binding energies of MoS₂ units within the MoS₂ crystal, or a locally greater vapor-phase concentration of WO_{3-x} above the substrate surface during the WS₂ growth step, relative to any Mo-containing species.

3.5 Conclusion

In summary, by carefully controlling contamination and defects present in the 2D seed crystals, lateral and vertical heteroepitaxy between monolayer WS₂ and MoS₂ can be selectively achieved on *c*-cut sapphire substrates. Hydrogen gas plays an important role in removing small particles contaminating MoS₂ monolayer seeds. When H₂ is used as a carrier gas, ultraclean MoS₂ monolayers are synthesized, and can thereafter be used as seeds for lateral heteroepitaxial growth of monolayer WS₂ to form atomically coherent and sharp in-plane, lateral WS₂/MoS₂ heterostructures. When no hydrogen is used, particle-decorated MoS₂ monolayers are obtained, which serve as seeds for vertical heteroepitaxial growth of monolayer WS₂ and the formation of vertical WS₂/MoS₂ heterostructures.

This two-step synthesis serves as a building block for making abrupt junctions between 2D materials. By controlling the cleanliness of the 2D seed, we can limit the growth of additional 2D materials in subsequent growth steps to the edges of the 2D seed. This scheme can be utilized for many 2D heterostructures, including patterned junctions in 2D materials and as platforms for further explorations of the electronic and optical properties of these materials.

Chapter 4

MoO₂/MoS₂ Core/Shell Nanoplates

4.1 Preface

Controlling the growth of 2D TMDCs is an important step toward utilizing these materials for either electronics or catalysis. Here, we report a new surface-templated growth method that enables the fabrication of MoO₂/MoS₂ and MoO₂/MoTe₂ core/shell nanoplates epitaxially aligned on (0001)-oriented 4H-silicon carbide and sapphire substrates. These heterostructures are characterized by a variety of techniques to identify the chemical and structural nature of the interface. Scanning electron microscopy shows that the nanoplates feature 3-fold symmetry indicative of epitaxial growth. Raman spectroscopy indicates that the MoO₂/MoS₂ nanoplates are composed of co-localized MoO₂ and MoS₂, and transmission electron microscopy confirms that the nanoplates feature MoO₂ cores with 2D MoS₂ coatings. Locked-coupled X-ray diffraction shows that the interfacial planes of the MoO₂ nanoplate cores belong to the {010} and {001} families. This method may be further generalized to create novel nanostructured interfaces with single-crystal substrates.

4.2 Introduction

Mono- and few-layer TMDCs are two-dimensional (2D) materials that feature electronic properties rivaling those of conventional semiconductors and catalytic activity rivaling that of expensive noble metals.^{113–121,122–125} The synthesis of novel TMDC nanostructures could significantly increase their potential use in catalytic applications and may result in particles with new electronic properties.^{84,126–134} Most synthetic efforts to fabricate TMDCs tacitly assume weak chemical interactions between the TMDC and

substrate, based on the low surface energy and lack of dangling bonds of chemically saturated 2D layers. This differs from the growth of traditional semiconductor nanoparticles on surfaces, where strong particle–substrate interactions can determine morphology. Recently, Wang et al. reported a synthetic technique that yields MoO₂/MoS₂ core/shell nanoplates.⁹² This is effectively a two-step process, in which a metallic MoO₂ core plate is grown and then subsequently sulfurized.

We focus on the initial step of this process: the nucleation of the MoO₂ core onto the substrate. By selecting single-crystal substrates that are nearly lattice matched with the MoO₂ core, we can use surface interactions to drive the orientation of the resulting plates. The resulting structures are free-standing plates aligned with the substrate. The spontaneous alignment of these plates along high-symmetry axes of the substrate confirms the strong bond between the substrate and nanoparticle. Subsequent sulfurization yields MoS₂ shells that are also aligned with the substrate. This technique depends only on the chemistry between the seed MoO₂ and substrate, and we demonstrate that it can be extended to form other aligned TMDC platelets by synthesizing MoO₂/MoTe₂ platelets as well. We characterize these heterostructures with a variety of techniques and identify the chemical and structural nature of the interface. This work is reproduced with permission from DeGregorio, et al.¹³⁵

4.3 Experimental

Freestanding MoO₂/MoS₂ core/shell plates were grown on nitrogen-doped, n-type 4H-SiC(0001) substrates (Cree, Inc, doping density $5 \times 10^{18} \text{ cm}^{-3}$), *c*-cut sapphire substrates (MTI Corp.), and 90 nm SiO₂/Si substrates (ACS Materials Inc.) via chemical vapor

deposition using a single zone of a hot-wall three-zone tube furnace (Fischer/Blue M HTF55347) inside a 3-inch quartz tube (MTI Corp.). The substrate was placed face-up on an alumina boat downstream from solid MoO₃ (99.5%, Sigma Aldrich) and elemental sulfur (99.999%, Alfa Aesar) precursors. The MoO₃ precursor boat was placed immediately upstream from the substrate, while the S precursor was located farther upstream in a cooler region of the furnace ($T_{\text{sulfur}} \sim 350$ °C). The tube atmosphere was purged by evacuation followed by the introduction of ultra-high purity Ar (Airgas) until ambient pressure was restored. The furnace was then heated to 700 °C at a rate of 20 °C per minute under a constant flow of 20 sccm Ar. After holding at 700 °C for 5 minutes, the furnace was cooled rapidly to room temperature by opening the lid of the furnace.

A similar procedure was used for MoO₂/MoTe₂ core/shell plate growth on *c*-cut sapphire. In this case, tellurium pieces (99.999%, Sigma Aldrich) were used in lieu of sulfur precursor and the tellurium boat was placed directly upstream from the MoO₃ precursor boat. The reaction temperature for MoO₂/MoTe₂ core/shell plate growth was 650 °C. For MoO₂/MoS₂ core/shell plate growth, annealed SiC substrates were also used. Annealed SiC substrates were heated to temperatures between 700 °C and 1000 °C using identical purging procedures in a clean tube without any MoO₃ or S present. Annealed substrates were exposed to air between the annealing and CVD growth of nanoplates.

Samples were characterized by scanning electron microscopy (SEM) using a JEOL JSM-6500F microscope with an accelerating voltage of 5 kV. Electron backscatter diffraction (EBSD) was performed on the samples using an accelerating voltage of 20 kV and a beam current of ~20 nA, and the scattered electrons were detected by an Oxford EBSD detector. Channel 5 software was used for acquisition and pole figure generation.

Raman spectroscopy was performed using a home-built Raman microscope at room temperature. The output of a 632.8 nm HeNe continuous wave laser (Thor Labs HNL210L) was expanded and directed into an Olympus MPLN100X objective with ~ 200 μW impinging on the sample. The scattered light was dispersed off of a 1200 g/mm grating inside 500 mm spectrograph and imaged onto a charge-coupled device (CCD) camera (Pixis 100BR-X). Imaging was achieved by rastering the sample using a computer-controlled Mad City Labs MCLS02845 nanopositioning stage controlled by a computer running LabView 2014. Transmission electron microscopy (TEM) was performed using a Tecnai T12 microscope operated at an accelerating voltage of 120 kV. Samples were prepared for TEM characterization by transferring MoO₂/MoS₂ core/shell nanoplates onto Cu grids with Quantifoil carbon supports using a solution dispersion method. X-ray diffraction (XRD) is performed using a PANalytical X'Pert diffractometer with monochromated Cu K α source in a locked-coupled configuration. Low-energy electron diffraction (LEED) and Auger electron spectroscopy (AES) were performed using a 4-grid MCP-LEED system from Oxford Instruments. Samples were attached to a stainless steel sample holder and degassed at 250 °C inside an ultrahigh vacuum chamber (base pressure 1×10^{-10} torr) to remove atmospheric adsorbates. The MCP LEED system allowed for the use of nA of current to reduce sample degradation and surface charging on the insulating substrates. Auger experiments were performed at an electron beam energy of 1500 eV and a beam current of ~ 20 μA .

In this work, I performed all of the MoO₂/MoS₂ core/shell plate synthesis, experimental design, and characterization via Raman, XRD, LEED, AES, and plate orientation analysis in SEM. Youngdong Yoo performed the synthesis of MoO₂/MoTe₂

core/shell plates, performed characterization via TEM and SEM, and assisted with the realization of the experiments.

4.4 Results and Discussion

This report stems from recent research characterizing the nucleating event for growing monolayer and few-layer TMDCs. The synthetic approach for CVD growth of monolayer TMDCs is shown schematically in Figure 4.1a. The accepted mechanism for the growth of monolayer TMDCs involves the formation of small transition metal suboxide particles (such as MoO_{3-x}) that nucleate on the substrate surface (the first frame of the schematic in Figure 4.1a).¹³⁶ Subsequent sulfurization of these particles results in fullerene-like TMDC shells followed by the growth of monolayer TMDC flakes. By altering the temporal flux profile of the chalcogen species, we obtain vertical, freestanding plates rather than flakes on SiC(0001). This procedure works for both MoTe_2 as well as MoS_2 , implying that nucleation of the MoO_2 core rather than chalcogenization is the morphology-determining step. Here, we will focus on the synthesis of the MoS_2 -based plates.

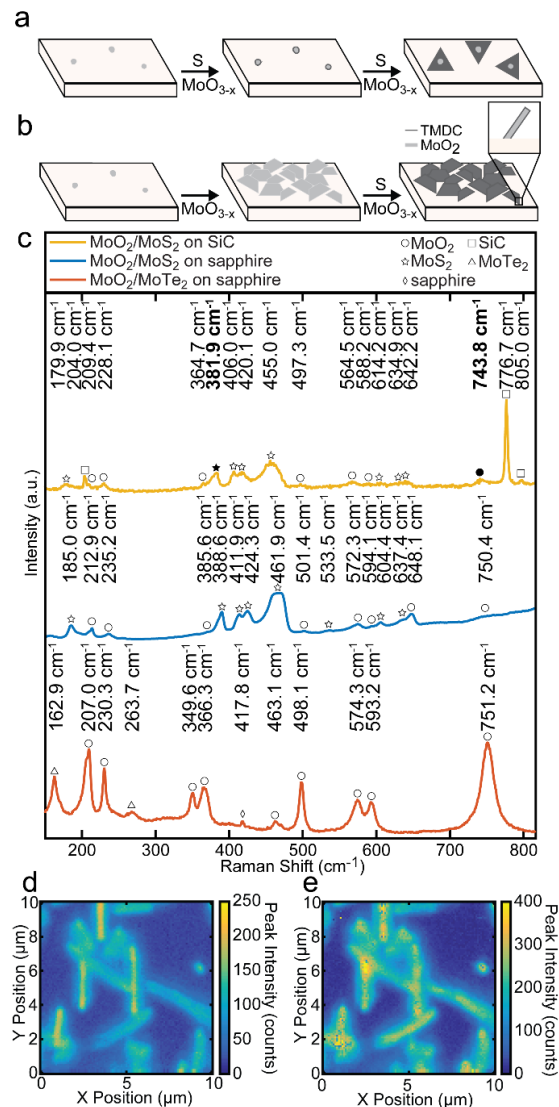


Figure 4.1. Mechanism schematics and Raman spectroscopy of MoO₂/MoS₂ core/shell plates. Schematics illustrating the self-seeding mechanisms of (a) monolayer TMDCs (previously reported) and (b) core/shell nano-plates (reported here). (c) Raman spectra (excited at 632.8 nm) of MoO₂/MoS₂ core/shell plates on SiC, MoO₂/MoS₂ core/shell plates on sapphire, and MoO₂/MoTe₂ core/shell plates on sapphire with identities indicated with a symbol above each peak (square for SiC, diamond for sapphire, circle for MoO₂, star for MoS₂ and triangle for MoTe₂). For MoO₂/MoS₂ core/shell plates on SiC, 2D maps are generated for the fitted Raman peak intensities of the (d) MoO₂ ~750 cm⁻¹ peak and (e) MoS₂ E₂ (~385 cm⁻¹) mode (no background subtraction). Fitted peak positions used in the 2D maps in (d) and (e) feature filled peak identity symbols and bolded peak positions in (c). This figure is reproduced with permission from DeGregorio, et al. *J. Phys. Chem. Lett.* **2017**, 8 (7), 1631–1636.¹³⁵

By moving the sulfur to colder/hotter regions of the furnace, we can reduce/increase its concentration within the CVD tube. Reducing the sulfur concentration in this manner additionally delays the arrival of the chalcogen species relative to the metal oxide precursor due to the position-dependent temperature ramp within the tube. The saturated sulfur vapor pressure at the source, which ultimately determines the concentration of sulfur at the sample during the growth process, is calculated in Figure 4.2. The low initial concentration of sulfur results in the condensation and crystallization of MoO_2 on the surface of the substrate, which is subsequently converted to MoS_2 as the sulfur concentration rises. The resulting structure is a core/shell plate of $\text{MoO}_2/\text{MoS}_2$, and the chemical interactions between the initial MoO_2 core and the substrate determine the shape and orientation of the particle, as shown in Figure 4.1b.

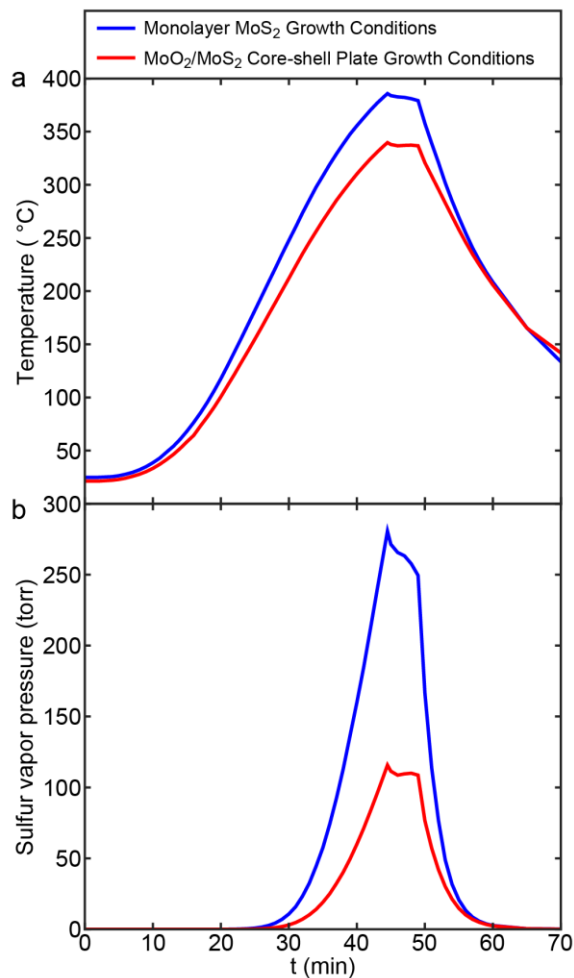


Figure 4.2. (a) Plots of temperature of sulfur boat position as a function of time and (b) plots of calculated sulfur vapor pressure as a function of time in the case of MoS₂ monolayer growth (blue) and MoO₂/MoS₂ core-shell plate growth (red). Vapor pressure was calculated using experimentally determined temperatures and using the relation in Ref. 137.¹³⁷ Between these two cases, the MoO₃ precursor boat position is unchanged, thus the MoO_{3-x} vapor pressure as a function of time is approximately the same in each case. This figure is reproduced with permission from DeGregorio, et al. *J. Phys. Chem. Lett.* **2017**, 8 (7), 1631–1636.¹³⁵

We confirm that the plates contain both crystalline MoO₂ and crystalline TMDC using Raman spectroscopy on representative plates. The Raman spectra of SiC(0001), MoO₂, MoS₂, and MoTe₂ have been extensively studied and are here used as chemical

identifiers.^{93,136,138–141} The Raman spectrum of a representative MoO₂/MoS₂ plate on SiC(0001) is shown in yellow in Figure 4.1c. All 19 of the peaks in the spectrum were assigned as known Raman peaks for either SiC,¹³⁸ MoO₂,¹³⁹ or MoS₂.⁹³ The Raman spectrum of bulk 2H-MoS₂ contains two primary peaks located at 381.9 cm⁻¹ (E_{2g}¹) and 406.0 cm⁻¹ (A_{1g}). Importantly, the energy separating these two phonon modes varies monotonically from 25 cm⁻¹ in the bulk to 18 cm⁻¹ in monolayer MoS₂. On the basis of the peak separation shown in Figure 4.1c, we estimate that the MoS₂ in the platelets is ~3–5 layers thick.⁹³ We note that interfacial strain will certainly induce shifts in the Raman spectra, and this has been extensively studied for MoS₂. Here, however, we are using the Raman spectrum as an analytical tool to identify the vibrational fingerprints of each component material. Raman mapping of the most intense MoS₂ and MoO₂ modes further confirms that the TMO and TMDC signals are coming from the same location (Figure 4.1d,e) and from regions of high optical contrast (Figure 4.3).

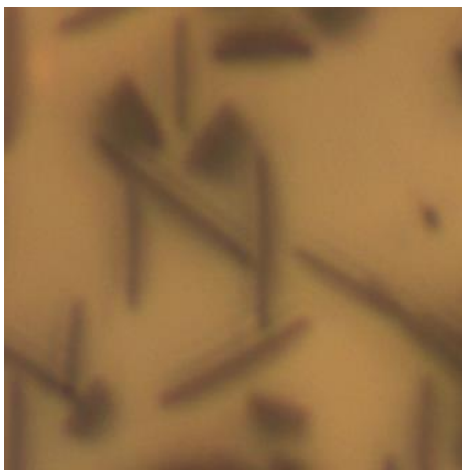


Figure 4.3. Optical image of MoO₂/MoS₂ core-shell plates visible in two-dimensional Raman maps in Figure 4.1d-e. Dark optical contrast corresponds well with increased intensity of Raman peaks for MoS₂ and MoO₂. Image width is 10 μm. This figure is reproduced with permission from DeGregorio, et al. *J. Phys. Chem. Lett.* **2017**, 8 (7), 1631–1636.¹³⁵

We used TEM to determine the core/shell structure of the MoO₂/MoS₂ plates. MoO₂/MoS₂ plates grown on SiC(0001) were carefully transferred from the SiC substrate onto a Quantifoil TEM grid using a solution dispersion method to place the plates flat on the TEM grid. Typical plates are shown in Figure 4.4a,b. The selected area electron diffraction (SAED) patterns acquired from these plates (Figure 4.4c,d) confirm that the monoclinic MoO₂ plate cores are single-crystalline and have a zone axis of [201]. Because the TEM images and SAED patterns were taken with nearly zero tilt angles, we deduce that the [201] zone axis is nearly perpendicular to the basal planes of the flat plates. Thus, the basal planes of both plates are identified as the {100} planes by simple crystallographic facet angle calculations. The dim spots scattered on the SAED patterns originate from MoS₂ shells. High-resolution TEM images of the plate edges (Figure 4.4e,f) show lattice fringes with spacing of ~6 Å, consistent with those of the MoS₂ formed on the side facets

of the plates. By counting the number of lattice fringes, we estimate that the MoS₂ shell is three layers thick, consistent with the estimate from Raman spectroscopy.

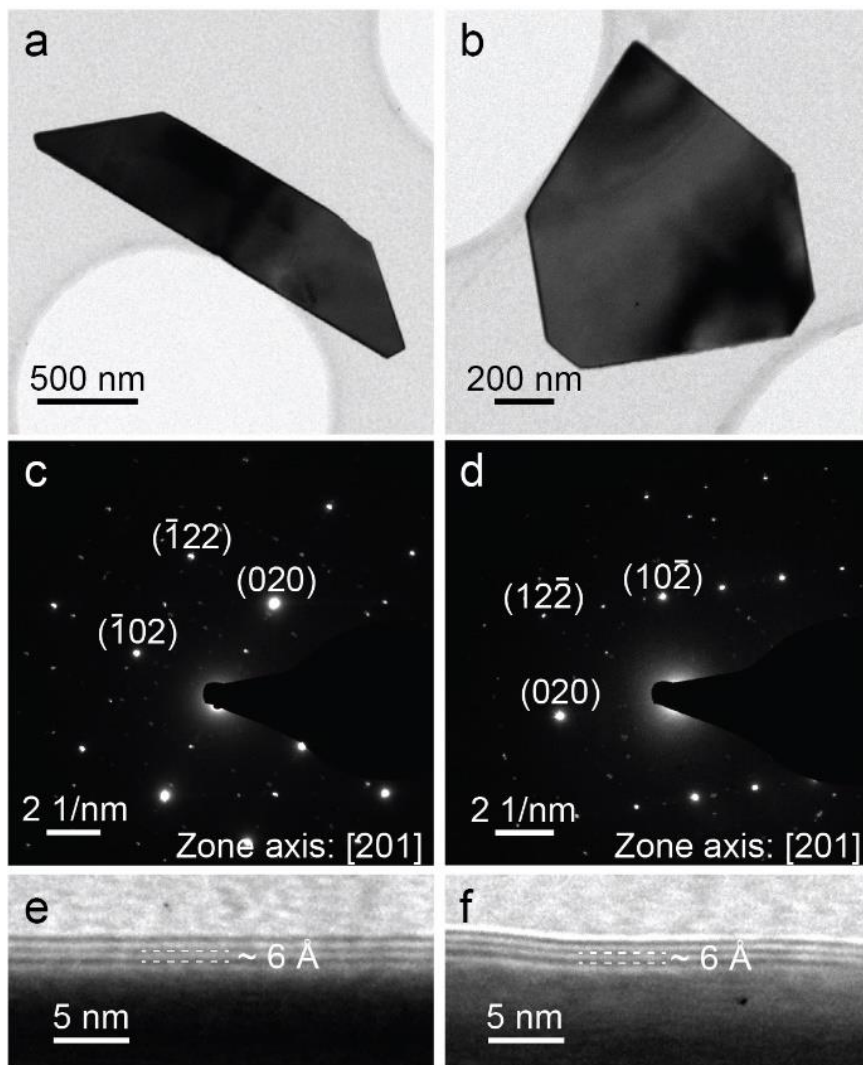


Figure 4.4. TEM analysis of MoO₂/MoS₂ core/shell plates. (a,b) TEM images of suspended vertical MoO₂/MoS₂ core/shell nanoplates. (c,d) SAED patterns corresponding to the plates in (a) and (b), respectively. (e,f) HRTEM images of plate edges in (a) and (b), respectively, showing lattice fringes indicative of MoS₂ few-layer shells. This figure is reproduced with permission from DeGregorio, et al. *J. Phys. Chem. Lett.* **2017**, 8 (7), 1631–1636.¹³⁵

Having confirmed the platelet core/shell structure, we seek to understand the growth mechanism driving vertical plate growth, as opposed to flat plate growth that has been reported previously.⁹² We hypothesize that the vertical structure is due to strong chemical interactions between the substrate and the MoO₂ core. First, the plates are aligned along the high-symmetry directions of the underlying wafer, as seen in SEM (Figure 4.5a–c). The plates display two different morphologies. They are either normal to the surface or tilted at an angle from the surface. Both families of plates (normal and tilted) have preferential growth directions, as highlighted by the red (normal plates) and blue (tilted plates) dotted lines in each image of Figure 4.5. Aside from the difference in tilt angle, these two morphologies have similar shapes and sizes, as shown by the tilted SEM images in Figure 4.5b. In these images, the sample stage was tilted inside of the microscope until the microscope was looking down the growth axis of the tilted plates (approximately 35°). In the tilted image, the previously tilted plates appear vertical, and the previously vertical plates appear tilted with a similar shape to that of the tilted plates in Figure 4.5a.

The platelets are aligned on the surface with 60° rotational symmetry, with a 30° offset between the two families. We measured the orientation of several hundred normal and tilted plates on the surface relative to the $[11\bar{2}0]$ direction of the silicon carbide. These results are shown in Figure 4.5d. Additionally, annealing the substrates prior to CVD leads to increased nucleation and alignment. At high temperatures, SiC(0001) undergoes a range of surface reconstructions that depend on temperature, pressure, and environmental composition.^{58,59,142–146} Figure 4.5c shows a SEM image of a SiC sample that was annealed at 1000 °C under Ar prior to growing the MoO₂/MoS₂ nanoplates, resulting in ~3× more

plates on the surface. This increase in nucleation indicates that substrate surface chemistry is playing an influential role in particle nucleation.

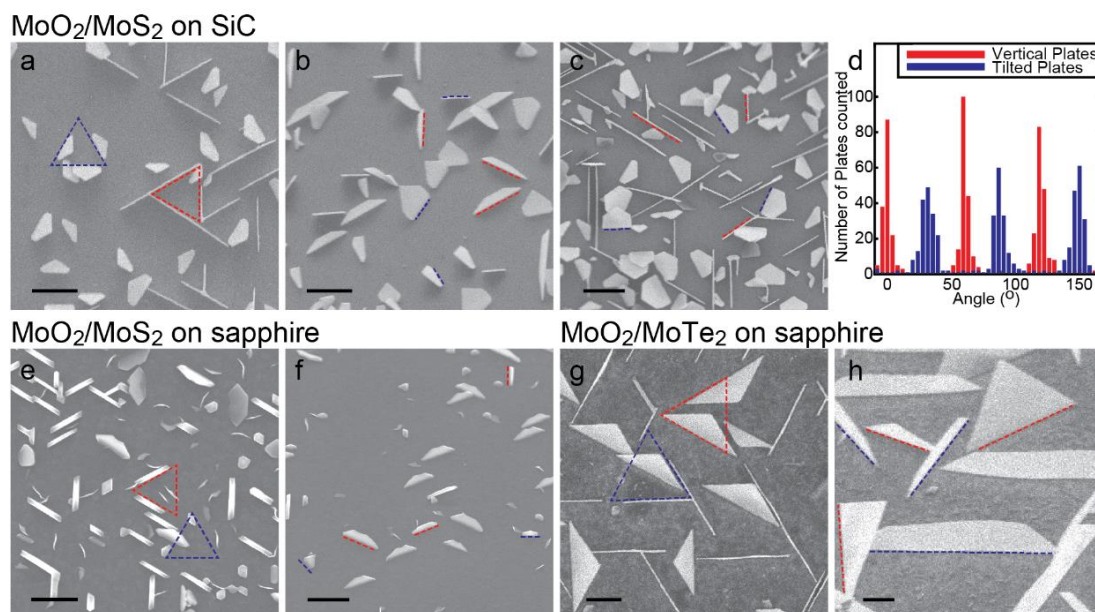


Figure 4.5. SEM analysis of MoO₂/MoS₂ core/shell plates. (a) SEM image of MoO₂/MoS₂ core/shell freestanding nanoplates on bare SiC with overlaid dotted triangles indicating three-fold symmetry of freestanding plates (red for vertically aligned plates and blue for tilted plates). (b) SEM image of the substrate in (a) with the stage tilted to 35°. (c) SEM image of growth on a SiC substrate previously annealed to 1000 °C. (d) histogram of MoO₂/MoS₂ core/shell nanoplates visible in a representative SEM image as a function of the azimuthal angle (relative to the SiC [11 $\bar{2}$ 0] direction). (e) SEM image of MoO₂/MoS₂ core/shell nanoplates grown on c-cut sapphire. (f) SEM image of the substrate in (e) tilted to 45°. (g) SEM image of MoO₂/MoTe₂ core/shell nanoplates on sapphire. (h) SEM image of the substrate in (g) tilted to 45°. All scale bars are 1 μm. This figure is reproduced with permission from DeGregorio, et al. *J. Phys. Chem. Lett.* **2017**, 8 (7), 1631–1636.¹³⁵

To understand how the substrate interactions could be directing growth of these core/shell plates, we consider the structure and reactivity of both the TMDC shell and the

TMO core. Conventional epitaxial growth of a material on a substrate induces a strain penalty that must be energetically compensated for by favorable chemical interactions. MoS₂ is a hexagonal layered material with a similar in-plane lattice constant to that of SiC(0001) ($a_{\text{SiC}} = 3.09 \text{ \AA}$, $a_{\text{MoS}_2} = 3.15 \text{ \AA}$).^{60,147} However, as a layered material, MoS₂ interacts weakly between layers and with a substrate surface. In order to exhibit epitaxy, the energy stored in the strained TMDC would need to be compensated by the interaction with the substrate. Indeed, by changing our reaction conditions, we were able to grow monolayer flakes of MoS₂ on SiC(0001) (Figure 4.6).

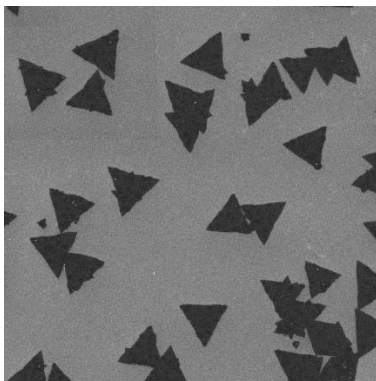


Figure 4.6. SEM image of MoS₂ monolayer flakes grown on a SiC substrate. Image width is 50 μm . This figure is reproduced with permission from DeGregorio, et al. *J. Phys. Chem. Lett.* **2017**, 8 (7), 1631–1636.¹³⁵

Despite needing only a 2.2% compression to be epitaxial on SiC(0001), these flakes of MoS₂ exhibit no preferred orientation. Additionally, growth of MoO₂/MoS₂ core/shell plates on SiO₂/Si substrates results in freestanding and flat plates with random orientations (Figure 4.7). Given this data, the interactions between SiC(0001) and the TMDC basal

plane and between MoO₂ cores and the amorphous SiO₂/Si substrate must be too weak to account for the oriented nanoplates that we observe.

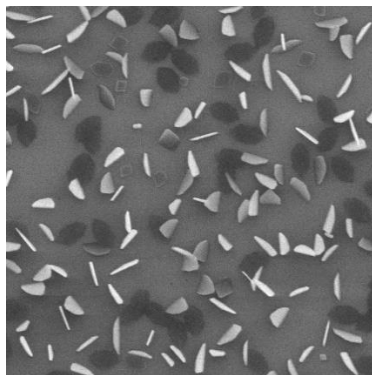


Figure 4.7. SEM image of MoO₂/MoS₂ core-shell plates grown on a SiO₂/Si substrate (90 nm oxide). No rotational symmetry or epitaxy is visible and plate faceting is different than on other substrates. Image width is 16 μm . This figure is reproduced with permission from DeGregorio, et al. *J. Phys. Chem. Lett.* **2017**, 8 (7), 1631–1636.¹³⁵

Next, we consider the structure of the MoO₂ oxide core and its relationship to SiC(0001). MoO₂ is a monoclinic crystal derived from a distorted rutile structure with a much larger lattice constant than SiC (space group P2₁/c, $a = 5.61 \text{ \AA}$, $b = 4.86 \text{ \AA}$, $c = 5.63 \text{ \AA}$, $\beta = 121^\circ$).¹⁴⁸ However, if one slices MoO₂ along its low-index planes, there would be unsaturated metal and oxygen atoms that could form strong covalent bonds to the oxide surface. Furthermore, while the lattice of MoO₂ is monoclinic, the angle between the a axis and the c axis is nearly 120° , suggesting that it could also adopt hexagonal symmetry on the surface.

Finally, we note that the SiC(0001) surface is known to reconstruct in a variety of ways, but at lower temperature, the most prominent reconstruction is the highly studied

SiC ($\sqrt{3} \times \sqrt{3}$)R30°. This surface reconstruction has a hexagonal lattice constant of 5.323 Å, only 5% different from the a and c axes of MoO₂. We used low-energy electron diffraction (LEED) and Auger electron spectroscopy to confirm the presence of the ($\sqrt{3} \times \sqrt{3}$)R30° reconstruction following nanoparticle growth and following sample annealing at 1000 °C (see Figures 4.8 and 4.9). We therefore hypothesize that oriented growth of the freestanding MoO₂ core is driven by the initial formation of a strained, epitaxial MoO₂ particle on the reconstructed surface, which is subsequently sulfurized to form the MoS₂ layers.

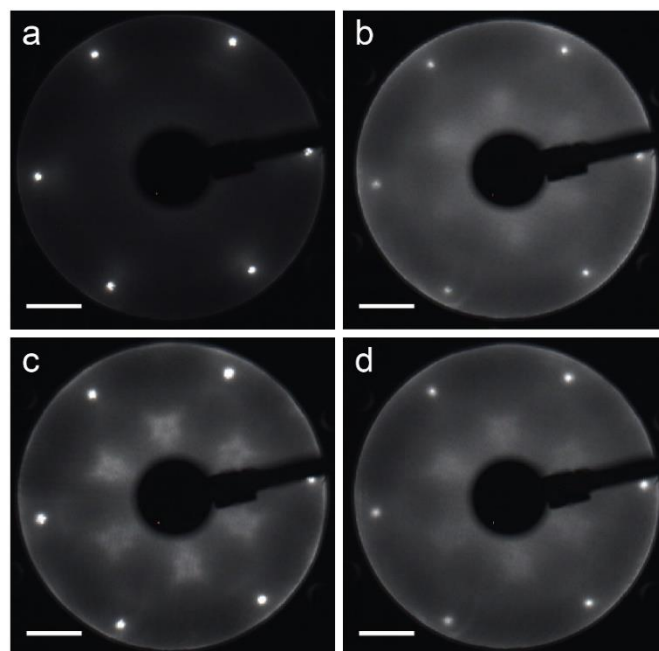


Figure 4.8. LEED patterns of prepared 4H-SiC and core/shell nanoplate samples. (a) Bare 4H-SiC, (b) MoO₂/MoS₂ core/shell nanoplates grown on SiC, (c) SiC substrate after 1000 °C anneal, and (d) MoO₂/MoS₂ core/shell nanoplates grown on SiC that had been previously annealed to 1000 °C (all images acquired with 100 eV beam energy, scale bars denote 1 Å⁻¹). This figure is reproduced with permission from DeGregorio, et al. *J. Phys. Chem. Lett.* **2017**, 8 (7), 1631–1636.¹³⁵

Polished SiC(0001) samples show the 6 spots belonging to the (1×1) unit cell (Figure 4.8a). The LEED patterns of samples after MoO₂/MoS₂ core/shell nanoplate growth on SiC (Figure 4.8b) show diffuse SiC ($\sqrt{3}\times\sqrt{3}$)R30° diffraction spots in addition to the primary SiC (1×1) spots.⁵⁸ After annealing the substrates to 1000 °C under argon, the pattern sharpens, takes on additional structure, and grows brighter (Figure 4.8c). This structure grows more diffuse, but persists, after growing MoO₂/MoS₂ platelets on the annealed substrates (Figure 4.8d). The increased structure indicates that additional reconstruction is happening, but it is difficult to resolve the exact symmetry and spacing.

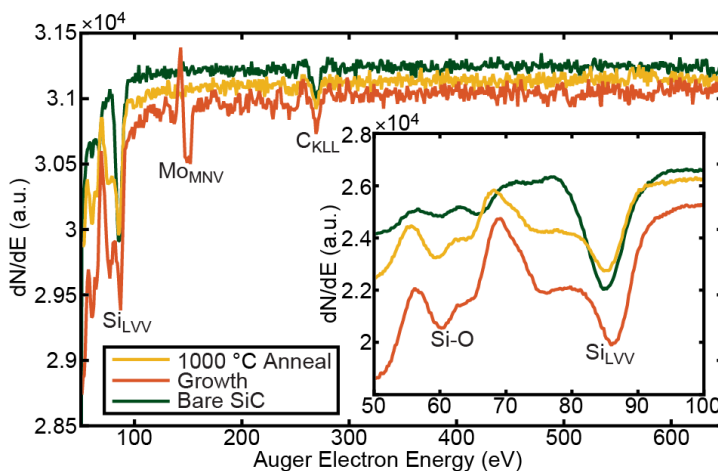


Figure 4.9. Low-energy Auger electron spectra with inset high-resolution spectra of MoO₂/MoS₂ core-shell plates grown on SiC (orange trace), bare SiC (green trace), and SiC after annealing at 1000 °C (yellow trace). Charging was observed on some spectra, so a linear offset was applied to align the C_{KLL} peaks. The ratios of Si_{LVV} to C_{KLL} peak amplitudes for core-shell plates grown on SiC (orange trace), bare SiC (green trace), and SiC after annealing at 1000 °C (yellow trace) are 5.54, 5.47, and 5.59, respectively, supporting the growth of the carbon-deficient ($\sqrt{3}\times\sqrt{3}$)R30° surface reconstruction. The signal-to-noise of peaks for the Si_{LVV} peaks in each of these cases is 38, 33, and 27, respectively, while the signal-to-noise of peaks for the C_{KLL} peaks is 5, 7, and 7, respectively. This figure is reproduced with permission from DeGregorio, et al. *J. Phys. Chem. Lett.* **2017**, 8 (7), 1631–1636.¹³⁵

Auger spectroscopy (Figure 4.9) confirms that all samples show the presence of Si_{LVV} and C_{KLL} peaks. The Auger spectra of substrates after growth and after annealing show additional peaks in the range of 60–85 eV, consistent with silicon-oxygen bonds.¹⁴² The ratio of Si_{LVV} to C_{KLL} peak amplitudes (measured trough to baseline) after background subtraction increases for the sample after growth and after annealing relative to bare SiC, consistent with the growth of the carbon-deficient $(\sqrt{3}\times\sqrt{3})\text{R}30^\circ$ surface reconstruction.

To probe the epitaxial relationship between the MoO_2 cores and the SiC substrate, we used locked-coupled XRD to determine which planes are parallel to the SiC(0001) surface and we performed electron backscatter diffraction (EBSD) on 63 individual plates. Representative results of this analysis can be seen in Figure 4.10. Pole figures generated using representative EBSD data (Figure 4.10c–d) show spots in similar positions near the center for the SiC (0001) pole figure and the MoO_2 (010) and (001) pole figures for a variety of representative plates, which indicates that these crystallographic planes are aligned. The alignment of the SiC (0001), MoO_2 (010), and MoO_2 (001) planes as measured by EBSD supports that these are the interfacial planes responsible for epitaxial growth of the core/shell plates. However, due to the sample geometry, it is unclear whether EBSD diffraction patterns acquired from specific plates are detected via traditional Bragg diffraction or a transmission Kikuchi diffraction. This uncertainty makes definitive orientation analysis from EBSD data alone impossible.

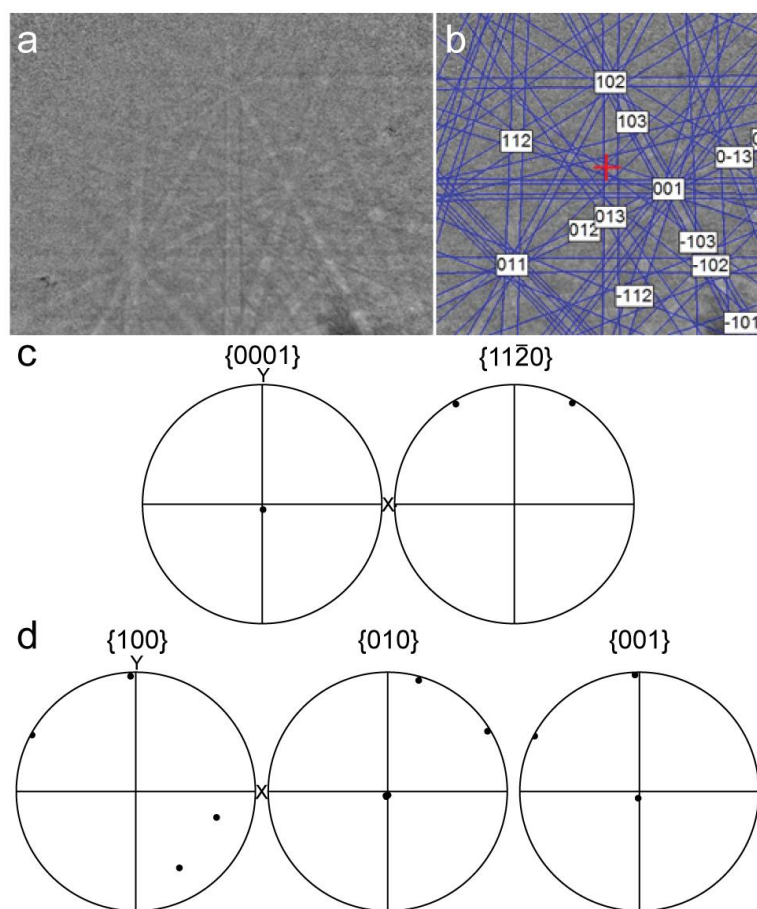


Figure 4.10. Representative EBSD analysis of core/shell nanoplates. (a) Raw and (b) indexed EBSD patterns for a $\text{MoO}_2/\text{MoS}_2$ plate. EBSD pole figures of $\text{MoO}_2/\text{MoS}_2$ core/shell plates generated on (c) one region of exposed SiC substrate and (d) seven representative $\text{MoO}_2/\text{MoS}_2$ core/shell plates. This figure is reproduced with permission from DeGregorio, et al. *J. Phys. Chem. Lett.* **2017**, 8 (7), 1631–1636.¹³⁵

The XRD pattern of the $\text{MoO}_2/\text{MoS}_2$ core/shell plate sample (Figure 4.11a) shows four 4H-SiC $\{0001\}$ peaks corresponding to the single-crystal 4H-SiC(0001) substrate used in the growth. Two MoO_2 peaks corresponding to the (020) and (002) planes are also visible. The locked-coupled $\theta/2\theta$ methodology only probes crystal planes with the \hat{q} vector normal to the surface. The presence of peaks corresponding to MoO_2 (010) and (001) planes confirms that these planes feature interfacial binding with the reconstructed

substrate surface. These interfacial plane assignments are supported by EBSD (Figure 4.10). Schematics of vertical (Figure 4.11b) and tilted (Figure 4.11c) plates indicate low-energy surface planes responsible for plate morphology. Given the crystal structure of the MoO₂ cores, the SAED patterns in Figure 4.4 indicate that all plates have basal planes of (100). The edge plane identities schematically represented in Figure 4.11b,c were determined by simple crystallographic facet angle calculations. These edge plane identities are supported by the interfacial planes identified from XRD, EBSD, and calculation of the plate facet angles using SEM images of flattened plates (Figure 4.12). Top-view, two-dimensional schematic illustrations of the MoO₂ (010) and (001) planes with underlying 4H-SiC ($\sqrt{3}\times\sqrt{3}$)R30° surface reconstruction can be seen in Figure 4.13.

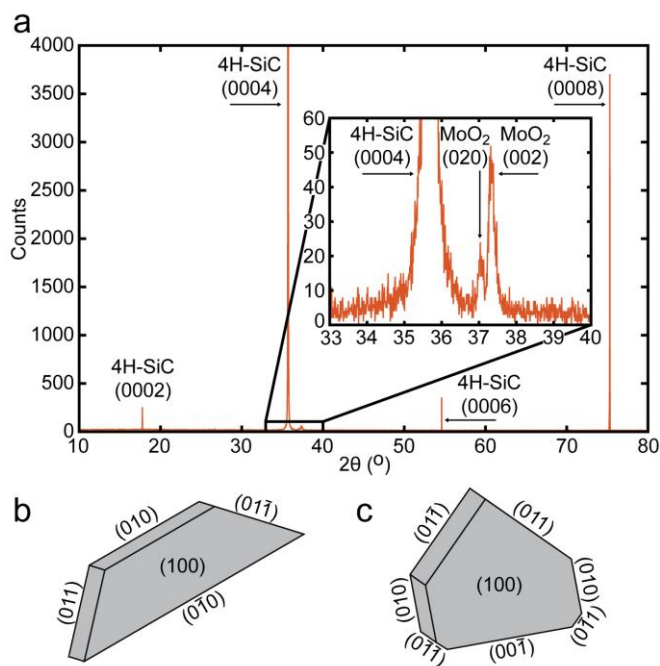


Figure 4.11. Structural analysis of MoO₂/MoS₂ core/shell plates. (a) XRD pattern of MoO₂/MoS₂ freestanding core/shell nanoplates on SiC acquired using a locked-coupled methodology. Schematics illustrating the MoO₂ crystallographic planes associated with the facets of (b) normal plates and (c) tilted plates. This figure is reproduced with permission from DeGregorio, et al. *J. Phys. Chem. Lett.* **2017**, 8 (7), 1631–1636.¹³⁵

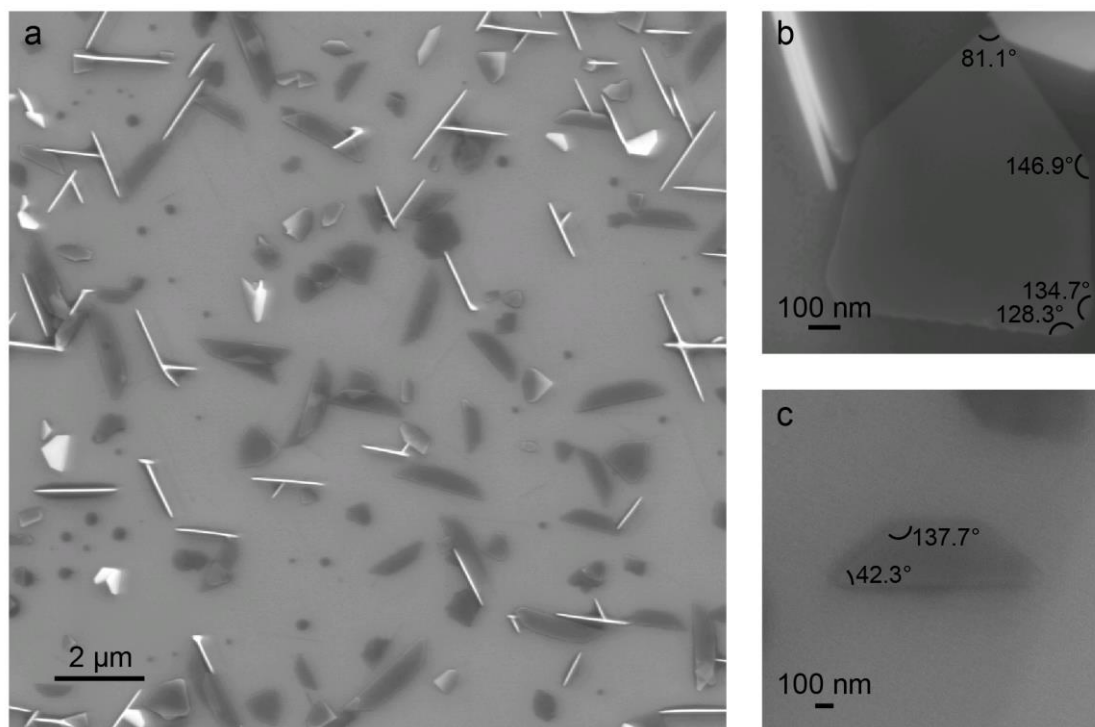


Figure 4.12. SEM images of MoO₂/MoS₂ core-shell plates that have been pushed flat using another bare SiC substrate. Higher-magnification SEM images of (b) tilted plates and (c) vertical plates are labeled with average plate facet angle measurements. This figure is reproduced with permission from DeGregorio, et al. *J. Phys. Chem. Lett.* **2017**, 8 (7), 1631–1636.¹³⁵

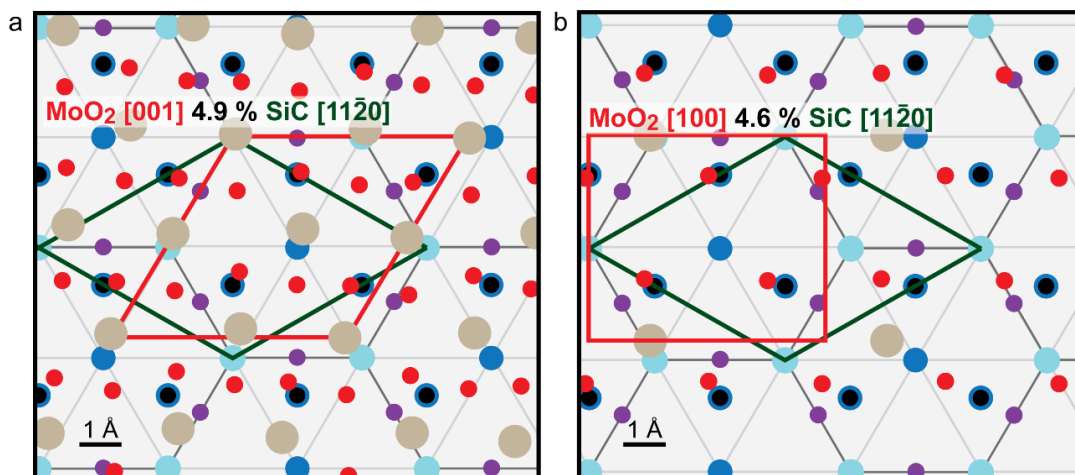


Figure 4.13. Top-view, two-dimensional schematics illustrate the crystallographic alignment of (a) MoO₂ (010) plane and (b) MoO₂ (001) plane with underlying 4H-SiC ($\sqrt{3}\times\sqrt{3}$)R30° surface reconstruction. Silicon atoms are indicated with blue circles (light blue for surface, darker blue for bulk), carbon with black, SiC surface oxygen atoms with purple, MoO₂ bulk oxygen atoms with red, and molybdenum with beige. Red parallelograms in each case represent MoO₂ unit cells and green parallelograms represent 4H-SiC ($\sqrt{3}\times\sqrt{3}$)R30° surface reconstruction repeating unit. Red text indicates MoO₂ crystallographic direction, green text indicates SiC direction, and black text indicates mismatch along specified directions. This figure is reproduced with permission from DeGregorio, et al. *J. Phys. Chem. Lett.* **2017**, 8 (7), 1631–1636.¹³⁵

Finally, while we have focused on the growth of MoO₂/MoS₂ platelets on silicon carbide, the mechanism that we propose for the aligned growth should be generalizable to create other structures. We note that *c*-cut sapphire has a hexagonal lattice and could also serve as a template for freestanding nanoparticles. The Al–O surface bonds should provide chemical anchors to form Al–O–Mo bonds, resulting in epitaxial freestanding plates. Indeed, under similar synthetic conditions, we observe the growth of freestanding, substrate-aligned MoO₂/MoS₂ plates (Figure 4.3e,f). Changing the chalcogen from sulfur to tellurium results in isomorphic structures composed of MoO₂/MoTe₂, as observed by SEM and Raman mapping (Figures 4.5g,h and 4.14). We hypothesize that this method

could be extended to any single-crystal substrate that has suitable symmetry, size, and chemical anchors to epitaxially nucleate the transition metal oxide. Furthermore, we propose that future experiments could change the symmetry of the substrate to favor a different interfacial plane of the MoO₂ core, creating a pathway to form TMDC nanoparticles with a wide variety of shapes and sizes.

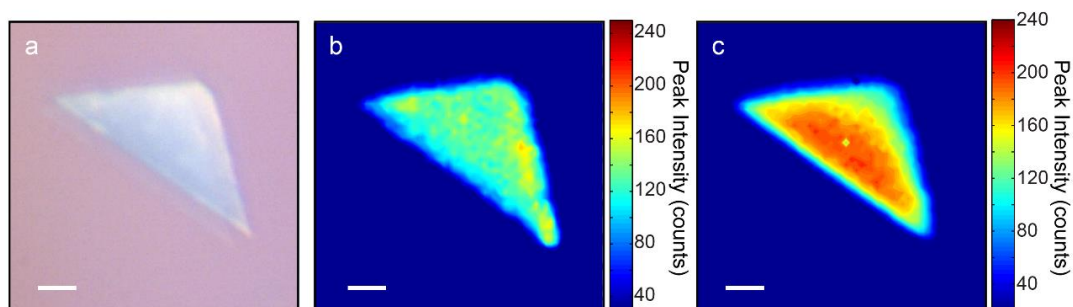


Figure 4.14. Optical image and Raman maps of MoO₂/MoTe₂ core-shell plate. (a) Optical image of a MoO₂/MoTe₂ core-shell plate. (b) Raman map of MoTe₂ 170 cm⁻¹ mode of the MoO₂/MoTe₂ core-shell plate. (c) Raman map of MoO₂ 747 cm⁻¹ mode of the MoO₂/MoTe₂ core-shell plate. All scale bars are 2 μm. This figure is reproduced with permission from DeGregorio, et al. *J. Phys. Chem. Lett.* **2017**, 8 (7), 1631–1636.¹³⁵

4.5 Conclusion

We have reported the novel growth of epitaxial, freestanding TMO/TMDC core/shell nanoplates. These core/shell plates were initially grown as MoO₂/MoS₂ core/shell plates on 4H-SiC, but they are also shown to grow on other substrates, in the case of MoO₂/MoS₂ plates grown on *c*-cut sapphire, and with other chalcogens, in the case of MoO₂/MoTe₂ core/shell plates on *c*-cut sapphire. The growth mechanism of these core/shell nanoplates is an extension of an established mechanism regarding self-seeding

TMDC monolayer growth. By delaying the chalcogen flux in this established mechanism, we can control the morphology of the TMO seed prior to chalcogenization. Delaying the chalcogen flux allows for the epitaxial growth of TMO plates on the substrate prior to the formation of the TMDC, but this modification could be extended to create TMO seeds of a variety of morphologies.

The method described here may be used as a general method for growing TMDC materials in a controlled, oriented manner and linking them to the substrate by a metallic core. The metallic TMO core could lead to improved charge injection in these heterostructures, due to the epitaxial, covalent bonding with the substrate. These TMO/TMDC core/shell nanoplates show promise in the field of catalysis, which requires high densities of active sites in good contact with a conductive substrate. The procedure described above should also be general to substrates of a variety of crystal structures, and as such, this scheme could allow for the growth of core/shell nanoplates grown in many epitaxial orientations. Finally, this modified mechanism offers pathways for creating new families of TMDC and TMO/TMDC nanoparticles controlled by substrate surface chemistry for future study.

Chapter 5

Metal-Semiconductor Heterostructures

5.1 Preface

Metal-semiconductor heterostructures are extremely important to consider in the context of electronics applications of TMDCs. Given that noble metals form contacts with high contact resistance, novel metal-semiconductor heterostructures must be investigated. Two different TMDC metal-semiconductor systems are investigated here.

First is the fabrication of in-plane 2H-1T' MoTe₂ homojunctions by the flux-controlled, phase engineering of few-layer MoTe₂ from Mo nanoislands. The phase of few-layer MoTe₂ in this system is controlled by changing the Te atomic flux controlled by the temperature of the reaction vessel. Few-layer 2H MoTe₂ is formed with high Te flux, few-layer 1T' MoTe₂ is formed with low Te flux, and few-layer in-plane 2H-1T' MoTe₂ homojunctions are formed with moderate Te flux. KPFM and Raman mapping confirm that in-plane 2H-1T' MoTe₂ homojunctions have abrupt interfaces between the two material domains, and they possess a potential difference of approximately 100 mV. This method is extended to a two-step lithographic process to create patterned junctions between 2H and 1T' MoTe₂. FETs of these in-plane 2H-1T' MoTe₂ homojunctions were subsequently fabricated, and the use of 1T' MoTe₂ as metallic electrodes in the FETs improves device performance by decreasing the contact resistance. The contact resistance extracted from transfer length method measurements is $470 \pm 300 \text{ } \Omega\text{-}\mu\text{m}$. Temperature-dependent transport characteristic measurements indicate a barrier height at the lateral 2H-1T' interface on the order of 10 meV, several times smaller than the metal-2H Schottky barrier height.

Secondly, lateral heterostructures between ML WS₂ and few-layer NbS₂ films are demonstrated here. These WS₂/NbS₂ heterostructures show abrupt edges between the two

materials, as indicated by SEM, Raman, AFM, KPFM, and PL mapping. FETs were also fabricated using these lateral WS₂/NbS₂ heterostructures. Preliminary device performance shows that the NbS₂ films are indeed metallic and show promise as a 2D TMDC contact material. However, due to device fabrication limitations related to sample degradation and resist under-exposure, the true electronic properties of WS₂/NbS₂ heterostructures have yet to be determined.

5.2 Introduction

5.2.1 Metal-Semiconductor Heterostructures

Metal-semiconductor heterostructures, as the name implies, describe the interface between a metal and a semiconductor. These heterostructures are typically designed with the intent of forming a FET or other electronic device that would use the semiconducting material as the channel and the metals on either side as contacts. When a semiconductor comes into contact with a metal, a barrier layer forms at the interface.⁷⁰ Charge carriers become depleted in this region, and thus it is referred to as the depletion region. Depending on the alignment of the metal's work function and the semiconductor's VB maximum and CB minimum, this depletion region can result in ohmic contact, in which charge can flow easily between both materials, or a Schottky barrier, in which the charge depletion induces a barrier that impedes the flow of charge.⁴⁷

Some of the most common electronic devices are based on bulk 3D channels comprised of silicon or III–V semiconductors, such as GaAs or GaN, connected by noble metal contacts, such as Au, Ag, or Pt.¹⁴⁹ Bulk devices have been developed to exhibit ideal device properties, including ohmic contacts, large on-off ratios, and good charge transfer

efficiency.^{150–152} Generally, such devices can be cost-effective and have been scalable down to nanoscale dimensions. However, as devices are continually pushed to smaller geometries, many of these traditional 3D devices struggle with fundamental limitations, including poor heat dissipation, high leakage currents, and tunneling effects.^{153–155} 2D materials, by nature of their sub-nanometer layer thickness and unique electronic properties, show promise for improved device properties in the small size limit.²⁰

5.2.2 Device Considerations for 2D Materials

Using traditional metal contacts for 2D semiconductor devices has been shown to induce a large contact resistance between the metal contact and 2D semiconductor.¹⁵⁶ The nature of this interface is very important, because a large contact resistance fundamentally limits the drain current and charge transfer efficiency of the device. The large contact resistance in 2D devices typically arises from the poor adhesion and general lack of chemical bonding that occurs between the deposited noble metal and 2D material due to the van der Waals forces at the 2D material surface. This contrasts with a bulk semiconductor device, in which covalent bonds can more easily form between the deposited metal and a reactive surface of a 3D semiconductor. The layered, van der Waals nature of all 2D materials generally prevents the possibility of binding with top-down deposited metals, giving rise to a tunneling barrier between the metal and the semiconductor in many 2D material devices.

One promising strategy for overcoming high-contact-resistance junctions with 2D semiconductors is to create lateral edge contacts.¹⁵⁶ 2D materials are more reactive at their edge sites, thus stronger chemical bonds more likely to form at the edges of a 2D material.

Modeling has shown that edge contacts lead to shorter bonding distances, stronger hybridization, and reduced overall contact resistance.^{156–159} These effects are especially pronounced in the case of 2D materials due to the large conductivity anisotropy between the in- and out-of-plane directions in 2D materials. It is also worth considering the choice of metal, as this can affect the overall contact resistance. While noble metals can be used to form edge contacts, it is difficult to control the precise contact position with traditional metal deposition, and thus it is difficult to control the charge injection pathway in the device. Metallic 2D materials can also be used, which can allow for native chemical bonding and fewer dangling bonds at the lateral interface. The efforts I have made to create metallic 2D TMDC contacts to semiconducting 2D TMDCs will be detailed in the remainder of this chapter.

5.2.3 In-Plane 2H-1T' MoTe₂ Homojunctions

The electronic properties of TMDCs are enriched by their polymorphism, with varying stacking orders and coordination geometry around the metal center that change the material properties.^{2,4,33,160} Traditionally, and most notably true for Mo- and W-based TMDCs, the 2H phase is semiconducting and features trigonal prismatic coordination, whereas the 1T phase is metallic and has octahedral coordination. Despite these enticing and disparate properties, tailoring the electronic properties of TMDCs is challenging, because of the metastability of 1T TMDCs and the large free energy difference between 2H and 1T TMDCs.^{161–163}

MoTe₂ is an exciting candidate material due to its large spin-orbit coupling and the fact that the 2H phase possesses a narrow band gap of 0.9–1.1 eV (notably similar to that

of Si, 1.1 eV).^{164–167} These properties make MoTe₂ an ideal candidate for spintronic devices, valleytronic devices, and optoelectronic devices operating in the near-infrared frequency range. One of the chief features of MoTe₂ is its phase tunability, originating from a relatively small free energy difference (40 meV per unit cell) between the 2H and 1T' phases of MoTe₂.^{162,168,169} Semiconducting 2H MoTe₂ is the most thermodynamically favorable phase, but semimetallic 1T' MoTe₂ (1T MoTe₂ that has undergone a Peierls distortion) can also be favored under specific conditions.^{141,170} 2H MoTe₂ has been reported to transform into 1T' MoTe₂ under applied tensile strain or by inducing Te deficiencies through laser illumination.^{168,169} If one could control the phase of MoTe₂ by simply controlling the reaction conditions, phase-patterned MoTe₂ could be mass produced for device fabrication.

Electronic and optoelectronic applications of 2D TMDCs require semiconductor–semiconductor junctions to allow for device functionality (e.g., p–n junctions, diodes, and FETs) and metal–semiconductor contacts to inject charges. As was discussed in Chapter 3, in-plane semiconducting TMDC heterostructures have been previously synthesized, and these heterostructures possess an abrupt change in electronic and optical properties across the atomically sharp junctions.^{76,83,84,101} Edge contacts have been formed in 2D material-based metal–semiconductor junctions to increase transistor “on” currents and effective charge mobility, as compared to traditional metal contacts.^{156,171} When the metal and semiconducting materials are two phases of the same material, the barrier to charge injection can be quite low, thereby resulting in ideal, minimally resistive, Ohmic contacts.^{161,168} Metal–semiconductor homojunctions in MoTe₂ have previously been fabricated via applied strain or laser illumination, but prior to this report, no group

has reported a direct synthetic approach for creating important metal–semiconductor homojunctions in any 2D material.

Here we report the fabrication of in-plane 2H-1T' MoTe₂ homojunctions using flux-controlled phase engineering of few-layer MoTe₂ from Mo nanoisland precursors. The phase of few-layer MoTe₂ is controlled by changing the Te atomic flux through the reaction vessel temperature. At high Te flux conditions, few-layer 2H MoTe₂ is formed, whereas few-layer 1T' MoTe₂ is obtained with low Te flux. Few-layer, in-plane 2H-1T' MoTe₂ homojunctions are synthesized using an intermediate Te flux condition. 2H-1T' MoTe₂ homojunctions are confirmed to have abrupt interfaces between the 2H and 1T' domains by Kelvin probe force microscopy (KPFM) and Raman mapping, with an approximately 100 mV potential difference between the domains. Furthermore, patterned few-layer 2H-1T' MoTe₂ heterostructures are fabricated using a phase-selective synthetic strategy. This flux-controlled phase engineering method could be utilized for the large-scale controlled fabrication of 2D metal–semiconductor junctions for future electronic and optoelectronic devices. This work is reproduced with permission from Yoo, et al.¹⁷²

5.2.4 2H-1T' MoTe₂ Devices

The in-plane 2H-1T' MoTe₂ homojunctions discussed in the previous section were used to fabricate in-plane field-effect transistors (FETs) to assess their electronic properties. As was discussed in Chapter 1, semiconducting TMDCs frequently have tunable bandgaps and ambipolar transport behavior, which makes them well-suited for use in CMOS logic circuits. Moreover, no devices with 1T' have been published yet using as-grown MoTe₂, and the detailed electrical properties of as-grown 2H-1T' MoTe₂ interfaces

have not yet been studied. This section on the fabrication and measurement of 2H-1T' MoTe₂ homojunction devices is presented as a summary of the work performed in collaboration with the Koester group at the University of Minnesota. The bulk of this work was performed by Rui Ma.

5.2.5 WS₂/NbS₂ Heterostructures

Interfacing semiconducting 2D TMDCs with other 2D materials has given rise to heterostructures of a wide range of properties. Increased control of growth conditions and sample preparation with 2D TMDCs has allowed for the design of increasingly complex 2D heterostructures and device geometries in recent years.^{78,171,173,174} However, many electronic devices featuring 2D materials suffer from large contact resistances at the metal contact interface, as was discussed earlier in this chapter.¹⁵⁶ Thus, it is imperative that the contact resistance be minimized to allow for accurate property measurement and optimal device performance.

One way to minimize the contact resistance of such a device is to form lateral heterostructures using a metallic 2D TMDC. In a lateral heterostructure, covalent bonds can form at the edge of the semiconducting TMDC layers, avoiding the involvement of the van der Waals surface in the device geometry. Some recently published works have utilized this strategy.^{161,175,176} Despite progress in this area, metal-semiconductor heterostructures have not yet been achieved using NbS₂, a metallic TMDC with a P6₃mc crystal structure. NbS₂ and WS₂ both have the same crystal structure and similar lattice constants ($a_{\text{NbS}_2} = 3.33 \text{ \AA}$, $a_{\text{WS}_2} = 3.16 \text{ \AA}$),¹⁷⁷ which should allow for favorable covalent bonding at the interface with minimal strain and few dangling bonds.

In this work, CVD-grown, monolayer WS₂ is used as a seed to grow few-layer NbS₂ in a lateral WS₂/NbS₂ heterostructure geometry. In this heterostructure, metallic NbS₂ functions as a 2D electrical contact to the semiconducting WS₂. These heterostructures were subsequently characterized, and electrical devices were made to determine the electronic effects of using NbS₂ as a contact material.

5.3 Experimental

5.3.1 In-Plane 2H-1T' MoTe₂ Homojunctions

In-plane 2H-1T' MoTe₂ homojunctions were synthesized from Mo nanoislands using a horizontal hot-wall tube furnace equipped with mass flow controllers and a vacuum pump, the same general setup as described above for MoS₂ growth. Mo nanoislands were deposited on SiO₂/Si substrates using an e-beam evaporation setup at the Minnesota Nano Center. Contact-mode AFM images and height line profiles show that the Mo nanoislands have heights of about 1–3 nm and widths of a few hundred nanometers (Figure 5.1), showing similar morphology to that of conventional transition metal nanoislands deposited by e-beam evaporation.¹⁷⁸ Te lump precursor was prepared by annealing Te slugs (0.8 g, 99.999%, Sigma Aldrich) at 635 °C for one hour under an Ar environment. Mo nanoislands on SiO₂/Si were placed face-down on an alumina boat containing the Te lump precursor placed at the center of the heating zone in a 3-inch quartz tube (MTI Corp.). After evacuating the quartz tube to less than 100 mTorr, Ar gas was flowed at a rate of 500 sccm until atmospheric pressure was reached. Ar and H₂ were then each flowed at a rate of 5 sccm. During the reaction, the furnace was ramped to 585 °C in 15 minutes and was kept

at this temperature for an hour. After the reaction, the furnace lid was opened so that the furnace would cool rapidly to room temperature.

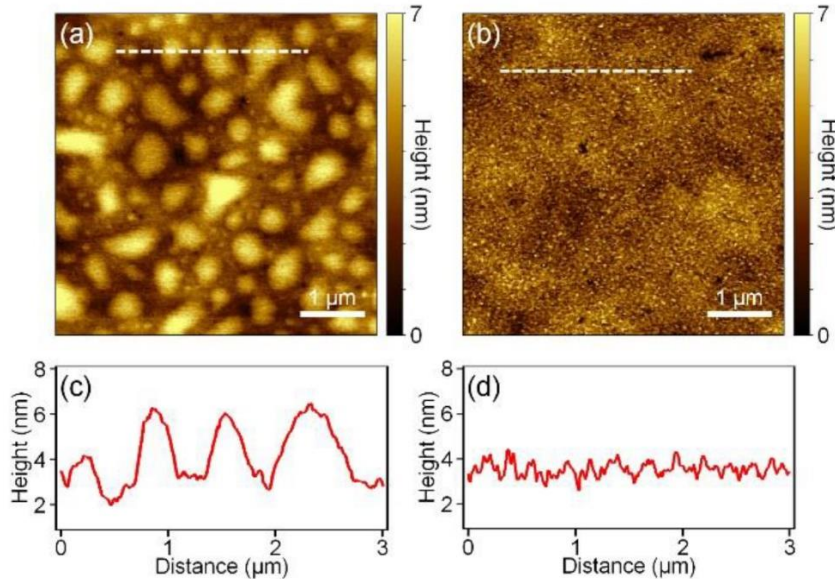


Figure 5.1. AFM of Mo nanoislands and in-plane 2H-1T' homojunctions. (a) AFM height image of Mo nanoislands deposited on SiO₂/Si substrates. (b) AFM height image of in-plane 2H-1T' homojunctions. (c) Height line profile along the dotted white line in (a). (d) Height line profile along the dotted white line in (b). This figure is reproduced with permission from Yoo, et al. *Adv. Mater.* **2017**, 29 (16), 1605461.¹⁷²

In-plane 2H-1T' MoTe₂ homojunction films are synthesized at a peak temperature of 585 °C, but this same procedure can be used to grow uniform films of few layer 2H MoTe₂ or 1T' MoTe₂ by simply changing the temperature of the reaction. 2H MoTe₂ is synthesized at 635 °C, whereas 1T' is synthesized at 535 °C. Given that the reaction times are the same in each of these cases, the linear ramp rate in each case was slightly different: ~41 °C/min for 2H MoTe₂, ~37 °C/min for in-plane 2H-1T' homojunctions, and ~34 °C/min for 1T' MoTe₂ films.

Using a phase selective synthetic strategy, we also demonstrate the patterning of few-layer 2H-1T' junctions. The fabrication process is illustrated in Figure 5.2. First, few-layer 1T' MoTe₂ is synthesized from Mo nanoislands with low Te flux. These few-layer 1T' MoTe₂ samples were subsequently spincoated with (methyl methacrylate) (PMMA) (MW ~950000). We wrote patterns using a Vistec EBPG 5000+ system, developed the PMMA in 1:3 MIBK:IPA, and rinsed the sample in IPA. Using the PMMA patterns as a protecting mask, the unmasked few-layer 1T' MoTe₂ was etched away in 30% H₂O₂ aqueous solutions for 3 min, and Mo nanoislands were deposited on the sample through e-beam evaporation. The PMMA was lifted off in acetone for 30 minutes to obtain patterned regions of 1T' MoTe₂ and Mo nanoislands, which were subsequently annealed with high flux to make few-layer 2H-1T' MoTe₂ patterns.

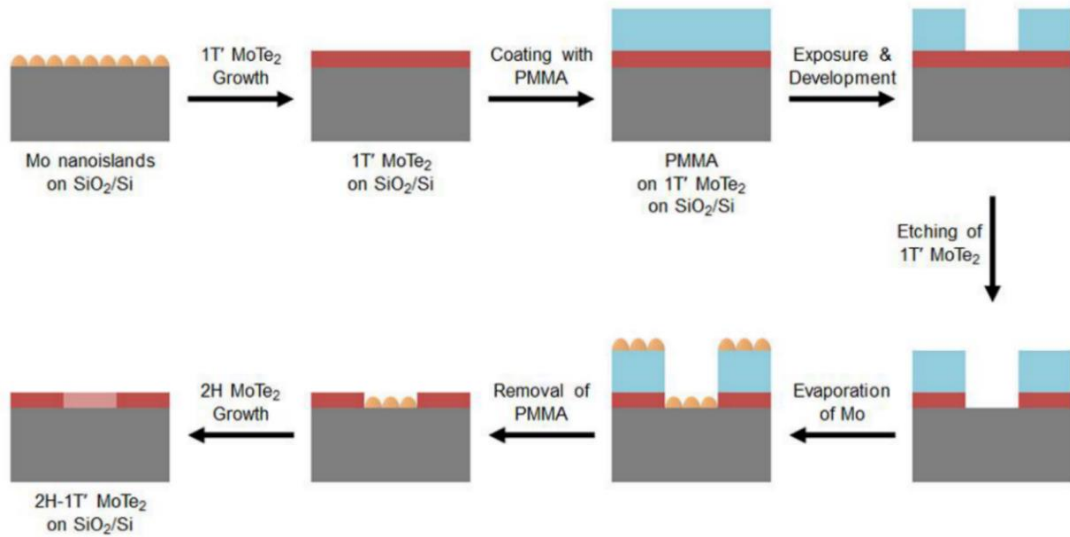


Figure 5.2. Schematic illustration of the fabrication procedure for few-layer 2H-1T' MoTe₂ patterns. This figure is reproduced with permission from Yoo, et al. *Adv. Mater.* **2017**, 29 (16), 1605461.¹⁷²

Contact-mode AFM measurements were performed on a Bruker Nanoscope V Multimode 8 SPM using silicon tips with nominal force constant of 0.60 N/m. KPFM measurements were performed using a Bruker SCM-PIT probe possessing an electrically conductive Pt-Ir coated tip with a tip radius of about 20 nm. Raman spectra and the maps were acquired using a 632.8 nm laser excitation focused through a 100x objective lens with a power of 30 μ W at room temperature. SEM images were taken on a JEOL JSM-6500F SEM operated at an accelerating voltage of 5 kV. XRD measurements were performed on a Bruker D8 Discover equipped with a 2D X-ray diffractometer using a Co $K\alpha$ radiation point source.

In this work, I acquired the AFM and KPFM data of the in-plane 2H-1T' MoTe₂ homojunctions. I also contributed intellectually to the realization of these experiments and have since replicated their results. The synthesis of in-plane 2H-1T' MoTe₂ homojunctions for this work and all other material characterization was performed by Youngdong Yoo.

5.2.2 2H-1T' MoTe₂ Devices

In-plane 2H-1T' MoTe₂ homojunction samples were patterned and etched into rectangular bars of 2H, 1T', and 1T'-2H-1T' MoTe₂ regions, upon which contacts of Ti/Au (10 nm/80 nm) were patterned and deposited. These devices were used to assess the device performance of MoTe₂ devices with and without the use of conducting 1T' MoTe₂ as an electrical contact.

This work is presented as a summary of work performed largely by Rui Ma in the Koester group. In these experiments, I was responsible for certain portions of the in-plane

2H-1T' MoTe₂ homojunction synthesis, as well as the Raman mapping. Much of the experimental design was performed by Rui Ma and Youngdong Yoo, and all of the device performance measurement was performed by Rui Ma and collaborators in the Koester and Low groups.

5.2.3 WS₂/NbS₂ Heterostructures

Ultraclean WS₂ monolayers were synthesized using a procedure reported previously.⁸⁴ A Lindberg/Blue M hot-wall, single-zone tube furnace was equipped with mass flow controllers and an Edwards RV8 vacuum pump. An alumina boat containing 500 mg of WO₃ powder (99.998 %, Alfa Aesar) was placed at the center of the furnace in a 2-inch diameter quartz tube. A *c*-cut sapphire substrate was placed polished-face-up on an upside-down alumina boat, which was placed a few centimeters downstream from the center of the furnace. Sulfur pieces (99.999 %, Alfa Aesar) were located in another alumina boat upstream from the center of the furnace. After evacuating the tube to less than 10 mtorr, Ar gas at 400 sccm was used to purge the tube. The Ar flow rate was then reduced to 60 sccm (standard cubic centimeters per minute) and H₂ gas was introduced at 15 sccm, maintaining a chamber pressure of 550 mtorr during the reaction. The furnace was heated to 1050 °C at a rate of 11 °C/min and kept at 1050 °C for 5 min. The temperatures of the substrate and sulfur powder were measured to be approximately 940 °C and 160 °C, respectively. The furnace was rapidly cooled after the reaction.

To synthesize WS₂/NbS₂ heterostructures, monolayer WS₂ grown on *c*-cut sapphire was used as a substrate for NbS₂ film growth. The NbS₂ film growth described here is very similar to the chloride-based, few-layer NbS₂ growth described in Chapter 2. WS₂/sapphire

substrates were placed at the center of the furnace in a 2-inch quartz tube, while S pieces and 100 mg NbCl₅ powder were placed upstream from the center of the furnace. Prior to loading, NbCl₅ powder was kept in a sealed vial with an Ar-rich atmosphere. Ar gas was introduced at 200 sccm prior to precursor loading and tube evacuation, to create an Ar-rich environment and minimize ambient degradation of the NbCl₅ powder during setup. After evacuating the tube, Ar gas was used to purge the tube. Ar and H₂ gas were then introduced at rates of 60 and 5 sccm, respectively, and the reaction was carried out at low pressure (~400 mtorr). The center of the furnace was heated to approximately 1000 °C at an average rate of 11 °C/min. After the S precursor remained molten for 7 min, the furnace was rapidly cooled.

Raman spectra and optical images were acquired using a Raman microscopy setup featuring 532 nm laser excitation aligned through a 100x objective lens with incident power of approximately 200 μW. AFM data was acquired in tapping mode on a Bruker Nanoscope V Multimode 8 SPM using Si tips with nominal force constant of 42 N/m. KPFM measurements were performed using a Bruker SCM-PIT-V2 probe comprised of a Pt–Ir tip with radius of approximately 20 nm. SEM images and EDS data were acquired using a JEOL JSM-6500F SEM and TEM images were acquired using a FEI Tecnai G2 F30 TEM. SEM, EDS, and TEM characterization was performed with the help of Nick Seaton and Jason Myers in the Characterization Facility at the University of Minnesota.

To ascertain the effectiveness of the NbS₂ as a contact material in these heterostructures, we have patterned samples in a metal–semiconductor–metal device geometry (NbS₂–WS₂–NbS₂) using e-beam lithography, with isolated regions of monolayer WS₂ laterally connected only to regions of NbS₂. Similar to the results presented

in Section 5.2.2, this work was done in collaboration with the Koester group, with the device fabrication performed by Rui Ma. Ti/Au (10 nm/80 nm) electrodes were deposited on top of the metallic NbS₂ film regions to read out the electronic properties of the patterned devices, and printed ion gels were deposited on top of the flakes to function as a top gate. NbS₂-only and WS₂-only control devices were also fabricated, in which isolated regions of each single material were used for depositing electrodes and top-gate ion gels. Aside from the device work and the SEM, EDS, and TEM characterization, all synthesis and characterization of these materials was performed by the author.

5.4 Results and Discussion

5.4.1 In-Plane 2H-1T' MoTe₂ Homojunctions

The MoTe₂ films obtained from the Mo nanoisland tellurization method can be seen in Figure 5.3. These MoTe₂ films are continuous and possess root-mean-square (RMS) roughness of about 0.88 nm, as determined by AFM, which is relatively smooth compared to the the 0.5–1 nm roughness of the underlying SiO₂/Si substrates. The thickness of these films were measured to be about 3.5 nm, consistent with the thickness of five layers of MoTe₂ (see Figure 5.4).^{140,179}

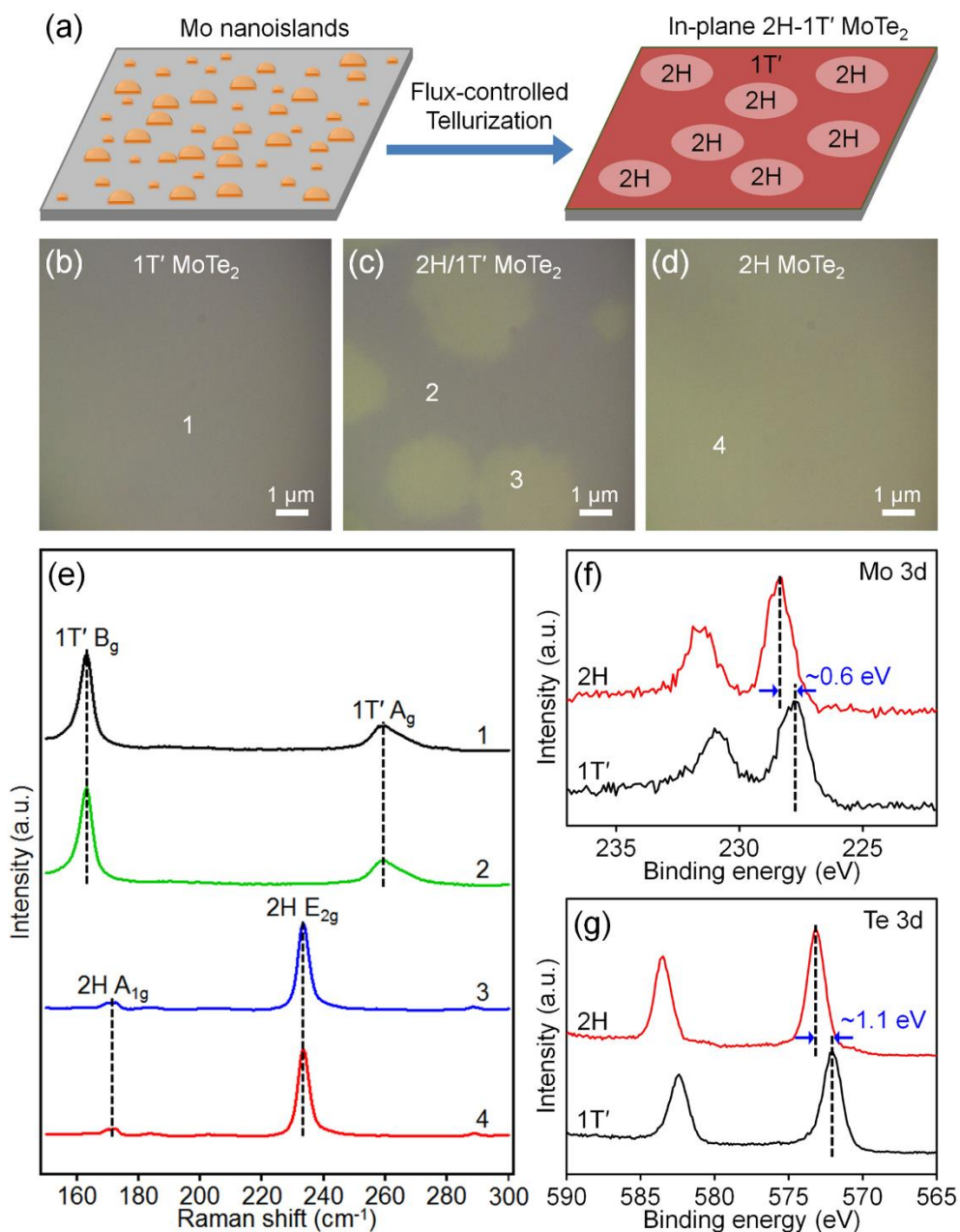


Figure 5.3. Growth of in-plane 2H-1T' MoTe₂ homojunctions from Mo nanoislands. (a) Schematic illustration of the growth process. (b–d) Optical image of few-layer 2H, in plane 2H-1T', and 1T' MoTe₂ synthesized at 635, 585, and 535 °C, respectively (e) Raman spectra acquired at the points marked by 1-4 in (b–d). (f) High-resolution XPS spectra showing Mo 3d peaks of few-layer 2H and 1T' MoTe₂. (g) High-resolution XPS spectra showing Te 3d peaks of few-layer 2H and 1T' MoTe₂. The Mo 3d and Te 3d peaks of few-layer 1T' MoTe₂ are downshifted by ~0.6 eV and ~1.1 eV, respectively, compared to those of few-layer 2H MoTe₂. This figure is reproduced with permission from Yoo, et al. *Adv. Mater.* **2017**, 29 (16), 1605461.¹⁷²

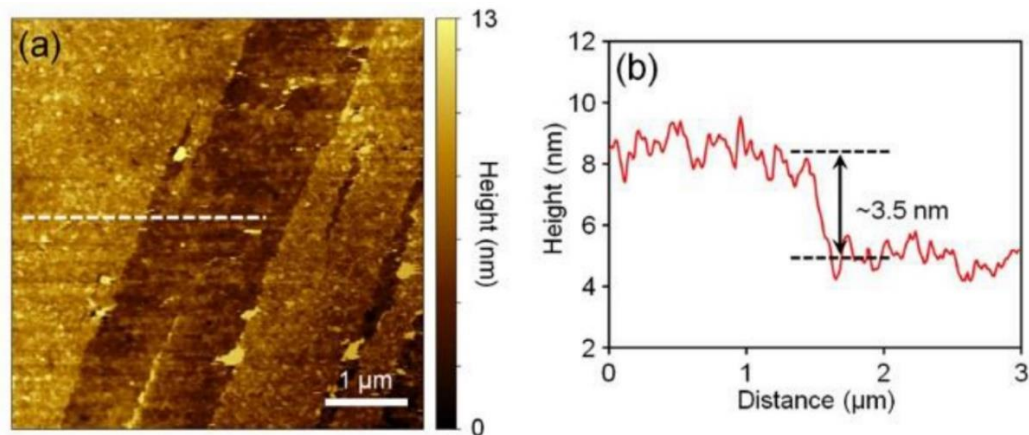


Figure 5.4. AFM of scratched in-plane 2H-1T' MoTe₂ films. (a) AFM height image of in-plane 2H-1T' MoTe₂ films with tweezer scratch. (b) Height line profile along the dotted white line in (a). This figure is reproduced with permission from Yoo, et al. *Adv. Mater.* **2017**, 29 (16), 1605461.¹⁷²

Optical images of few-layer MoTe₂ films show that the MoTe₂ in each case is very uniform, with large optical contrast between 1T' and 2H MoTe₂ domains. The change in optical contrast between the 1T' and 2H MoTe₂ is due to the change in the visible absorption spectrum of each phase.^{141,164} Raman spectra taken from different points of a 2H/1T' homojunction show that each domain exhibits phase-specific characteristic Raman peaks: the B_g (163.0 cm⁻¹) and A_g (260.1 cm⁻¹) modes for 1T' MoTe₂, and the A_{1g} (170.9 cm⁻¹) and E_{2g} (233.5 cm⁻¹) modes for 2H MoTe₂.^{164,180} The crystal structures of as-synthesized few-layer 2H and 1T' MoTe₂ were confirmed by XRD (Figure 5.5).

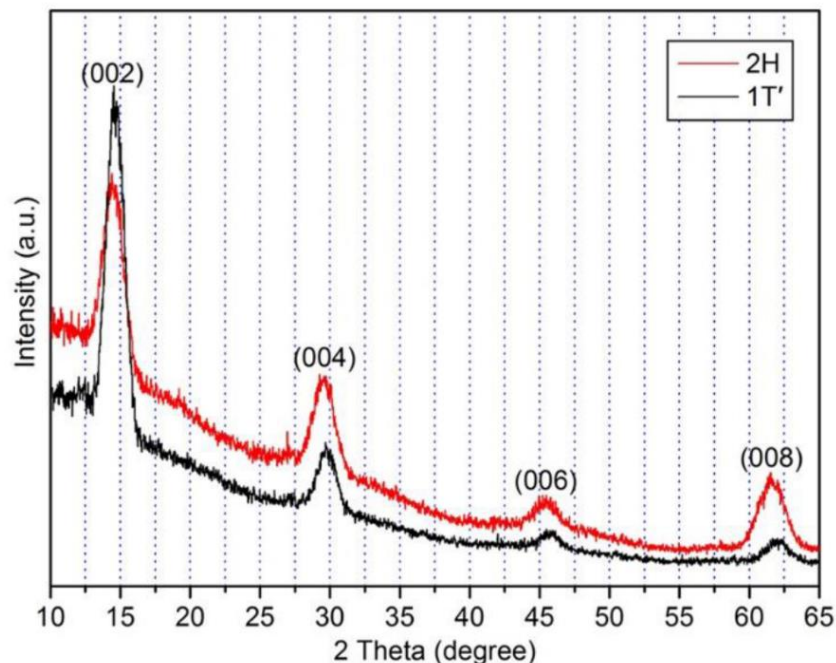


Figure 5.5. XRD patterns of few-layer 2H (red) and 1T' (black) MoTe₂. The peaks of as synthesized few-layer 2H and 1T' MoTe₂ are indexed to hexagonal 2H MoTe₂ (JCPDS #73-1650) and monoclinic 1T' MoTe₂ (JCPDS #71-2157), respectively. This figure is reproduced with permission from Yoo, et al. *Adv. Mater.* **2017**, 29 (16), 1605461.¹⁷²

XPS measurements allowed for the analysis of the elemental composition and chemical states of few-layer MoTe₂. The presence of elemental Mo and Te are confirmed in few-layer 2H and few-layer 1T' films by the XPS survey spectrum. Also present in the survey spectrum are adventitious C and O signal, which originate from atmospheric transfer of the material. These signals were used to calibrate the electron binding energies. The high-resolution XPS peaks for 2H MoTe₂ were observed at 228.4 eV (Mo 3d_{5/2}), 231.5 eV (Mo 3d_{3/2}), 573.1 eV (Te 3d_{5/2}), and 583.5 eV (Mo 3d_{3/2}). The high-resolution XPS peaks for 1T' MoTe₂ were observed at 227.8 eV (Mo 3d_{5/2}), 230.9 eV (Mo 3d_{3/2}), 572.0 eV (Te 3d_{5/2}), and 582.4 eV (Mo 3d_{3/2}). The XPS peaks for 1T' MoTe₂ are reportedly downshifted by about 0.4–0.6 eV from the XPS peaks of 2H MoTe₂.^{140,168,179} In our few-

layer 1T' MoTe₂, however, the Te 3d peaks are downshifted by ~1.1 eV, whereas the Mo 3d peaks are downshifted by ~0.6 eV. We attribute this additional downshifting of the Te 3d peaks to Te deficiency. Chalcogen deficiency in TMDCs reportedly decreases the binding energy of the chalcogen while maintaining the same binding energy of the transition metal,¹⁸¹ which is consistent with our XPS measurements (Figure 5.6). The Te/Mo atomic ratios of the MoTe₂ films were quantified by comparing the area ratio of Mo 3d-to-Te 3d peaks of 2H MoTe₂ with that of 1T' MoTe₂. When the value of this Te/Mo atomic ratio for 2H MoTe₂ is normalized to 2.00, the Te/Mo atomic ratio of 1T' MoTe₂ is calculated to be about 1.86.

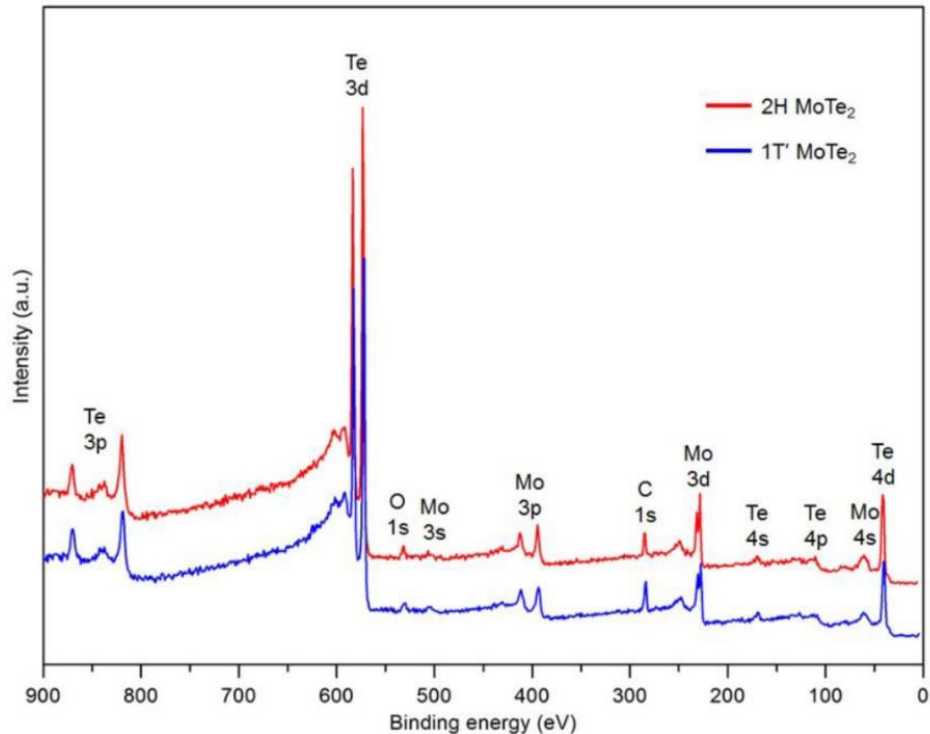


Figure 5.6. XPS survey spectrum of few-layer 2H (red) and 1T' (blue) MoTe₂. This figure is reproduced with permission from Yoo, et al. *Adv. Mater.* **2017**, 29 (16), 1605461.¹⁷²

Based on the Te deficiency present in these few-layer 1T' MoTe₂ films, we hypothesize that the flux of Te during the growth determines the phase of MoTe₂, consistent with the previously reported crystal growth.^{141,182} The experiments presented in Figure 5.3 conflate two variables: substrate temperature and Te flux. Figure 5.7 shows a series of reactions performed to exclude the influence of substrate temperature on the resulting films. In these experiments, the Te flux was controlled independently by keeping the substrate temperature at 635 °C and placing the Te lump at four different positions in the growth tube: A (635 °C), B (585 °C), C (535 °C), and D (485 °C). The vapor pressure of Te was calculated to be approximately 10.9, 4.5, 1.7, and 0.5 Torr for the 635, 585, 535, and 485 °C conditions, respectively.¹⁸³ Flux, defined as the number of deposited atoms per unit time and area, is proportional to the vapor pressure. To this end, the Te flux at 635 °C is estimated to be approximately 20 times greater than at 485 °C. Stokes and anti-Stokes Raman spectra show that sample A (Te temperature of 635 °C) exhibits characteristic Raman peaks of 2H MoTe₂, while sample C (Te temperature of 535 °C) shows characteristic Raman peaks of 1T' MoTe₂. Sample B (Te temperature of 585 °C) shows Raman peaks corresponding to both 2H and 1T' MoTe₂, indicating that the sample is composed of both 2H and 1T' MoTe₂. Sample D (Te temperature of 485 °C) exhibits shifted Raman peaks of 1T' MoTe₂, likely due to the severe Te deficiency present in the sample as a result of the dramatically decreased Te flux. Additional Raman measurements and Lorentzian fitting results are shown in Figure 5.8.

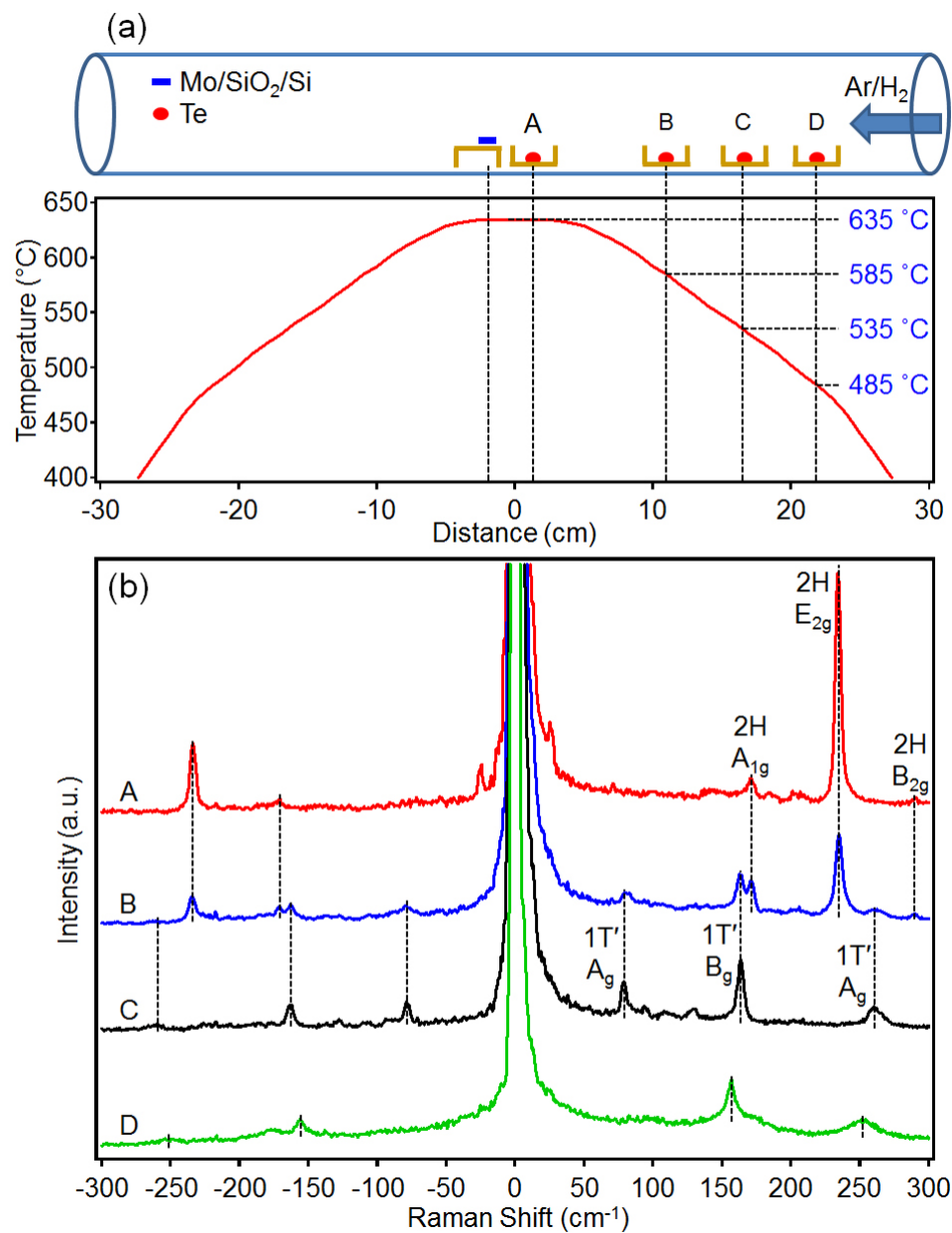


Figure 5.7. Flux-controlled phase engineering of few-layer MoTe₂. (a) Schematic illustration of the experimental setup for flux-controlled reactions and the temperature profiles of the furnace heated to 635 °C. Te lump was placed at positions of A (635 °C), B (585 °C), C (535 °C), and D (485 °C) for the syntheses of few-layer 2H, mixed 2H-1T', 1T', and defective 1T' MoTe₂, respectively. The temperature of Mo nanoislands on SiO₂/Si substrates was kept at 635 °C for all experiments. (b) Stokes and anti-Stokes Raman spectra of few-layer 2H, mixed 2H-1T', 1T', and defective 1T' MoTe₂ synthesized at Te temperatures of 634, 585, 535, and 485 °C, respectively. This figure is reproduced with permission from Yoo, et al. *Adv. Mater.* **2017**, 29 (16), 1605461.¹⁷²

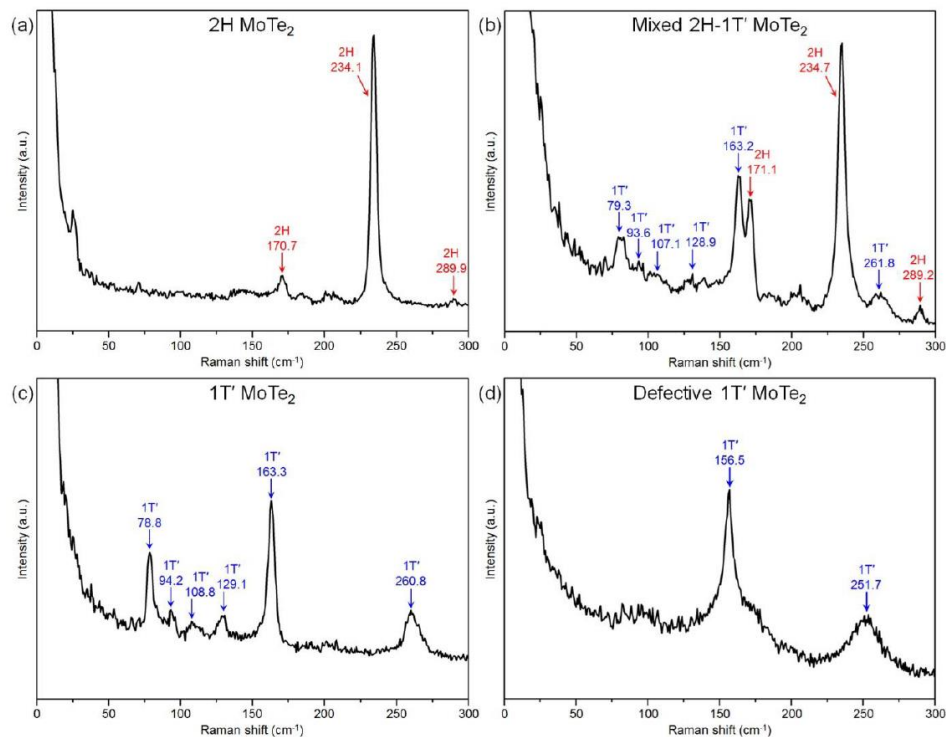


Figure 5.8. Raman spectra and Lorentzian fitting results of few-layer 2H, mixed 2H-1T', 1T', and defective 1T' MoTe₂. This figure is reproduced with permission from Yoo, et al. *Adv. Mater.* **2017**, 29 (16), 1605461.¹⁷²

This synthesis is assumed to be in thermodynamic control, given that the Mo nanoislands are annealed in a Te environment for long enough that they can reach thermodynamic equilibrium. This is further supported by the observation that the changes in phase are driven by the Te chemical potential. Density functional theory (DFT) calculations have previously predicted that 2H MoTe₂ is the most thermodynamically stable phase for stoichiometric MoTe₂, whereas the 1T' phase becomes more stable as the Te vacancy concentration increases.¹⁶⁸ Here, it is demonstrated experimentally that the MoTe₂ phase is determined thermodynamically by the Te vacancy concentration, and we provide optimum quantitative values of vapor pressures for the growth of 2H, mixed 2H-1T', and 1T' MoTe₂.

The in-plane 2H-1T' MoTe₂ homojunctions are further characterized by Raman mapping and KPFM (Figure 5.9). An optical image of the 2H-1T' MoTe₂ region used for Raman mapping shows clear optical contrast between the 2H and 1T' domains. Raman spectra indicate that the inner, circular area is composed of 2H MoTe₂, whereas the outer region is composed of 1T' MoTe₂. Raman maps of the 2H MoTe₂ E_{2g} mode and the 1T' MoTe₂ B_g mode show that the junctions between the 2H and 1T' MoTe₂ domains are abrupt. An AFM height image and corresponding height line profile show that no significant height difference exists between the 2H and 1T' regions. A KPFM image and corresponding potential line profile confirm that a sharp 100 mV potential difference exists between the 2H and 1T' MoTe₂ domains. KPFM measures the contact potential difference (CPD) between the scanning probe tip and the material.¹⁸⁴ CPDs measured on 2H and 1T' MoTe₂ are defined to be $[\Phi(\text{tip}) - \Phi(2\text{H MoTe}_2)]/e$ and $[\Phi(\text{tip}) - \Phi(1\text{T}' \text{ MoTe}_2)]/e$, where $\Phi(\text{tip})$, $\Phi(2\text{H MoTe}_2)$, and $\Phi(1\text{T}' \text{ MoTe}_2)$ are the work functions for the tip, 2H MoTe₂, and 1T' MoTe₂, respectively. Based on the KPFM measurement, the work function difference between the 2H and 1T' MoTe₂ domains, $\Phi(2\text{H MoTe}_2) - \Phi(1\text{T}' \text{ MoTe}_2)$, is calculated to be approximately 100 meV. This work function difference can be attributed to the Te deficiency in 1T' MoTe₂ and the electronic structure difference between 2H and 1T' MoTe₂. An atomic model of in-plane 2H-1T' MoTe₂ junctions is illustrated in Figure 5.9i.

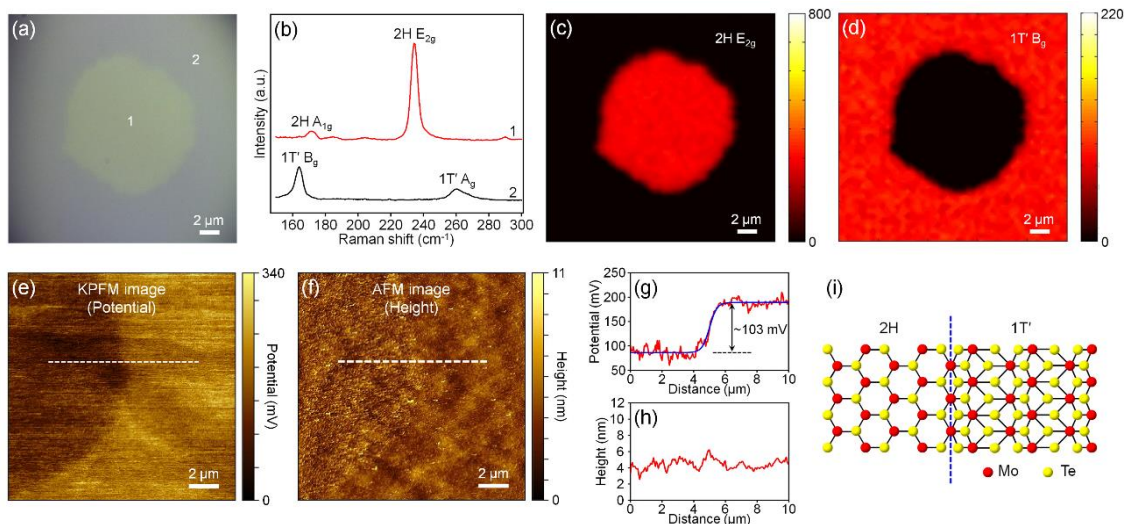


Figure 5.9. Raman mapping and KPFM study of in-plane 2H-1T' MoTe₂ homojunctions. (a) Optical image of in-plane 2H-1T' MoTe₂ homojunctions. (b) Raman spectra taken from the points marked by 1 and 2 in (a). (c) Raman intensity map of the E_{2g} mode of 2H MoTe₂. (d) Raman intensity map of the B_g mode of 1T' MoTe₂. (e) KPFM potential image of the in-plane 2H-1T' MoTe₂ homojunctions. (f) AFM height image of the in-plane 2H-1T' MoTe₂ homojunctions. (g) Potential line profile along the dotted white line in (e). (h) Height line profile along the dotted white line in (f). (i) Atomic model of an in-plane junction between 2H and 1T' MoTe₂. This figure is reproduced with permission from Yoo, et al. *Adv. Mater.* **2017**, 29 (16), 1605461.¹⁷²

Using a phase selective synthetic strategy, we also demonstrate the patterning of few-layer 2H-1T' junctions (Figure 5.10). A crucial observation of these patterns is that the phase of few-layer 1T' MoTe₂ is conserved without phase change or decomposition during the annealing step with high Te flux (Figure 5.11). We believe this is due to Te atoms being unable to effectively incorporate into the lattices of previously synthesized few-layer 1T' MoTe₂ under the high Te flux conditions. Generally, once MoTe₂ has been grown in a specific phase, it becomes kinetically trapped in that phase under our reaction conditions. The 2H-1T' MoTe₂ patterns fabricated by this method show a sharp optical

contrast between the inner and outer regions. Raman measurements and mapping confirm that the inner and outer domains of these patterned junctions are 2H and 1T' MoTe₂, respectively, and that the junction features abrupt interfaces between the 2H and 1T' domains.

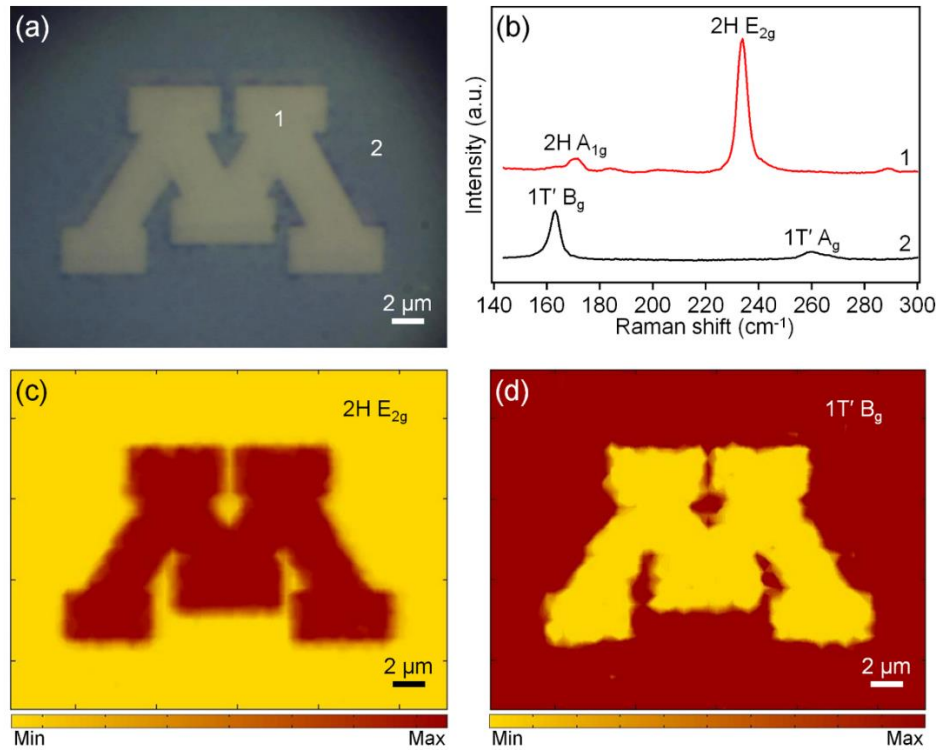


Figure 5.10. Fabrication of few-layer 2H-1T' MoTe₂ patterns. (a) Optical image of 2H-1T' MoTe₂ patterns. (b) Raman spectra taken from the points marked by 1 and 2 in (a). (c) Raman intensity map of the E_{2g} mode of 2H MoTe₂. (d) Raman intensity map of the B_g mode of 1T' MoTe₂. This figure is reproduced with permission from Yoo, et al. *Adv. Mater.* **2017**, 29 (16), 1605461.¹⁷²

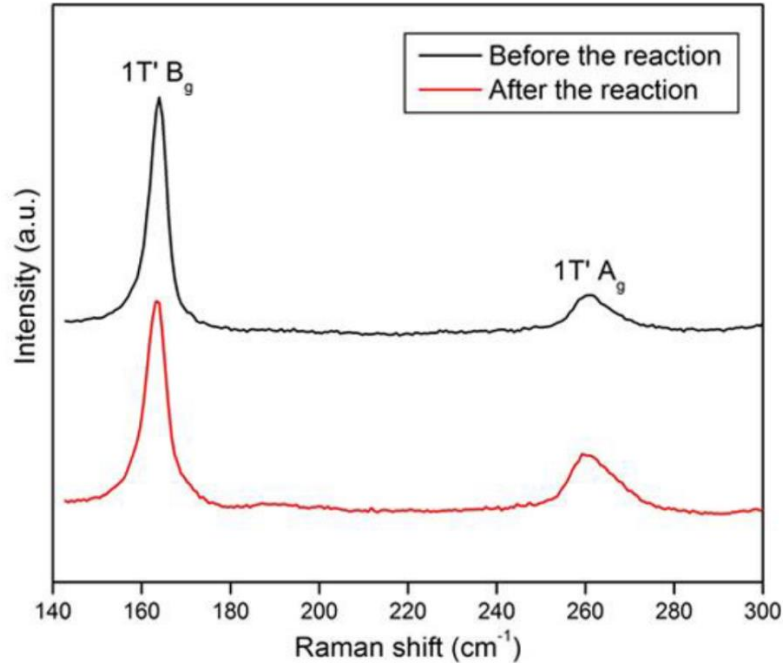


Figure 5.11. Phase conservation of few-layer 1T' MoTe₂ during annealing with high Te flux. Raman spectra of the 1T' MoTe₂ before (black) and after (red) annealing with high Te flux. This figure is reproduced with permission from Yoo, et al. *Adv. Mater.* **2017**, 29 (16), 1605461.¹⁷²

5.4.2 2H-1T' MoTe₂ Devices

The in-plane 2H-1T' MoTe₂ homojunctions discussed in the previous section were used to fabricate in-plane field-effect transistors (FETs) to assess their electronic properties. Figure 5.12 shows an optical image and Raman peak intensity maps of representative 1T'-2H-1T' MoTe₂ devices, showing optical contrast and Raman peak intensity differences between the interior 2H and exterior 1T' regions that indicate an abrupt junction between the two phases.

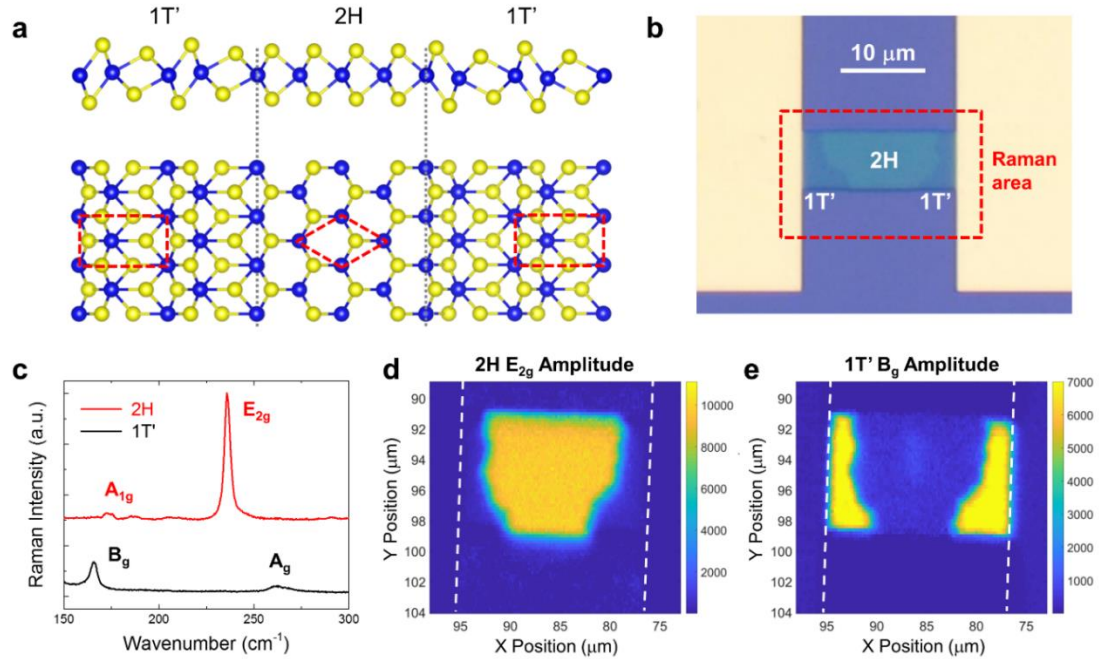


Figure 5.12. Schematic illustration and Raman mapping of 1T'-2H-1T' MoTe₂ devices. (a) Schematic diagram of an in-plane, monolayer 1T'-2H-1T' MoTe₂ homojunction. The top schematic in (a) is a cross-section view and the bottom is a basal plane view, with blue spheres representing Mo atoms, yellow spheres representing Te atoms, and the red dashed boxes representing primitive unit cells. (b) Optical image of a few-layer 1T'-2H-1T' MoTe₂ device. (c) Raman spectra acquired from the 1T' and 2H regions in (b). (d) and (e) are Raman intensity maps of the E_{2g} mode of 2H MoTe₂ and the B_g mode of 1T' MoTe₂, respectively, acquired from the region indicated by the red dashed rectangle in (b). White dashed lines in (d) and (e) indicate the borders of the Ti/Au contacts. This figure is reproduced with permission from Ma, et al. Manuscript in preparation.

The transfer length method was used to determine the contact resistances of 1T'-only and 2H-only devices (Figure 5.13). The contact resistance between Ti/Au and 1T' MoTe₂ was determined to be $0.47 \pm 0.03 \text{ k}\Omega\text{-}\mu\text{m}$ and the sheet resistance of the 1T' MoTe₂ was determined to be $2.65 \pm 0.09 \text{ k}\Omega\text{-}\mu\text{m}$ with no applied backgate voltage (V_{BG}), which are comparable to the lowest published resistance values for phase-transitioned FETs of TMDCs (200–300 $\Omega\text{-}\mu\text{m}$).¹⁶¹ The contact resistance between Ti/Au and 2H MoTe₂ was

determined to be $15.6 \pm 0.58 \text{ M}\Omega\text{-}\mu\text{m}$, with sheet resistance of $5.67 \pm 0.7 \text{ M}\Omega\text{-}\mu\text{m}$ at $V_{\text{BG}} = -100 \text{ V}$, which indicates that the contact resistance of a MoTe_2 device can be reduced by approximately 4 orders of magnitude when using $1\text{T}'$ MoTe_2 as the contact material. The back-gate dependence of the 2H-only device contact resistance is shown in Figure 5.13b, which indicates that the contact resistance increases with increasing V_{BG} .

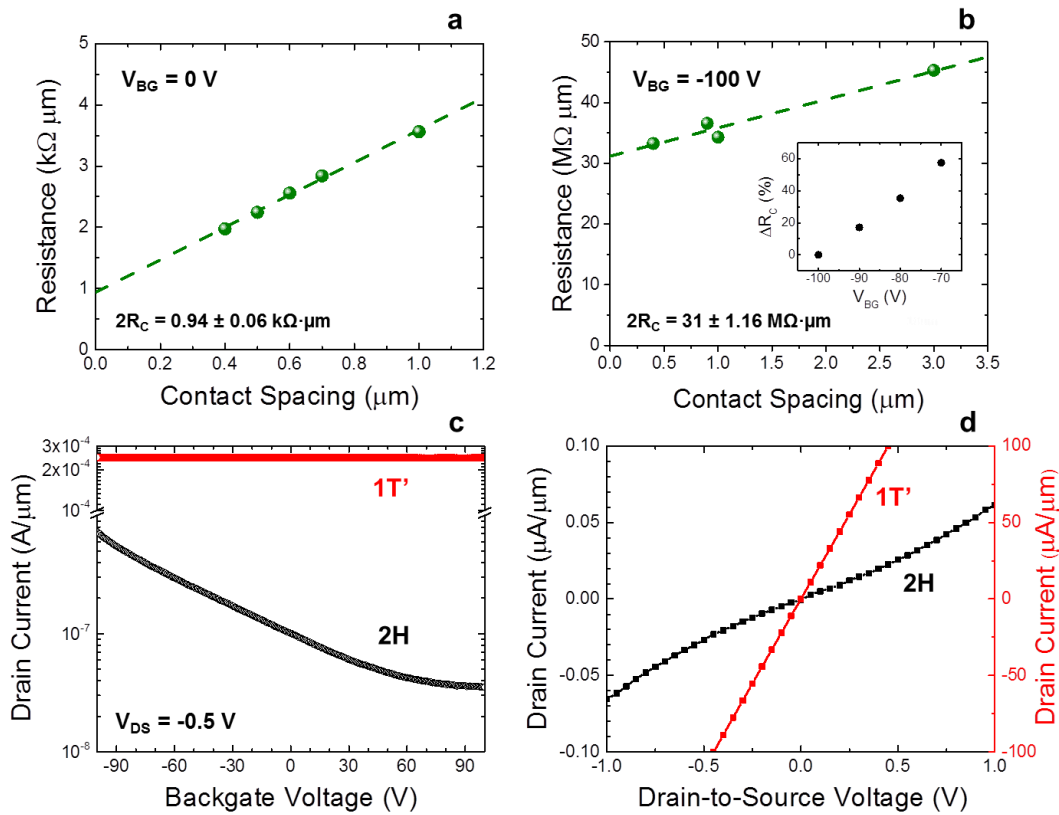


Figure 5.13. Transfer length measurements and device characteristics. (a) Resistance vs. contact spacing for the $1\text{T}'$ device at $V_{\text{BG}} = 0 \text{ V}$. (b) Resistance vs. contact spacing for the 2H device at $V_{\text{BG}} = -100 \text{ V}$ and $V_{\text{DS}} = -0.1 \text{ V}$. The inset in (b) is the percentage change of contact resistance at four different values of V_{BG} . (c) Room temperature transfer characteristics of the $1\text{T}'$ and 2H devices at $V_{\text{DS}} = -0.5 \text{ V}$. (d) Room temperature output characteristics of the $1\text{T}'$ device at $V_{\text{BG}} = 0 \text{ V}$ and the 2H device at $V_{\text{BG}} = -100 \text{ V}$. This figure is reproduced with permission from Ma, et al. Manuscript in preparation.

Room-temperature transfer characteristics of drain current (I_D) vs. V_{BG} of 1T'-only and 2H-only devices (Figure 5.13c) indicate that the 1T'-only device shows high drive current (245 $\mu\text{A}/\mu\text{m}$ at $V_{DS} = -0.5$ V) and no gate modulation, thereby confirming its metallicity. The 2H-only device shows typical metal-oxide-semiconductor field-effect transistor (MOSFET) transfer characteristic with a current on/off ratio of $\sim 10^3$, possibly affected by defects in the channel. The interface trap density of this device is calculated to be $\sim 10^{13}$ cm^{-2}/eV at room temperature. The room-temperature output characteristics (I_D vs. V_{DS}) of the 1T'-only device (Figure 5.13d) show that the current of the 1T'-only device is more than 4 orders of magnitude larger than that of the 2H-only device at the same V_{DS} . Additionally, the 1T'-only device shows a linear relationship whereas the 2H-only device shows nonlinear behavior, supporting the assignment of 1T' and 2H MoTe₂ as metallic and semiconducting, respectively.

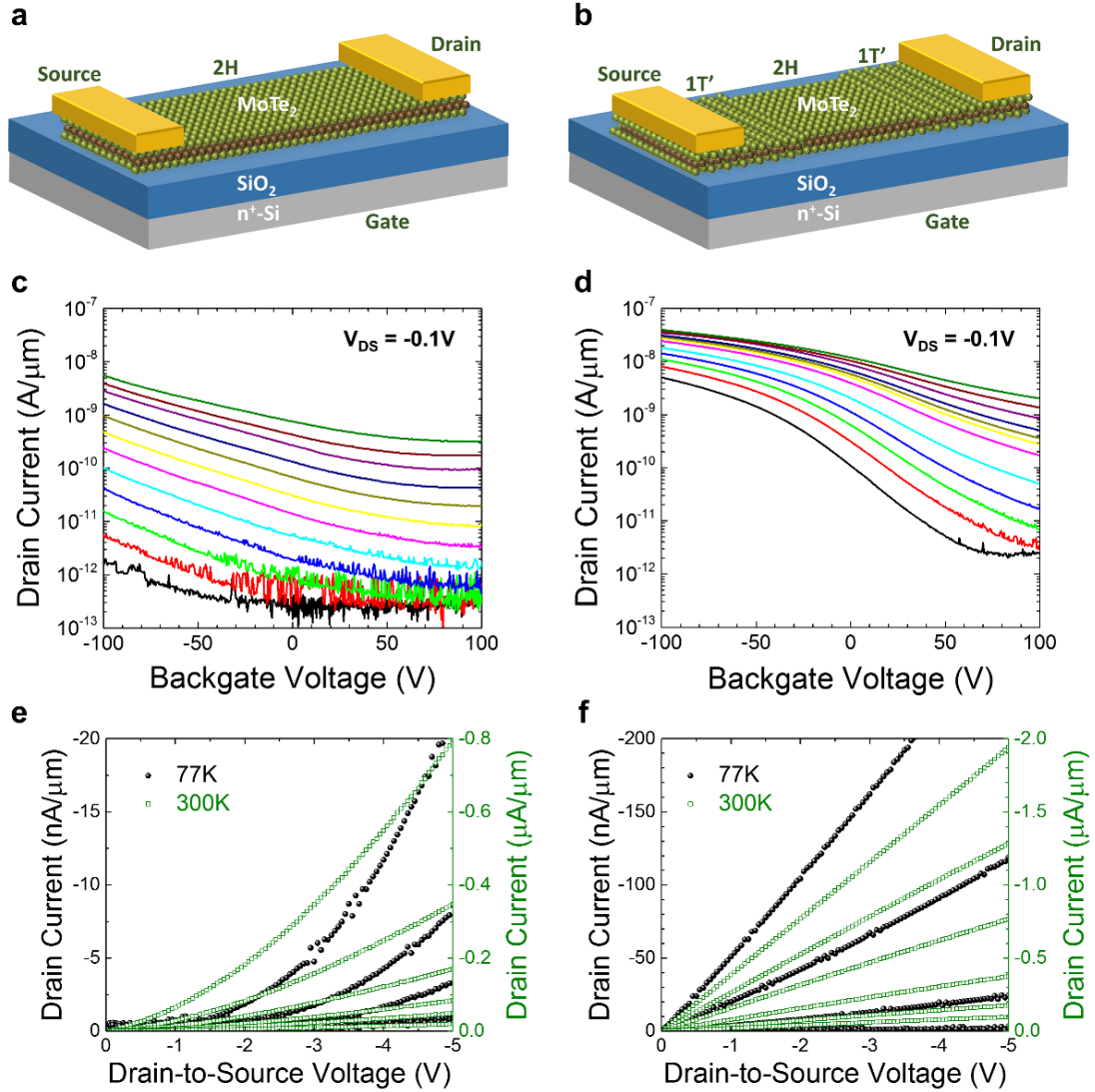


Figure 5.14. Temperature-dependent transport characteristics of 2H-only and 1T'-2H-1T' MoTe₂ devices. (a) and (b) are schematic diagrams of the 2H and 1T'-2H-1T' device structures, respectively. The 2H device dimensions are $L_{DS} = 3 \mu\text{m}$ and $W = 21 \mu\text{m}$, and the 1T'-2H-1T' device dimensions are $L_{DS} = 23 \mu\text{m}$ and $W = 9 \mu\text{m}$ (with $17 \mu\text{m}$ 2H region length). Transfer characteristics (I_D vs. V_{BG}) of the (c) 2H device and (d) 1T'-2H-1T' device at $V_{DS} = -0.1 \text{ V}$ for temperatures varying from 77 K (black curve) to 300 K (olive curve). Output characteristics (I_D vs. V_{DS}) of the (e) 2H and (f) 1T'-2H-1T' device for V_{BG} varying from -100 V (top curve) to $+100 \text{ V}$ (bottom curve) in steps of 40 V , acquired at $T = 77 \text{ K}$ (black points) and $T = 300 \text{ K}$ (olive points). This figure is reproduced with permission from Ma, et al. Manuscript in preparation.

The temperature-dependent device behavior for 2H-only and 1T'/2H/1T' device geometries (Figure 5.14) show that the on-current, current on/off ratio, and subthreshold swing (SS) are all improved by the use of 1T' electrodes. The on-current, current on/off ratio, and SS for the 1T'/2H/1T' device all increase with decreasing temperature, suggesting that the current of the 1T'/2H/1T' device is in the mobility-limited regime, as opposed to the thermionic-limited regime. Improvement of the current on/off ratio and SS is not strongly observed in the 2H-only device, indicating that the current is limited by thermionic transport associated with the metal/MoTe₂ interface in this case. Table 5.1 compares the performance of the 2H-only and 1T'/2H/1T' devices, and is reproduced with permission from Ma, et al. (manuscript in preparation). Each of the properties compared in Table 5.1 shows a significant improvement with the 1T'/2H/1T' devices. It is important to note that these devices have relatively high defect density, suggesting the need for further work to reduce the defects in the as-grown MoTe₂.

The hole mobility was extracted from the temperature-dependent transfer characteristics for 2H-only and 1T'/2H/1T' devices. The hole mobility at a given temperature and V_{DS} is extracted at the maximum transconductance, g_m , which is the maximum derivative of the I_D - V_{GS} curve. The hole mobility, μ , is then calculated by

$$\mu = \frac{g_m \cdot L}{W \cdot C_{ox} \cdot V_{DS}} \quad (4.1)$$

where L and W are the length and width of the device, respectively, C_{ox} is the gate dielectric capacitance, and V_{DS} is the drain-to-source voltage. The extracted hole mobility as a function of temperature for the 2H-only and the 1T'/2H/1T' devices are shown in Figure 5.15.

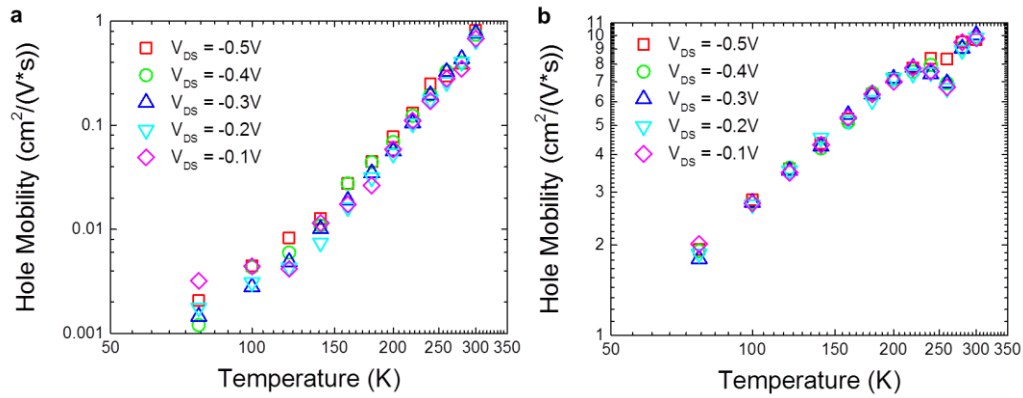


Figure 5.15. Hole mobility (log scale) as a function of temperature (log scale) for the (a) 2H-only device and the (b) 1T'/2H/1T' device in Figure 5.14 at different values of V_{DS} . This figure is reproduced with permission from Ma, et al. Manuscript in preparation.

The 1T'/2H/1T' device shows more than 10 times higher hole mobility than that of the 2H-only device, which is a logical result of the reduced contact resistances at the metal/1T' and 1T'/2H interfaces. The mobility is relatively low in both devices because of the high defect density in the as-grown MoTe₂. The 2H-only and 1T'/2H/1T' devices show a power-law mobility vs. temperature dependence, $\mu \propto T^x$, where $x = 5.9$ and $x = 1.3$, respectively. The slope of the 1T'/2H/1T' device is close to the typical factor of $x = 1.5$ for impurity scattering-dominant transport in the material due to the negligible effect of the contacts. This confirms the ohmic nature of the metal/1T' and 1T'/2H interfaces. Additionally, the dependence of V_{DS} on the hole mobility in the 1T'/2H/1T' device is less than that in the 2H-only device, again confirming ohmic contacts in the 1T'/2H/1T' device. For the 2H-only device, the contact resistance and sheet resistance are of the same order of magnitude, thus one would expect higher V_{DS} dependence.

Table 5.1. Comparison of 2H and 1T'-2H-1T' device performance.

Property	2H devices	1T'/2H/1T' devices	Ratio
On-current ($\text{nA}/\mu\text{m}$) (at 300K, $V_{\text{GS}} = -100\text{V}$, $V_{\text{DS}} = -0.1\text{V}$)	5.72	39.6	6.9
Transconductance ($\text{nS}/\mu\text{m}$) (at 300K, $V_{\text{DS}} = -0.1\text{V}$)	0.2	0.43	2.1
Mobility ($\text{cm}^2\text{V}^{-1}\text{s}^{-1}$) (at 300K, $V_{\text{DS}} = -0.1\text{V}$)	0.6-0.8	9-10	12-15
Current on/off ratio (at 77K, $V_{\text{DS}} = -0.1\text{V}$)	10	3.5×10^3	350

Improvement in the contact resistance when using the metal/1T' electrode design is also observed in the output characteristics (I_D vs. V_{DS}) of the devices shown in Figures 5.14e–f. The linear output characteristics of the 1T'/2H/1T' device at 300 and 77 K indicates ohmic behavior of the 1T' electrode and the 1T'/2H interface, whereas the output characteristics of the 2H device are nonlinear and become severe at low temperature, suggesting the presence of a Schottky barrier at the metal-2H interface.

Temperature-dependent transfer characteristics were used to extract Schottky barrier heights for three interfaces: (1) Metal/2H MoTe₂, (2) metal/1T' MoTe₂, and (3) 1T'/2H MoTe₂. The thermionic emission equation was used to model the temperature and bias dependence of I_D , expressed as

$$I_D = A^{**} T^{1.5} \exp \left[-\frac{1}{k_B T} (\Phi_{\text{SB}}) - \frac{qV_{\text{DS}}}{\eta} \right] \quad (4.2)$$

where A^{**} is the effective Richardson constant, T is the temperature, k_B is the Boltzmann constant, Φ_{SB} is the Schottky barrier height between the metal Fermi energy and the valence band edge of 2H MoTe₂, q is the electronic charge, V_{DS} is the drain-to-source voltage, and η is the ideality factor. The activation energy is denoted by $(\Phi_{\text{SB}} - qV_{\text{DS}}/\eta)$, and Φ_{SB} at each

gate voltage is extracted by the Arrhenius plot, $\ln(I_D/T^{1.5})$ vs. $1/k_B T$, at different values of V_{DS} .

The Arrhenius plots for a 1T'-only device at $V_{BG} = 0$ V (Figure 5.16a) show positive slope values, indicating a negative activation energy. This suggests that the conductivity of 1T' MoTe₂ decreases with increasing temperature, thereby implying that 1T' MoTe₂ is metallic or semi-metallic. The Arrhenius plots for a 2H-only device at $V_{BG} = -100$ V (Figure 5.16b) show negative slope values, indicating thermally-activated transport. Similar behavior was observed for all V_{BG} values used. Finally, the Arrhenius plots for a 1T'/2H/1T' device at $V_{BG} = -100$ V (Figure 5.16c) also show negative slope values, indicating thermally-activated transport. However, since no thermally-activated transport was observed for the metal/1T' interface, the energy barrier associated with transport in the 1T'/2H/1T' device must be associated with the 1T'/2H interface and not the metal/1T' interface.

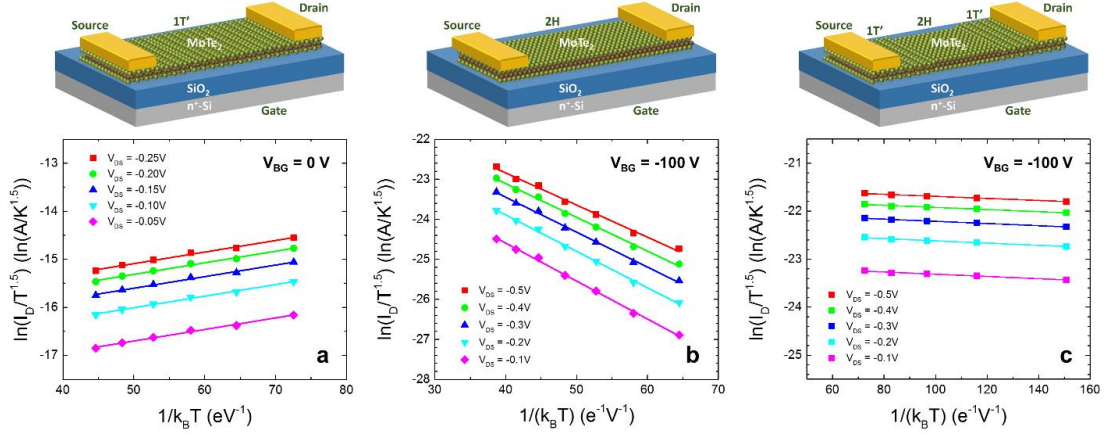


Figure 5.16. Arrhenius plots and bias-dependent effective barrier heights. (a) Arrhenius plots of $\ln(I_D/T^{1.5})$ vs. $1/k_B T$ for the 1T'-only device (depicted above the (a) panel) at $V_{BG} = 0$ V for different values of V_{DS} . The positive slopes here indicate the absence of an energy barrier at the metal/1T' interface. (b) Arrhenius plots for the 2H-only device at $V_{BG} = -100$ V for different values of V_{DS} . (c) Arrhenius plots for the 1T'/2H/1T' device at $V_{BG} = -100$ V for different values of V_{DS} . Given the absence of a barrier at the metal/1T' interface, the positive slope in (c) is an indication of the barrier height at the 1T'/2H interface. This figure is reproduced with permission from Ma, et al. Manuscript in preparation.

According to Equation 4.2, the Arrhenius curve slopes can be plotted as a function of V_{DS} and then extrapolated to $V_{DS} = 0$ V to extract the effective hole Schottky barrier height, Φ_{SB} . The slopes of the Arrhenius curves are $(qV_{DS}/\eta - \Phi_{SB})$, so the effective Schottky barrier height, Φ_{SB} , can be extracted by plotting the slopes vs. V_{DS} and then extrapolating to $V_{DS} = 0$ V. A representative plot of the extraction for a 2H-only device at a given V_{BG} is shown in Figure 5.17. Φ_{SB} is extracted for all values of V_{BG} . The results of this extrapolation for the 2H-only device and the 1T'/2H/1T' device (Figure 5.18) show that the overall barrier height for the 1T'/2H/1T' device is significantly lower than that of the 2H-only device over the entire range of V_{BG} .

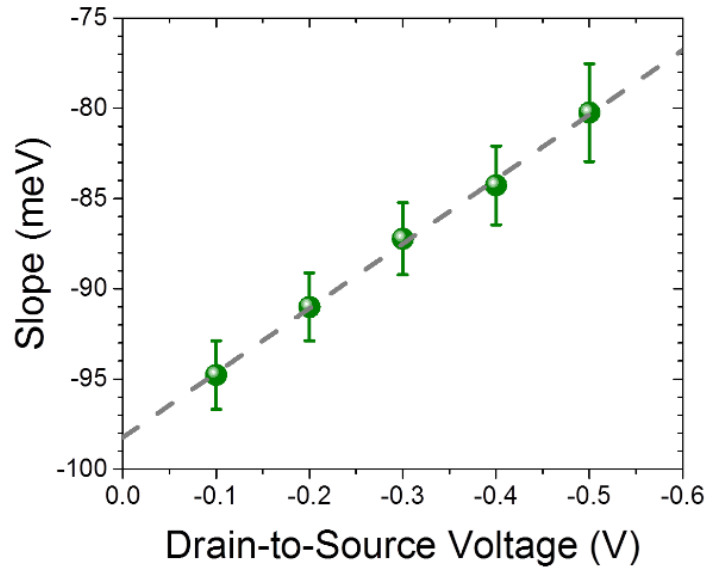


Figure 5.17. Plot of the slopes of the Arrhenius plot for the 2H-only device in Figure 5.14 vs. V_{DS} at $V_{BG} = -100$ V. This figure is reproduced with permission from Ma, et al. Manuscript in preparation.

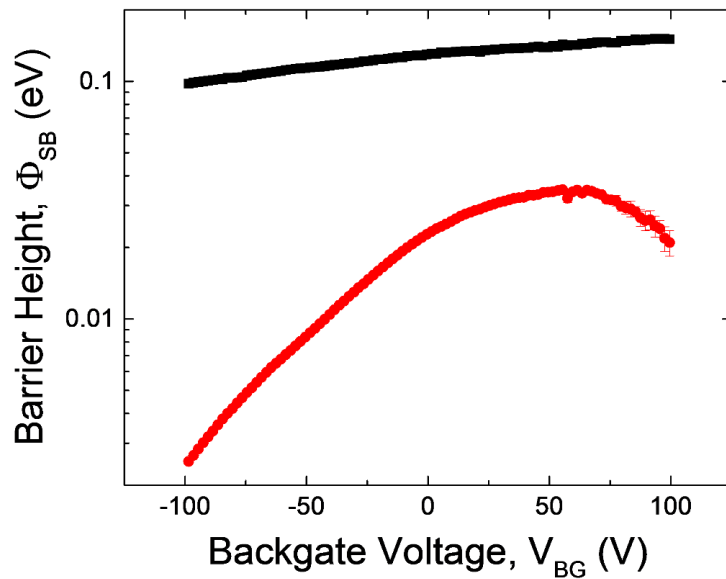


Figure 5.18. Effective Schottky barrier height of the 2H device (black curve) and the 1T'/2H/1T' device (red curve) as a function of V_{BG} . Error bars are extracted from the fitting shown in Figure 5.16. This figure is reproduced with permission from Ma, et al. Manuscript in preparation.

These results are qualitatively consistent with the Schottky barrier heights extracted for metal contacts to exfoliated 2H MoTe₂,^{185,186} and the 1T'/2H energy barrier is also consistent with that previously observed for exfoliated MoTe₂ with process-induced 1T' regions.¹⁶⁸ However, some discrepancy exists in the gate voltage dependence of the barrier height for the metal/2H contacts. In a previous report,¹⁸⁶ the effective barrier height was found to have a strong gate voltage dependence, with the barrier height increasing to 300 meV near the transistor off-state to near 0 V in the strong on-state region. Contrastingly, our work shows that the metal/2H barrier height has only a small gate voltage dependence, with similar behavior for the 1T'/2H barrier height. This behavior is likely due to the presence of defects in MoTe₂, which can lead to trap-assisted tunneling of carriers from the metal contacts into the MoTe₂.

We have also performed density functional theory (DFT) calculations of monolayer to five-layer 1T' and 2H MoTe₂ band structures to estimate the expected band alignments. Figure 5.19 shows the computed band structures of 5-layer 2H and 5-layer 1T' MoTe₂. Using PBE/GGA with spin-orbit coupling, the 5-layer 2H MoTe₂ is determined to be a semiconductor with an indirect band gap of 0.75 eV. This band gap is smaller than the experimentally determined value, but DFT has long been shown to underestimate the magnitude of band gaps. For the 5-layer 1T' MoTe₂, the band gap is closed and the CB minimum and VB maximum are overlapping. Because these CB and VB states are not completely separated, the 5-layer 1T' MoTe₂ is determined to be semi-metallic.

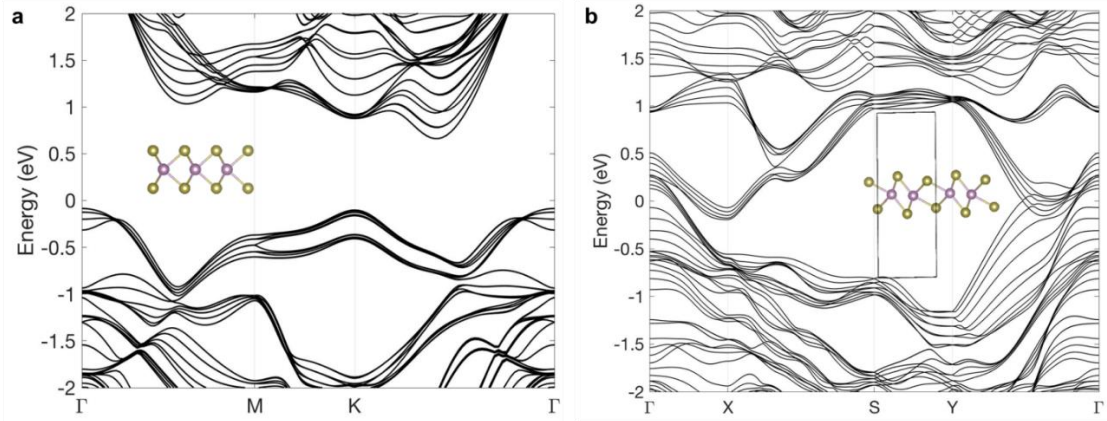


Figure 5.19. Calculated band structures of (a) 5-layer 2H MoTe₂, and (b) 5-layer 1T' MoTe₂, respectively, with spin-orbit coupling included. Inset are the crystallographic unit cells. This figure is reproduced with permission from Ma, et al. Manuscript in preparation.

DFT calculations confirm that 1T' and 2H MoTe₂ are metallic and semiconducting, respectively. DFT calculations also show that the Fermi level at the five-layer 1T'/2H boundary is within ~ 100 meV of the valence band edge, which is much closer than expected for Ti contacts to 2H MoTe₂.¹⁸⁷ We believe that the effect of trap-assisted transport in our samples makes it difficult to perform a truly quantitative comparison with experimental data.

The thickness dependent band gap determined by the difference between the CB minimum and VB maximum is shown in Figure 5.20a. The barrier heights (for holes) at the 2H/1T' interface were calculated using the Schottky-Mott model,¹⁸⁸ which assumes that the barrier for holes is the energy difference between the work function of the metal and the VB maximum of the semiconductor. The calculated barrier heights as a function of layer number are shown in Figure 5.20b.

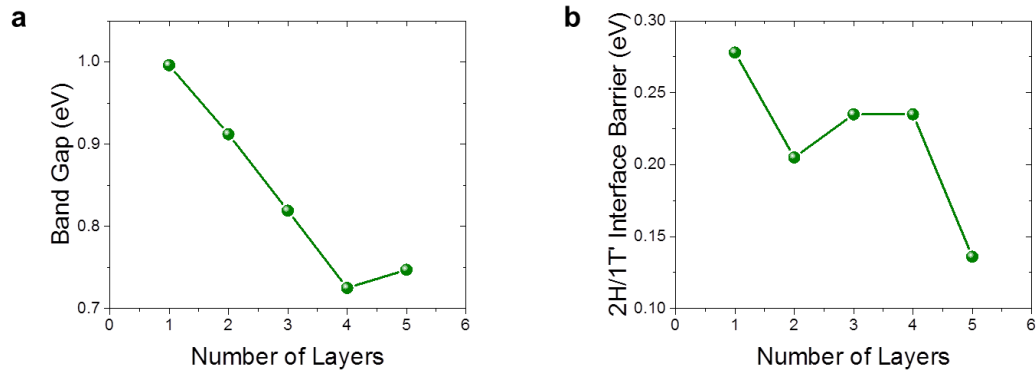


Figure 5.20. (a) Band gap of 2H MoTe₂ and (b) barrier height at the 2H/1T' interface as a function of layer number. This figure is reproduced with permission from Ma, et al. Manuscript in preparation.

The calculated barrier height for the 5-layer 2H-1T' interface is ~ 136 meV. This is much larger than the electrically determined value in Figure 5.18, but it has been previously demonstrated that the Schottky-Mott model is insufficient in predicting the barrier height of 2D lateral heterostructures.¹⁸⁹ Sophisticated models are needed to more accurately estimate the barrier heights, possibly including the construction a supercell that consists of both material phases. Another possible explanation for this barrier height discrepancy is that the interfacial traps in our devices may pin the Fermi level of 1T' MoTe₂ closer to the VB of 2H MoTe₂.

Finally, we note that the roll-off of the Schottky barrier for the 1T'/2H/1T' device in Figure 5.18 at positive gate voltages is unexpected, because the effective barrier height should continue to increase to at least half of the band gap before decreasing due to the onset of ambipolar transport.¹⁸⁵ Thus, additional experiments and simulations are needed to understand the role of traps and the electrostatic effects of the in-plane 1T'/2H heterostructures.

5.4.3 WS₂/NbS₂ Heterostructures

WS₂/NbS₂ lateral heterostructures grown via CVD can be seen in Figure 5.21. The as-grown WS₂ triangular flakes grown on bare *c*-cut sapphire are shown in the representative optical microscope image in Figure 5.21a and confirmed to be monolayer by PL spectroscopy (Figure 5.21b), showing strong PL peak intensity.⁹⁹ Subsequent NbS₂ growth on these samples results in the lateral heterostructures visible in the optical image in Figure 5.21c. Raman spectra (Figure 5.21d) confirm the presence of WS₂ and NbS₂ Raman modes over the respective regions of each material, with modes of both materials visible at the interface region.^{66,190–192} SEM images (Figure 5.21e) show the WS₂/NbS₂ lateral heterostructures with some NbS₂ nucleated on the center of the top of the WS₂. These SEM images show some charging at the edge of the WS₂ domains, partially due to the insulating sapphire substrate beneath the semiconducting WS₂ regions, accentuated by charge pooling at the interface between the WS₂ and metallic NbS₂. EDS data in these regions show the clear presence of elemental Nb and S in the NbS₂ film regions, but there is little to no W signal visible anywhere on the surface. This lack of W signal is easily explained by the monolayer nature of the WS₂ domains providing such a small sample volume that the generated signal is below the detection limit of the EDS detector.

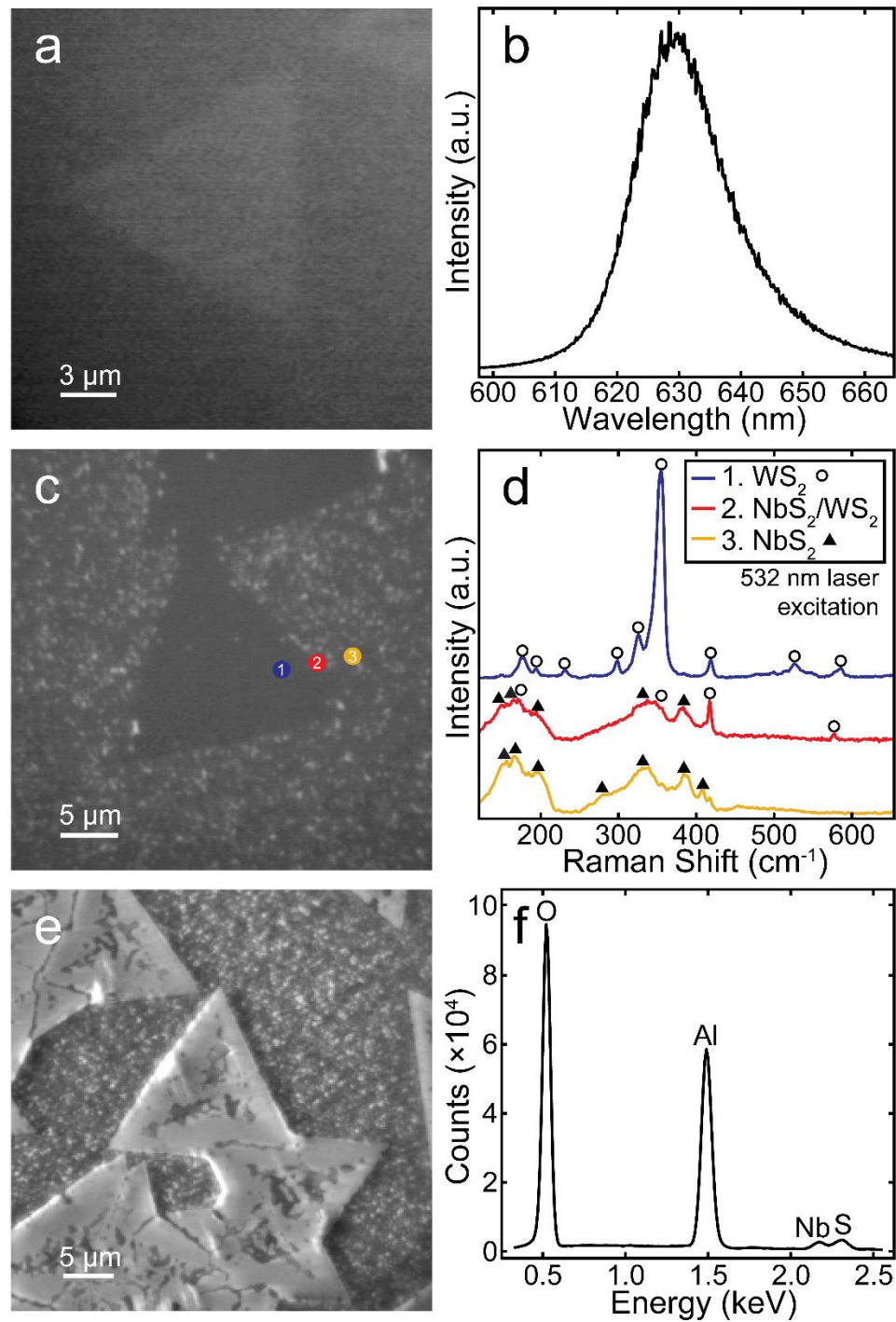


Figure 5.21. WS_2/NbS_2 lateral heterostructure characterization. (a) Representative optical image of ML WS_2 on sapphire, (b) PL spectrum of another representative ML WS_2 /sapphire sample, (c) optical image of WS_2/NbS_2 heterostructures, (d) Raman spectra corresponding to regions 1–3 in (c), (e) SEM image of WS_2/NbS_2 heterostructures, and (f) EDS spectrum over NbS_2 film region.

AFM analysis in Figure 5.22 provides a clear perspective of the interface morphology. The monolayer WS_2 flakes show smooth surfaces that undulate correspondingly with the underlying surface terraces in the sapphire substrate. The NbS_2 film on the other side of the interface is polycrystalline, with a ~ 1 nm height increase (relative to the WS_2 height), implying that the NbS_2 is few-layer at the WS_2/NbS_2 interface. The NbS_2 film thickness increases significantly with increasing distance from the interface. The maximum NbS_2 film thickness varies between samples but is typically ~ 50 – 100 nm, as shown in Figure 5.22b. The NbS_2 film shows a variety of triangular plateaus and etch pits on the surface, which are likely due to dislocations or defects generated during growth. As was discussed in Chapter 2, it is likely that the use of NbCl_5 precursor has unintended consequences on the NbS_2 film morphology. Vapor-phase chlorine or other chloride-containing byproducts of the NbCl_5 precursor are likely creating regions of local oxidation, which result in the formation of triangular etch pits in the NbS_2 film at high temperatures. While this morphology is not ideal, the film appears to be completely continuous, with all grains in seemingly good contact with nearby grains. Most importantly, the NbS_2 film appears to grow laterally from the edge of the WS_2 flake, with a seemingly abrupt junction between the NbS_2 and WS_2 regions.

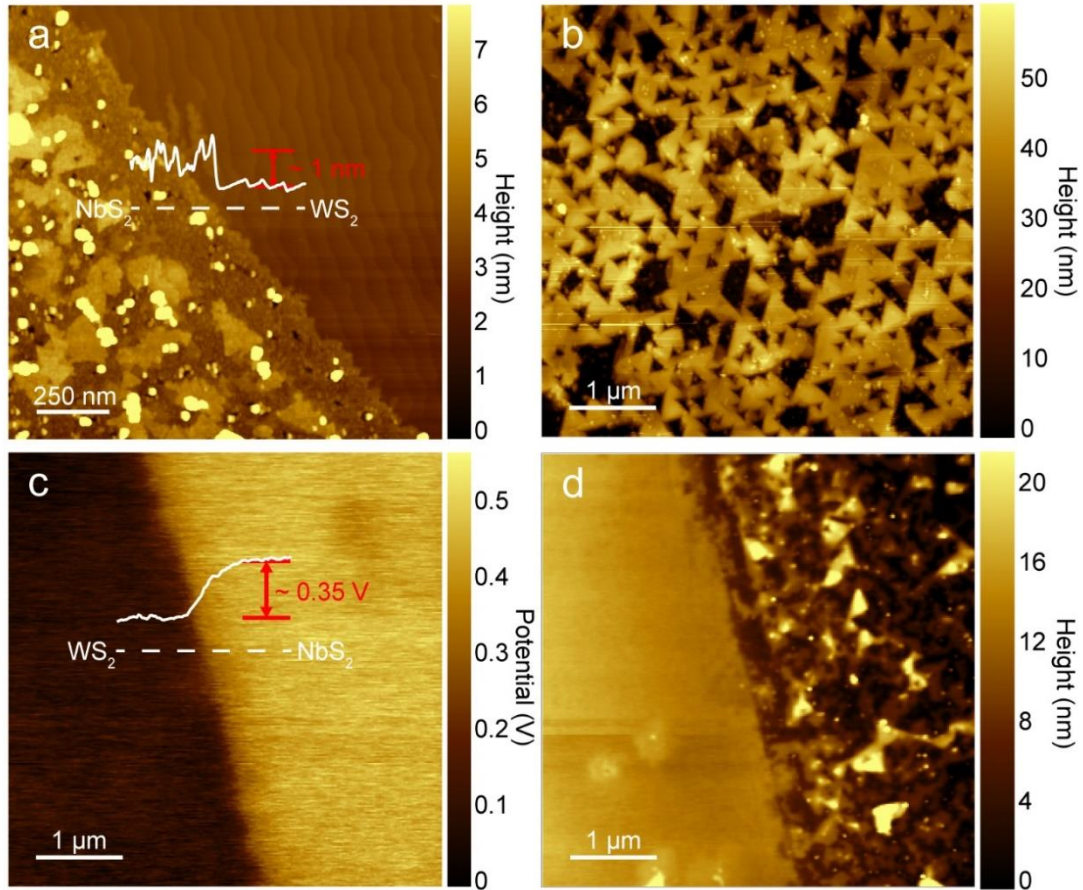


Figure 5.22. AFM and KPFM analysis of WS₂/NbS₂ heterostructures. (a) AFM of a WS₂/NbS₂ heterostructure interface and (b) AFM of a NbS₂-only film region. (c) KPFM potential image and (d) height image of a WS₂/NbS₂ heterostructure interface, acquired simultaneously.

To better characterize the electronic properties of the heterostructure, I performed KPFM across the interface. KPFM potential images show a ~ 0.35 V potential difference across the WS₂/NbS₂ interface. This potential difference is somewhat larger than the potential difference expected between the work function of NbS₂ and the valence band maximum of WS₂,¹⁹³ but this discrepancy is likely due to the insulating sapphire substrate. NbS₂ is expected to be metallic, but the geometry of the deposited film is such that it is not directly in contact with any other metals. Thus, the WS₂/NbS₂ heterostructures are not able

to be properly grounded during KPFM measurement without inducing permanent damaging to the sample through the use of carbon tape or a metallic epoxy.

Cross-section HRTEM analysis was performed on the WS_2/NbS_2 heterostructures to investigate the interfacial structure. A cross-sectional lamella of the sample was etched and lifted out of the substrate using a focused ion beam (FIB) setup. Figure 5.23 shows HRTEM analysis of this cross-sectional sample. The crystal lattice of the sapphire substrate is clearly visible (with lattice spacing of $\sim 5 \text{ \AA}$), upon which layers of the NbS_2 film are stacked with layer spacing of $\sim 6 \text{ \AA}$, consistent with the crystal structures of both materials. The inset in Figure 5.23a shows a convergent beam electron diffraction (CBED) pattern of the NbS_2 film region, which shows the rhombohedral, A-B-C stacking order expected for 3R NbS_2 , thereby confirming the NbS_2 film is the 3R phase. In other regions of the cross-section sample, the WS_2 monolayer crystal is visible, indicated by the sub-nanometer film of dark contrast above the sapphire substrate. EDS data acquired from each of these regions confirms the presence of NbS_2 and WS_2 , respectively. However, it is difficult to ascertain any information about the interfacial bonding and structure of these heterostructures from these HRTEM images, because the lateral NbS_2/WS_2 interface was not clearly resolvable. The inability to resolve the lateral NbS_2/WS_2 interface is likely due to the difficulty in etching and thinning the cross-sectional lamella via FIB. The hard, insulating nature of sapphire makes this process slow and prone to charging-induced error.

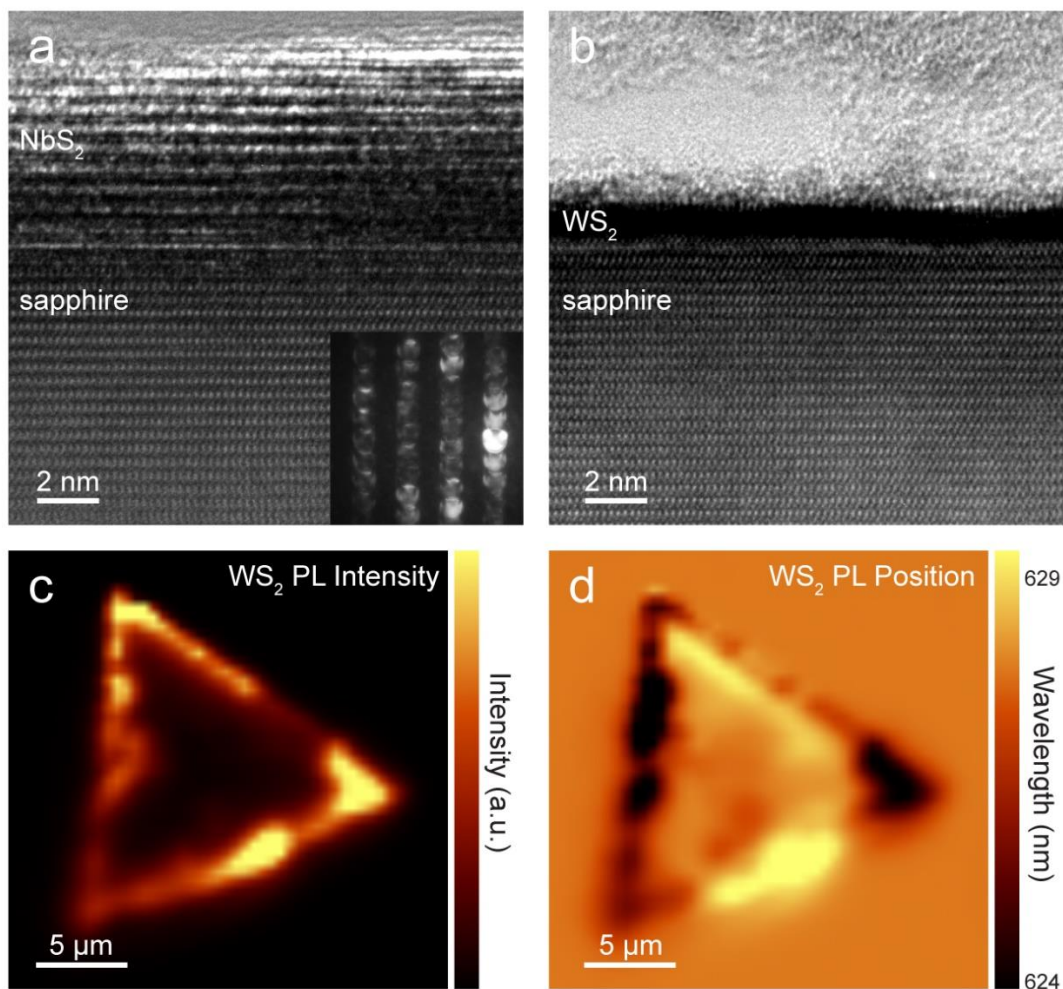


Figure 5.23. Cross-section TEM and PL mapping analysis of the WS_2/NbS_2 interface. Cross-section TEM image of the (a) $\text{NbS}_2/\text{sapphire}$ interface and (b) $\text{WS}_2/\text{sapphire}$ interface. Inset in (a) is a CBED pattern of NbS_2 film. Map of WS_2 PL (c) intensity and (d) position observed in a WS_2/NbS_2 heterostructure on sapphire.

To better understand the nature of the WS_2/NbS_2 interface, I acquired PL maps of the WS_2/NbS_2 heterostructures on sapphire (Figure 5.23c–d). Photoluminescence is sensitive to a variety of factors, including external electrostatic doping, strain, and structural defects, thus PL mapping can help us better understand the interfacial structure.¹⁹⁴ The PL intensity map of the WS_2/NbS_2 heterostructures in Figure 5.23c–d

shows that there is significantly increased PL intensity at the edge of the ML WS₂ flakes that directly borders the NbS₂ film. This locally increased PL intensity at the WS₂ edge also corresponds with a general decrease in the PL peak position. It has been previously shown that the PL peak wavelength can blueshift when the material has a higher concentration of *n*-dopants.^{194–196} In the case of WS₂/NbS₂ heterostructures, the increased intensity and blue-shifting of the PL at the WS₂ edges is likely due to *n*-doping caused by structural defects (such as S vacancies or Nb inclusions) localized at the edges of the WS₂ flakes.

The goal of this work is to use metallic few-layer NbS₂ as a lateral contact to the semiconducting WS₂ monolayers. The preliminary characteristics of NbS₂-only, NbS₂/WS₂, and WS₂-only devices are shown in Figure 5.24. Output characteristics of a representative NbS₂-only device with no applied gate voltage show relatively large current with applied drain-to-source voltage (V_{DS}), especially compared to that of WS₂/NbS₂ and WS₂-only devices (Figure 5.24b–c). Some non-linearity is present in the NbS₂ output characteristics, which could be an indicator of semi-metallic character in the NbS₂. However, transfer characteristics of the NbS₂-only device (Figure 5.24d) show no gate dependence in the drain current at a varying V_{DS} , which indicates that the NbS₂ channel is metallic.

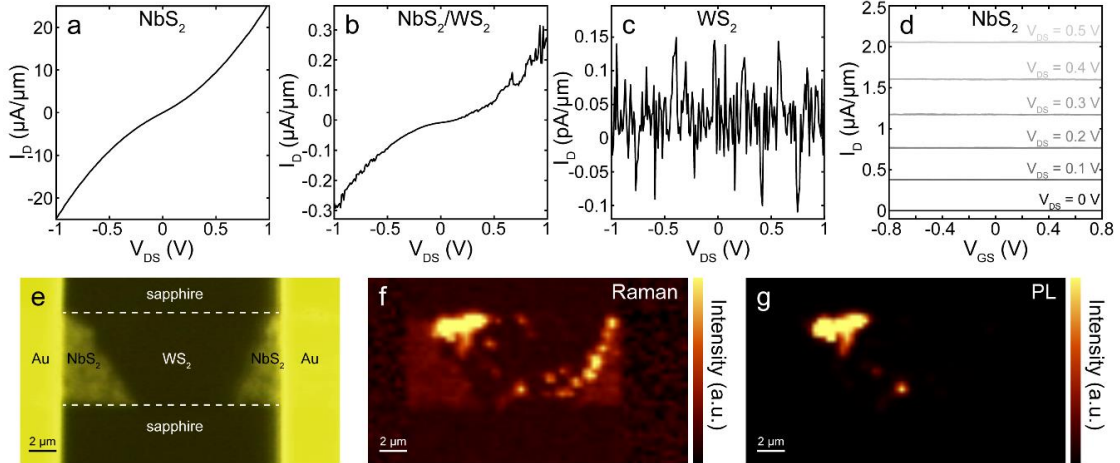


Figure 5.24. Preliminary device characteristics and investigation of WS_2/NbS_2 heterostructure devices via Raman and PL mapping. Output characteristics (drain current vs. drain-to-source voltage) of representative (a) NbS_2 -only, (b) WS_2/NbS_2 , and (c) WS_2 -only devices with no applied gate voltage. (d) Transfer characteristics (drain current vs. gate-to-source voltage) of a NbS_2 -only device at varying drain-to-source voltages, showing no gate dependence. (e) Optical microscope image of a representative WS_2/NbS_2 heterostructure device. (f) WS_2 Raman and (g) PL maps of device in (e), showing degradation in the channel.

It was observed that the e-beam resist was under-dosed during device fabrication, resulting in resist residuals that are visibly present for WS_2/NbS_2 , NbS_2 -only, and WS_2 -only devices (all devices shown in Figure 5.24). The presence of these residuals is a more likely explanation of the non-linearity present in the NbS_2 output characteristics than semi-metallic character. Output characteristics of the WS_2/NbS_2 heterostructure device show two orders of magnitude less current than the NbS_2 -only device, which can be due to e-beam resist residuals and damage to the channel during device fabrication, which I will discuss in more detail in the following paragraph. Output characteristics of the WS_2 -only device show no distinguishable current, which can be due to e-beam resist residuals, channel damage, or van der Waals tunneling barriers formed between the Ti/Au leads and the WS_2 , as discussed in Section 5.2.2.

The particularly low drain currents for the WS₂/NbS₂ and WS₂-only devices prompted an investigation into the integrity of the materials in these devices. After removing the ion-gel top gates, all devices appear to show significant damage to the channel region, as indicated in WS₂ Raman and PL maps (Figure 5.24f–g). A significant portion of the channel region in these devices do not show the indicative WS₂ Raman or PL peaks that were present before device fabrication. This damage is likely induced by the choice of ion gel top gate or long solvent soaking times for resist removal during device fabrication. In future devices, gentler device fabrication procedures will be used. It is also worth noting that the WS₂ Raman map was generated by integrating the Raman intensity over a small relative wavenumber range around the WS₂ 2LA(M) mode near 352 cm⁻¹.¹⁹⁰ However, this range overlaps with Raman modes for NbS₂, hence we can see moderate Raman intensity over the NbS₂ regions in Figure 5.24f.⁶⁷

5.5 Conclusions and Future Work

The work with in-plane, few-layer, 2H-1T' MoTe₂ homojunctions demonstrates that flux-controlled tellurization of Mo nanoislands can be used to grow phase-specific few-layer MoTe₂ films. This is the first time few-layer in-plane 2H-1T' MoTe₂ homojunctions have been synthesized at optimum Te flux conditions. With low Te flux, few-layer 1T' MoTe₂ is obtained, whereas few-layer 2H MoTe₂ is formed with high Te flux. With exceedingly low Te flux, defective 1T' MoTe₂ can be grown. Raman mapping and KPFM confirm that the junctions of the in-plane 2H-1T' MoTe₂ homojunctions have a sharp interface possessing a potential difference of 100 meV between the two domains. Furthermore, the phase-selective MoTe₂ synthesis has been shown to be useful for the

fabrication of patterned few-layer 2H-1T' MoTe₂ junctions. This flux-controlled synthetic approach allows for the possibility of large-scale direct fabrication of patterned edge-contact 2D material devices.

With the few-layer 2H-1T' MoTe₂ device fabrication, we have shown that 2H MoTe₂ devices are significantly improved with the use of metallic 1T' contacts. This improvement is a result of the reduced contact resistance and small barrier height at the 2H/1T' interface. This technique for creating 1T'-contacted MoTe₂ FETs can be expanded to the phase-selective synthetic strategy demonstrated above, in which 2H MoTe₂ is initially grown and patterned and 1T' MoTe₂ is subsequently grown around the 2H channels. 2H-1T' MoTe₂ homojunctions show promise for realizing phase-change memory and logic devices.

The successful two-step CVD growth of lateral WS₂/NbS₂ heterostructures is also demonstrated here. We have investigated the nature of the interface between these two materials, and subsequently patterned the heterostructures into a FET device geometry to assess the heterostructure's electrical performance. Due to device fabrication limitations related to sample degradation and resist under-exposure, the true electronic properties of these WS₂/NbS₂ heterostructures have yet to be determined. Future work in sample patterning and device fabrication seeks to minimize sample damage and eliminate any other deleterious effects that may conceal the electronic properties of the materials. We also intend to extract the contact resistance quantitatively by performing transfer length measurements on NbS₂ films. If NbS₂ is going to succeed as a 2D lateral contact for semiconducting TMDCs, the NbS₂ films must show high electrical conductivity throughout the entirety of the film. Furthermore, there must be little to no contact resistance

at the interface between the NbS₂ and WS₂. Future tests seek to investigate these properties of the WS₂/NbS₂ devices.

Assuming NbS₂ continues to show promise as a metallic 2D contact material, we wish to use this framework for additional experiments. Many semiconducting 2D TMDCs show promise for future electronics, and each TMDC possess a unique band gap. The magnitude of a given band gap and the energetic position of the CB minimum and VB maximum are all important parameters to consider. When considering an interface with a metal, the position of these bands relative to the work function of the metal is also quite important, because these relative positions dictate whether ohmic contact or a Schottky barrier is present at the interface. In the example of WS₂/NbS₂ heterostructures, there is expected to be a relatively small Schottky barrier between the n-type WS₂ and metallic NbS₂.^{68,193} However, in the case of WSe₂, a p-type semiconducting TMDC, there is expected to be a small but *negative* Schottky barrier, indicative of spontaneous charge transfer between the NbS₂ and WSe₂. Given this and the work I have performed to grow monolayer WSe₂ films via CVD, we intend to grow lateral WSe₂/NbS₂ heterostructures and assess the electronic properties of fabricated devices. Similar to the CVD growth of NbS₂ films described above, WSe₂/NbS₂ heterostructures will be grown using ML WSe₂ as a seed crystal for the lateral growth of NbS₂ using the chloride-based CVD growth procedure. These WSe₂/NbS₂ heterostructures will then be patterned into devices and their characteristics will be assessed. These heterostructures have the potential to greatly impact the future of 2D material devices.

Chapter 6

Conclusions

The work I present here demonstrates the exhaustive investigation into the CVD growth of a variety of promising 2D TMDCs, including MoS₂, WS₂, MoTe₂, NbS₂, and WSe₂. With these results, I have demonstrated synthetic control over the growth of these materials. I have grown 2D TMDC crystals and films with variable thickness, phase, and morphology. I have been able to reproducibly synthesize the growth of monolayer crystals of MoS₂, WS₂, and WSe₂, as well as the few-layer film growths of 2H MoTe₂, 1T' MoTe₂, and NbS₂. I have demonstrated that the various aspects of these materials can be controlled through the systematic optimization of many synthetic parameters, including substrate choice, substrate preparation, precursor choice, precursor temperature, substrate temperature, precursor timing, reaction time, and post-growth conditioning.

With the substrate modifications I have performed, I have shown that surface reconstruction and modification can have a direct result on the subsequent CVD growth of 2D TMDCs. ML MoS₂ growth on SiO₂/Si is randomly oriented, whereas ML MoS₂ growth on *c*-cut sapphire is aligned to the sapphire surface terraces. Annealed sapphire substrates show a great deal of step flow after ambient annealing at high temperature, but despite these smooth surfaces, subsequently MoS₂ growth is confined to the step edges, and thus grows in irregular, truncated flakes along surface terrace edges. These experiments demonstrate the feasibility of using surface preparation methods to control the CVD growth of TMDCs. The effects demonstrated here of the substrate on the CVD growth of TMDCs should be considered in future TMDC growths.

I have shown that controlled growth of 2D TMDCs allows for the creation of many novel 2D semiconductor-semiconductor and metal-semiconductor heterostructures. Specifically, I have demonstrated the synthesis of vertical and lateral MoS₂/WS₂

heterostructures, freestanding MoO₂/MoS₂ core/shell plates, in-plane 2H-1T' MoTe₂ few-layer films, and lateral heterostructures between ML WS₂ and few-layer NbS₂.

With the growth of lateral and vertical MoS₂/WS₂ heterostructures, it is demonstrated that the lateral or vertical nature of alignment can be directly controlled by the cleanliness of the MoS₂ 2D seed. When hydrogen is included in the carrier gas stream, sharp and clean MoS₂ crystals are synthesized, and these can be used for the lateral heteroepitaxial growth of WS₂. When hydrogen is excluded from the carrier gas stream, MoS₂ crystals with particles along the edges are synthesized, and subsequent growth of WS₂ results in vertical heterostructures due to additional nucleation on the MoS₂ surface due to the presence of additional particles. This synthetic dichotomy can be used in future work to select for lateral and vertical heteroepitaxy between a variety of 2D TMDCs.

I have demonstrated the novel growth of epitaxially grown, freestanding MoO₂/MoS₂ core/shell nanoplates on 4H-SiC. These core/shell nanoplates are grown using a minor synthetic modification of ML MoS₂ growth. Specifically, this is achieved by the delaying of chalcogen precursor during the growth, which allows for the MoO_{3-x} precursor to nucleate and grow into freestanding, epitaxial plates on the 4H-SiC surface, subsequently sulfurizing to form MoS₂ shells. This procedure is demonstrated to be generalizable to MoO₂/MoTe₂ core/shell nanoplates, and it can likely be extended to other TMDC systems. These materials show promise for catalytic applications that require TMDC active sites and high-density, epitaxial, freestanding nanoplate geometries.

The in-plane 2H-1T' MoTe₂ few-layer homojunctions and WS₂/NbS₂ lateral heterostructures are shown to be patternable, and electronic devices have been fabricated to assess their characteristics. In-plane 2H-1T' MoTe₂ few-layer homojunction devices

show significant improvement over 2H MoTe₂ devices made with noble metal contacts, demonstrating reduced contact resistance and Schottky barrier height. This improved functionality is achieved by the reduced potential difference between the 2H and 1T' MoTe₂ and the metallic nature of the 1T' MoTe₂. The improved functionality of 1T'-2H-1T' MoTe₂ devices also bolsters the underlying premise of using metallic TMDCs as contacts with reduced contact resistance.

The WS₂/NbS₂ lateral heterostructures shown here are the first ever report of lateral heterostructures between these materials, and it is demonstrated that the growth of NbS₂ is limited to growing around the edge of ML WS₂ crystals. Problems with the fabrication of WS₂/NbS₂ lateral heterostructure devices obscure the electronic properties of these devices, but the properties of these devices will be determined in future work. This system will also be extended to make metallic NbS₂ contacts to other semiconducting TMDCs. WSe₂/NbS₂ heterostructures will be grown using ML WSe₂ as a seed crystal for the lateral CVD growth of NbS₂ via the chloride-based CVD growth procedure. These WSe₂/NbS₂ heterostructures will then be patterned into devices and their characteristics will be assessed. In-plane 2H-1T' MoTe₂ few-layer homojunctions and WS₂/NbS₂ lateral heterostructures show promise for future 2D TMDC devices by the reduction or elimination of the Schottky barrier induced with noble metal contacts.

Analysis of the TMDCs and related heterostructures grown here indicates that they are high-quality and can be reproducibly grown when considering the synthetic parameters described above. These CVD-grown TMDCs and heterostructures show promise for a variety of applications, including catalysis, nanoelectronics, optoelectronics, and valleytronics. There is much future work that has yet to be done in the context of showing

these heterostructures' utility in the various applications for which they show promise. It is my hope that this presentation of data bolsters support for future use of these materials in applications and industry.

References

- (1) Novoselov, K. S.; Geim, A. K.; Morozov, S. V.; Jiang, D.; Zhang, Y.; Dubonos, S. V.; Grigorieva, I. V.; Firsov, A. A. Electric Field Effect in Atomically Thin Carbon Films. *Science* **2004**, *306* (5696), 666–669.
- (2) Butler, S. Z.; Hollen, S. M.; Cao, L.; Cui, Y.; Gupta, J. A.; Gutiérrez, H. R.; Heinz, T. F.; Hong, S. S.; Huang, J.; Ismach, A. F.; et al. Progress, Challenges, and Opportunities in Two-Dimensional Materials Beyond Graphene. *ACS Nano* **2013**, *7* (4), 2898–2926.
- (3) Kuc, A.; Zibouche, N.; Heine, T. Influence of Quantum Confinement on the Electronic Structure of the Transition Metal Sulfide TS_2 . *Phys. Rev. B* **2011**, *83* (24), 245213.
- (4) Wang, Q. H.; Kalantar-Zadeh, K.; Kis, A.; Coleman, J. N.; Strano, M. S. Electronics and Optoelectronics of Two-Dimensional Transition Metal Dichalcogenides. *Nat. Nanotechnol.* **2012**, *7* (11), 699–712.
- (5) Ganatra, R.; Zhang, Q. Few-Layer MoS_2 : A Promising Layered Semiconductor. *ACS Nano* **2014**, *8* (5), 4074–4099.
- (6) Rapoport, L.; Bilik, Y.; Feldman, Y.; Homyonfer, M.; Cohen, S. R.; Tenne, R. Hollow Nanoparticles of WS_2 as Potential Solid-State Lubricants. *Nature* **1997**, *387* (6635), 791–793.
- (7) Hu, K. H.; Wang, J.; Schraube, S.; Xu, Y. F.; Hu, X. G.; Stengler, R. Tribological Properties of MoS_2 Nano-Balls as Filler in Polyoxymethylene-Based Composite Layer of Three-Layer Self-Lubrication Bearing Materials. *Wear* **2009**, *266* (11–12), 1198–1207.
- (8) Topsøe, H.; Clausen, B. S.; Massoth, F. E. *Hydrotreating Catalysis*; Springer New York: Berlin, 1996; Vol. 11.
- (9) McBride, K. L.; Head, J. D. DFT Investigation of MoS_2 Nanoclusters Used as Desulfurization Catalysts. *Int. J. Quantum Chem.* **2009**, *109* (15), 3570–3582.
- (10) Sørensen, S. G.; Füchtbauer, H. G.; Tuxen, A. K.; Walton, A. S.; Lauritsen, J. V. Structure and Electronic Properties of In Situ Synthesized Single-Layer MoS_2 on a Gold Surface. *ACS Nano* **2014**, *8* (7), 6788–6796.
- (11) Xia, F.; Mueller, T.; Lin, Y.-M.; Valdes-Garcia, A.; Avouris, P. Ultrafast Graphene Photodetector. *Nat. Nanotechnol.* **2009**, *4* (12), 839–843.
- (12) Lopez-Sanchez, O.; Lembke, D.; Kayci, M.; Radenovic, A.; Kis, A. Ultrasensitive Photodetectors Based on Monolayer MoS_2 . *Nat. Nanotechnol.* **2013**, *8* (7), 497–501.
- (13) Zhang, W.; Chuu, C.-P.; Huang, J.-K.; Chen, C.-H.; Tsai, M.-L.; Chang, Y.-H.; Liang, C.-T.; Chen, Y.-Z.; Chueh, Y.-L.; He, J.-H.; et al. Ultrahigh-Gain Photodetectors Based on Atomically Thin Graphene- MoS_2 Heterostructures. *Sci. Rep.* **2015**, *4* (1), 3826.

- (14) Yu, S. H.; Lee, Y.; Jang, S. K.; Kang, J.; Jeon, J.; Lee, C.; Lee, J. Y.; Kim, H.; Hwang, E.; Lee, S.; et al. Dye-Sensitized MoS₂ Photodetector with Enhanced Spectral Photoresponse. *ACS Nano* **2014**, *8* (8), 8285–8291.
- (15) Hu, P.; Wang, L.; Yoon, M.; Zhang, J.; Feng, W.; Wang, X.; Wen, Z.; Idrobo, J. C.; Miyamoto, Y.; Geoegean, D. B.; et al. Highly Responsive Ultrathin GaS Nanosheet Photodetectors on Rigid and Flexible Substrates. *Nano Lett.* **2013**, *13* (4), 1649–1654.
- (16) Calandra, M. Chemically Exfoliated Single-Layer MoS₂: Stability, Lattice Dynamics, and Catalytic Adsorption from First Principles. *Phys. Rev. B* **2013**, *88* (24), 245428.
- (17) Ataca, C.; Şahin, H.; Ciraci, S. Stable, Single-Layer MX₂ Transition-Metal Oxides and Dichalcogenides in a Honeycomb-Like Structure. *J. Phys. Chem. C* **2012**, *116* (16), 8983–8999.
- (18) Toh, R. J.; Sofer, Z.; Luxa, J.; Sedmidubský, D.; Pumera, M. 3R Phase of MoS₂ and WS₂ Outperforms the Corresponding 2H Phase for Hydrogen Evolution. *Chem. Commun.* **2017**, *53* (21), 3054–3057.
- (19) Böker, T.; Severin, R.; Müller, A.; Janowitz, C.; Manzke, R.; Voß, D.; Krüger, P.; Mazur, A.; Pollmann, J. Band Structure of MoS₂, MoSe₂, and α -MoTe₂: Angle-Resolved Photoelectron Spectroscopy and Ab Initio Calculations. *Phys. Rev. B* **2001**, *64* (23), 235305.
- (20) Radisavljevic, B.; Radenovic, A.; Brivio, J.; Giacometti, V.; Kis, A. Single-Layer MoS₂ Transistors. *Nat. Nanotechnol.* **2011**, *6* (3), 147–150.
- (21) Mak, K. F.; Lee, C.; Hone, J.; Shan, J.; Heinz, T. F. Atomically Thin MoS₂: A New Direct-Gap Semiconductor. *Phys. Rev. Lett.* **2010**, *105* (13), 136805.
- (22) Molina-Sánchez, A.; Wirtz, L. Phonons in Single-Layer and Few-Layer MoS₂ and WS₂. *Phys. Rev. B* **2011**, *84* (15), 155413.
- (23) Sahoo, S.; Gaur, A. P. S.; Ahmadi, M.; Guinel, M. J.-F.; Katiyar, R. S. Temperature-Dependent Raman Studies and Thermal Conductivity of Few-Layer MoS₂. *J. Phys. Chem. C* **2013**, *117* (17), 9042–9047.
- (24) Kaasbjerg, K.; Thygesen, K. S.; Jacobsen, K. W. Phonon-Limited Mobility in n-Type Single-Layer MoS₂ from First Principles. *Phys. Rev. B* **2012**, *85* (11), 115317.
- (25) Zhu, Z. Y.; Cheng, Y. C.; Schwingenschlögl, U. Giant Spin-Orbit-Induced Spin Splitting in Two-Dimensional Transition-Metal Dichalcogenide Semiconductors. *Phys. Rev. B* **2011**, *84* (15), 153402.
- (26) Ye, Y.; Xiao, J.; Wang, H.; Ye, Z.; Zhu, H.; Zhao, M.; Wang, Y.; Zhao, J.; Yin, X.; Zhang, X. Electrical Generation and Control of the Valley Carriers in a Monolayer Transition Metal Dichalcogenide. *Nat. Nanotechnol.* **2016**, No. April, 1–6.
- (27) Benameur, M. M.; Radisavljevic, B.; Héron, J. S.; Sahoo, S.; Berger, H.; Kis, A. Visibility of Dichalcogenide Nanolayers. *Nanotechnology* **2011**, *22* (12), 125706.

- (28) Zhou, W.; Zou, X.; Najmaei, S.; Liu, Z.; Shi, Y.; Kong, J.; Lou, J.; Ajayan, P. M.; Yakobson, B. I.; Idrobo, J.-C. Intrinsic Structural Defects in Monolayer Molybdenum Disulfide. *Nano Lett.* **2013**, *13* (6), 2615–2622.
- (29) Jain, A.; Bharadwaj, P.; Heeg, S.; Parzefall, M.; Taniguchi, T.; Watanabe, K.; Novotny, L. Minimizing Residues and Strain in 2D Materials Transferred from PDMS. *Nanotechnology* **2018**, *29* (26), 265203.
- (30) Joensen, P.; Frindt, R. F.; Morrison, S. R. Single-Layer MoS₂. *Mater. Res. Bull.* **1986**, *21* (4), 457–461.
- (31) Coleman, J. N.; Lotya, M.; O'Neill, A.; Bergin, S. D.; King, P. J.; Khan, U.; Young, K.; Gaucher, A.; De, S.; Smith, R. J.; et al. Two-Dimensional Nanosheets Produced by Liquid Exfoliation of Layered Materials. *Science* **2011**, *331* (6017), 568–571.
- (32) Zeng, Z.; Yin, Z.; Huang, X.; Li, H.; He, Q.; Lu, G.; Boey, F.; Zhang, H. Single-Layer Semiconducting Nanosheets: High-Yield Preparation and Device Fabrication. *Angew. Chemie Int. Ed.* **2011**, *50* (47), 11093–11097.
- (33) Chhowalla, M.; Shin, H. S.; Eda, G.; Li, L.-J.; Loh, K. P.; Zhang, H. The Chemistry of Two-Dimensional Layered Transition Metal Dichalcogenide Nanosheets. *Nat. Chem.* **2013**, *5* (4), 263–275.
- (34) Pierson, H. O. *Handbook of Chemical Vapor Deposition: Principles, Technology and Applications*; Noyes Publications: Norwich, New York, U.S.A, 1999.
- (35) Dobkin, D.; Zuraw, M. K. *Principles of Chemical Vapor Deposition*; Springer Science, 2003.
- (36) Lee, Y.-H.; Zhang, X.-Q.; Zhang, W.; Chang, M.-T.; Lin, C.-T.; Chang, K.-D.; Yu, Y.-C.; Wang, J. T.-W.; Chang, C.-S.; Li, L.-J.; et al. Synthesis of Large-Area MoS₂ Atomic Layers with Chemical Vapor Deposition. *Adv. Mater.* **2012**, *24* (17), 2320–2325.
- (37) Atkins, P.; de Paula, J. *Physical Chemistry*, 9th ed.; W. H. Freeman, 2009.
- (38) Callister, Jr., W. D.; Rethwisch, D. G. *Materials Science and Engineering: An Introduction*; John Wiley and Sons, 2009.
- (39) Ishizaka, A.; Murata, Y. Crystal Growth Model for Molecular Beam Epitaxy: Role of Kinks on Crystal Growth. *J. Phys. Condens. Matter* **1994**, *6* (45), L693–L698.
- (40) Venables, J. A. *Introduction to Surface and Thin Film Processes*; Cambridge University Press, 2000.
- (41) Oura, K.; Lifshits, V. G.; Saranin, A. A.; Zotov, A. V.; Katayama, M. *Surface Science: An Introduction*; Springer-Verlag, 2003.
- (42) Venables, J. A. Atomic Processes in Crystal Growth. *Surf. Sci.* **1994**, *299–300*, 798–817.
- (43) Ohring, M. *Materials Science of Thin Films*, 2nd ed.; 2001.

- (44) Floro, J. A.; Chason, E.; Cammarata, R. C.; Srolovitz, D. J. Physical Origins of Intrinsic Stresses in Volmer–Weber Thin Films. *MRS Bull.* **2002**, 27 (01), 19–25.
- (45) Eaglesham, D. J.; Cerullo, M. Dislocation-Free Stranski-Krastanow Growth of Ge on Si(100). *Phys. Rev. Lett.* **1990**, 64 (16), 1943–1946.
- (46) Somorjai, G. A. *Introduction to Surface Chemistry and Catalysis*, 2nd ed.; John Wiley & Sons Inc., 2010.
- (47) Kolasinski, K. W. *Surface Science: Foundations of Catalysis and Nanoscience*, 3rd ed.; John Wiley & Sons Inc., 2012.
- (48) Eberl, K.; Iyer, S. S.; Zollner, S.; Tsang, J. C.; Legoues, F. K. Growth and Strain Compensation Effects in the Ternary $\text{Si}_{1-x-y}\text{Ge}_x\text{C}_y$ Alloy System. *Appl. Phys. Lett.* **1992**, 60 (24), 3033–3035.
- (49) Oshima, R.; Takata, A.; Okada, Y. Strain-Compensated InAs/GaNAs Quantum Dots for Use in High-Efficiency Solar Cells. *Appl. Phys. Lett.* **2008**, 93 (8), 8–11.
- (50) Doppalapudi, D.; Iliopoulos, E.; Basu, S. N.; Moustakas, T. D. Epitaxial Growth of Gallium Nitride Thin Films on A -Plane Sapphire by Molecular Beam Epitaxy. *J. Appl. Phys.* **1999**, 85 (7), 3582–3589.
- (51) Wang, B.; Caffio, M.; Bromley, C.; Früchtl, H.; Schaub, R. Coupling Epitaxy, Chemical Bonding, and Work Function at the Local Scale in Transition Metal-Supported Graphene. *ACS Nano* **2010**, 4 (10), 5773–5782.
- (52) Gao, M.; Pan, Y.; Huang, L.; Hu, H.; Zhang, L. Z.; Guo, H. M.; Du, S. X.; Gao, H.-J. Epitaxial Growth and Structural Property of Graphene on Pt(111). *Appl. Phys. Lett.* **2011**, 98 (3), 033101.
- (53) Reinhardt, K.; Kern, W. *Handbook of Semiconductor Wafer Cleaning Technology: Science, Technology, and Applications*, 2nd ed.; William Andrew, 2008.
- (54) Koma, A.; Yoshimura, K. Ultrasharp Interfaces Grown with Van Der Waals Epitaxy. *Surf. Sci.* **1986**, 174 (1–3), 556–560.
- (55) Koma, A. Van Der Waals Epitaxy—a New Epitaxial Growth Method for a Highly Lattice-Mismatched System. *Thin Solid Films* **1992**, 216 (1), 72–76.
- (56) Zhang, X.; Meng, F.; Christianson, J. R.; Arroyo-Torres, C.; Lukowski, M. a; Liang, D.; Schmidt, J. R.; Jin, S. Vertical Heterostructures of Layered Metal Chalcogenides by van Der Waals Epitaxy. *Nano Lett.* **2014**, 14 (6), 3047–3054.
- (57) Koma, A. Van Der Waals Epitaxy for Highly Lattice-Mismatched Systems. *J. Cryst. Growth* **1999**, 201–202, 236–241.
- (58) Seyller, T. Passivation of Hexagonal SiC Surfaces by Hydrogen Termination. *J. Phys. Condens. Matter* **2004**, 16 (17), S1755–S1782.
- (59) Seyller, T. Electronic Properties of SiC Surfaces and Interfaces: Some Fundamental and Technological Aspects. *Appl. Phys. A* **2006**, 85 (4), 371–385.

- (60) Levinshtein, M. E.; Rumyantsev, S. L.; Shur, M. S. *Properties of Advanced Semiconductor Materials: GaN, AlN, InN, BN, SiC, SiGe.*; John Wiley & Sons Inc., 2001.
- (61) Kukushkin, S. a.; Osipov, a. V.; Feoktistov, N. a. Synthesis of Epitaxial Silicon Carbide Films through the Substitution of Atoms in the Silicon Crystal Lattice: A Review. *Phys. Solid State* **2014**, *56* (8), 1507–1535.
- (62) Zhuang, D.; Edgar, J. H. Wet Etching of GaN, AlN, and SiC: A Review. *Mater. Sci. Eng. R Reports* **2005**, *48* (1), 1–46.
- (63) Murata, J.; Okamoto, T.; Sadakuni, S.; Hattori, A. N.; Yagi, K.; Sano, Y.; Arima, K.; Yamauchi, K. Atomically Smooth Gallium Nitride Surfaces Prepared by Chemical Etching with Platinum Catalyst in Water. *J. Electrochem. Soc.* **2012**, *159* (4), H417–H420.
- (64) Carmalt, C. J.; Peters, E. S.; Parkin, I. P.; Manning, T. D.; Hector, A. L. Chemical Vapor Deposition of Niobium Disulfide Thin Films. *Eur. J. Inorg. Chem.* **2004**, No. 22, 4470–4476.
- (65) Carmalt, C. J.; Manning, T. D.; Parkin, I. P.; Peters, E. S.; Hector, A. L. Formation of a New (1T) Trigonal NbS₂ Polytype via Atmospheric Pressure Chemical Vapour Deposition. *J. Mater. Chem.* **2004**, *14* (3), 290.
- (66) Ge, W.; Kawahara, K.; Tsuji, M.; Ago, H. Large-Scale Synthesis of NbS₂ Nanosheets with Controlled Orientation on Graphene by Ambient Pressure CVD. *Nanoscale* **2013**, *5* (13), 5773.
- (67) Zhao, S.; Hotta, T.; Koretsune, T.; Watanabe, K.; Taniguchi, T.; Sugawara, K.; Takahashi, T.; Shinohara, H.; Kitaura, R. Two-Dimensional Metallic NbS₂: Growth, Optical Identification and Transport Properties. *2D Mater.* **2016**, *3* (2), 025027.
- (68) Zhou, H.; Wang, C.; Shaw, J. C.; Cheng, R.; Chen, Y.; Huang, X.; Liu, Y.; Weiss, N. O.; Lin, Z.; Huang, Y.; et al. Large Area Growth and Electrical Properties of P-Type WSe₂ Atomic Layers. *Nano Lett.* **2015**, *15* (1), 709–713.
- (69) Koperski, M.; Nogajewski, K.; Arora, A.; Cherkez, V.; Mallet, P.; Veuillen, J.-Y.; Marcus, J.; Kossacki, P.; Potemski, M. Single Photon Emitters in Exfoliated WSe₂ Structures. *Nat. Nanotechnol.* **2015**, *10* (6), 503–506.
- (70) Kittel, C. *Introduction to Solid State Physics*, 8th ed.; John Wiley & Sons Inc., 2005.
- (71) Novoselov, K. S.; Mishchenko, A.; Carvalho, A.; Castro Neto, A. H. 2D Materials and van Der Waals Heterostructures. *Science* **2016**, *353* (6298), aac9439.
- (72) Hong, X.; Kim, J.; Shi, S.; Zhang, Y.; Jin, C.; Sun, Y.; Tongay, S.; Wu, J.; Zhang, Y.; Wang, F. Ultrafast Charge Transfer in Atomically Thin MoS₂/WS₂ Heterostructures. *Nat. Nanotechnol.* **2014**, *9* (9), 682–686.
- (73) Lee, C.-H.; Lee, G.-H.; van der Zande, A. M.; Chen, W.; Li, Y.; Han, M.; Cui, X.; Arefe, G.; Nuckolls, C.; Heinz, T. F.; et al. Atomically Thin P–n Junctions with van Der Waals Heterointerfaces. *Nat. Nanotechnol.* **2014**, *9* (9), 676–681.

- (74) Tongay, S.; Fan, W.; Kang, J.; Park, J.; Koldemir, U.; Suh, J.; Narang, D. S.; Liu, K.; Ji, J.; Li, J.; et al. Tuning Interlayer Coupling in Large-Area Heterostructures with CVD-Grown MoS₂ and WS₂ Monolayers. *Nano Lett.* **2014**, *14* (6), 3185–3190.
- (75) Zhu, X.; Monahan, N. R.; Gong, Z.; Zhu, H.; Williams, K. W.; Nelson, C. A. Charge Transfer Excitons at van Der Waals Interfaces. *J. Am. Chem. Soc.* **2015**, *137* (26), 8313–8320.
- (76) Gong, Y.; Lin, J.; Wang, X.; Shi, G.; Lei, S.; Lin, Z.; Zou, X.; Ye, G.; Vajtai, R.; Yakobson, B. I.; et al. Vertical and In-Plane Heterostructures from WS₂/MoS₂ Monolayers. *Nat. Mater.* **2014**, *13* (12), 1135–1142.
- (77) Zhang, X.; Lin, C.; Tseng, Y.; Huang, K.; Lee, Y. Synthesis of Lateral Heterostructures of Semiconducting Atomic Layers. *Nano Lett.* **2015**, *15* (1), 410–415.
- (78) Levendorf, M. P.; Kim, C. J.; Brown, L.; Huang, P. Y.; Havener, R. W.; Muller, D. A.; Park, J. Graphene and Boron Nitride Lateral Heterostructures for Atomically Thin Circuitry. *Nature* **2012**, *488* (7413), 627–632.
- (79) Liu, L.; Park, J.; Siegel, D. a; McCarty, K. F.; Clark, K. W.; Deng, W.; Basile, L.; Idrobo, J. C.; Li, A.-P.; Gu, G. Heteroepitaxial Growth of Two-Dimensional Hexagonal Boron Nitride Templated by Graphene Edges. *Science* **2014**, *343* (6167), 163–167.
- (80) Chen, L.; He, L.; Wang, H. S.; Wang, H.; Tang, S.; Cong, C.; Xie, H.; Li, L.; Xia, H.; Li, T.; et al. Oriented Graphene Nanoribbons Embedded in Hexagonal Boron Nitride Trenches. *Nat. Commun.* **2017**, *8*, 1–6.
- (81) Kim, S. M.; Hsu, A.; Araujo, P. T.; Lee, Y.-H.; Palacios, T.; Dresselhaus, M.; Idrobo, J.-C.; Kim, K. K.; Kong, J. Synthesis of Patched or Stacked Graphene and HBN Flakes: A Route to Hybrid Structure Discovery. *Nano Lett.* **2013**, *13* (3), 933–941.
- (82) Shin, H.-C.; Jang, Y.; Kim, T.-H.; Lee, J.-H.; Oh, D.-H.; Ahn, S. J.; Lee, J. H.; Moon, Y.; Park, J.-H.; Yoo, S. J.; et al. Epitaxial Growth of a Single-Crystal Hybridized Boron Nitride and Graphene Layer on a Wide-Band Gap Semiconductor. *J. Am. Chem. Soc.* **2015**, *137* (21), 6897–6905.
- (83) Heo, H.; Sung, J. H.; Jin, G.; Ahn, J.-H.; Kim, K.; Lee, M.-J.; Cha, S.; Choi, H.; Jo, M.-H. Rotation-Misfit-Free Heteroepitaxial Stacking and Stitching Growth of Hexagonal Transition-Metal Dichalcogenide Monolayers by Nucleation Kinetics Controls. *Adv. Mater.* **2015**, *27* (25), 3803–3810.
- (84) Yoo, Y.; Degregorio, Z. P.; Johns, J. E. Seed Crystal Homogeneity Controls Lateral and Vertical Heteroepitaxy of Monolayer MoS₂ and WS₂. *J. Am. Chem. Soc.* **2015**, *137* (45), 14281–14287.
- (85) Liu, Y.; Ghosh, R.; Wu, D.; Ismach, A.; Ruoff, R.; Lai, K. Mesoscale Imperfections in MoS₂ Atomic Layers Grown by a Vapor Transport Technique. *Nano Lett.* **2014**, *14* (8), 4682–4686.

- (86) Ling, X.; Lee, Y.-H.; Lin, Y.; Fang, W.; Yu, L.; Dresselhaus, M. S.; Kong, J. Role of the Seeding Promoter in MoS₂ Growth by Chemical Vapor Deposition. *Nano Lett.* **2014**, *14* (2), 464–472.
- (87) Kim, I. S.; Sangwan, V. K.; Jariwala, D.; Wood, J. D.; Park, S.; Chen, K.-S.; Shi, F.; Ruiz-Zepeda, F.; Ponce, A.; Jose-Yacamán, M.; et al. Influence of Stoichiometry on the Optical and Electrical Properties of Chemical Vapor Deposition Derived MoS₂. *ACS Nano* **2014**, *8* (10), 10551–10558.
- (88) Song, I.; Park, C.; Hong, M.; Baik, J.; Shin, H.-J.; Choi, H. C. Patternable Large-Scale Molybdenum Disulfide Atomic Layers Grown by Gold-Assisted Chemical Vapor Deposition. *Angew. Chem. Int. Ed. Engl.* **2014**, *53* (5), 1266–1269.
- (89) Zhang, C.; Johnson, A.; Hsu, C.-L.; Li, L.-J.; Shih, C.-K. Direct Imaging of Band Profile in Single Layer MoS₂ on Graphite: Quasiparticle Energy Gap, Metallic Edge States, and Edge Band Bending. *Nano Lett.* **2014**, *14* (5), 2443–2447.
- (90) Wu, S.; Huang, C.; Aivazian, G.; Ross, J. S.; Cobden, D. H.; Xu, X. Vapor–Solid Growth of High Optical Quality MoS₂ Monolayers with Near-Unity Valley Polarization. *ACS Nano* **2013**, *7* (3), 2768–2772.
- (91) Ji, Q.; Zhang, Y.; Gao, T.; Zhang, Y.; Ma, D.; Liu, M.; Chen, Y.; Qiao, X.; Tan, P.-H.; Kan, M.; et al. Epitaxial Monolayer MoS₂ on Mica with Novel Photoluminescence. *Nano Lett.* **2013**, *13* (8), 3870–3877.
- (92) Wang, X.; Feng, H.; Wu, Y.; Jiao, L. Controlled Synthesis of Highly Crystalline MoS₂ Flakes by Chemical Vapor Deposition. *J. Am. Chem. Soc.* **2013**, *135* (14), 5304–5307.
- (93) Li, H.; Zhang, Q.; Yap, C. C. R.; Tay, B. K.; Edwin, T. H. T.; Olivier, A.; Baillargeat, D. From Bulk to Monolayer MoS₂: Evolution of Raman Scattering. *Adv. Funct. Mater.* **2012**, *22* (7), 1385–1390.
- (94) Chakraborty, B.; Matte, H. S. S. R.; Sood, A. K.; Rao, C. N. R. Layer-Dependent Resonant Raman Scattering of a Few Layer MoS₂. *J. Raman Spectrosc.* **2013**, *44* (1), 92–96.
- (95) Splendiani, A.; Sun, L.; Zhang, Y.; Li, T.; Kim, J.; Chim, C.-Y.; Galli, G.; Wang, F. Emerging Photoluminescence in Monolayer MoS₂. *Nano Lett.* **2010**, *10* (4), 1271–1275.
- (96) Dumcenco, D.; Ovchinnikov, D.; Marinov, K.; Lazić, P.; Gibertini, M.; Marzari, N.; Sanchez, O. L.; Kung, Y.-C.; Krasnozhon, D.; Chen, M.-W.; et al. Large-Area Epitaxial Monolayer MoS₂. *ACS Nano* **2015**, *9* (4), 4611–4620.
- (97) Ji, Q.; Kan, M.; Zhang, Y.; Guo, Y.; Ma, D.; Shi, J.; Sun, Q.; Chen, Q.; Zhang, Y.; Liu, Z. Unravelling Orientation Distribution and Merging Behavior of Monolayer MoS₂ Domains on Sapphire. *Nano Lett.* **2015**, *15* (1), 198–205.
- (98) Ye, M.; Winslow, D.; Zhang, D.; Pandey, R.; Yap, Y. Recent Advancement on the Optical Properties of Two-Dimensional Molybdenum Disulfide (MoS₂) Thin Films. *Photonics* **2015**, *2* (1), 288–307.

- (99) Gutiérrez, H. R.; Perea-López, N.; Elías, A. L.; Berkdemir, A.; Wang, B.; Lv, R.; López-Urías, F.; Crespi, V. H.; Terrones, H.; Terrones, M. Extraordinary Room-Temperature Photoluminescence in Triangular WS₂ Monolayers. *Nano Lett.* **2013**, *13* (8), 3447–3454.
- (100) Liu, Z.; Amani, M.; Najmaei, S.; Xu, Q.; Zou, X.; Zhou, W.; Yu, T.; Qiu, C.; Birdwell, A. G.; Crowne, F. J.; et al. Strain and Structure Heterogeneity in MoS₂ Atomic Layers Grown by Chemical Vapour Deposition. *Nat. Commun.* **2014**, *5* (1), 5246.
- (101) Li, M.-Y.; Shi, Y.; Cheng, C.-C.; Lu, L.-S.; Lin, Y.-C.; Tang, H.-L.; Tsai, M.-L.; Chu, C.-W.; Wei, K.-H.; He, J.-H.; et al. Epitaxial Growth of a Monolayer WSe₂-MoS₂ Lateral p-n Junction with an Atomically Sharp Interface. *Science* **2015**, *349* (6247), 524–528.
- (102) Krivanek, O. L.; Chisholm, M. F.; Nicolosi, V.; Pennycook, T. J.; Corbin, G. J.; Dellby, N.; Murfitt, M. F.; Own, C. S.; Szilagy, Z. S.; Oxley, M. P.; et al. Atom-by-Atom Structural and Chemical Analysis by Annular Dark-Field Electron Microscopy. *Nature* **2010**, *464* (7288), 571–574.
- (103) Yu, Y.; Hu, S.; Su, L.; Huang, L.; Liu, Y.; Jin, Z.; Purezky, A. A.; Geohegan, D. B.; Kim, K. W.; Zhang, Y.; et al. Equally Efficient Interlayer Exciton Relaxation and Improved Absorption in Epitaxial and Nonepitaxial MoS₂/WS₂ Heterostructures. *Nano Lett.* **2015**, *15* (1), 486–491.
- (104) Kim, B.-S.; Kim, E.; Jeon, H.-S.; Lee, H.-I.; Lee, J.-C. Study on the Reduction of Molybdenum Dioxide by Hydrogen. *Mater. Trans.* **2008**, *49* (9), 2147–2152.
- (105) Leisegang, T.; Levin, A. A.; Walter, J.; Meyer, D. C. In Situ X-Ray Analysis of MoO₃ Reduction. *Cryst. Res. Technol.* **2005**, *40* (1–2), 95–105.
- (106) Schulmeyer, W. V.; Ortner, H. M. Mechanisms of the Hydrogen Reduction of Molybdenum Oxides. *Int. J. Refract. Met. Hard Mater.* **2002**, *20* (4), 261–269.
- (107) Yoo, Y.; Seo, K.; Han, S.; Varadwaj, K. S. K.; Kim, H. Y.; Ryu, J. H.; Lee, H. M.; Ahn, J. P.; Ihee, H.; Kim, B. Steering Epitaxial Alignment of Au, Pd, and AuPd Nanowire Arrays by Atom Flux Change. *Nano Lett.* **2010**, *10* (2), 432–438.
- (108) Henry, C. R. Morphology of Supported Nanoparticles. *Prog. Surf. Sci.* **2005**, *80* (3–4), 92–116.
- (109) Helveg, S.; Lauritsen, J. V.; Lægsgaard, E.; Stensgaard, I.; Nørskov, J. K.; Clausen, B. S.; Topsøe, H.; Besenbacher, F. Atomic-Scale Structure of Single-Layer MoS₂ Nanoclusters. *Phys. Rev. Lett.* **2000**, *84* (5), 951–954.
- (110) Bao, W.; Borys, N. J.; Ko, C.; Suh, J.; Fan, W.; Thron, A.; Zhang, Y.; Buyanin, A.; Zhang, J.; Cabrini, S.; et al. Visualizing Nanoscale Excitonic Relaxation Properties of Disordered Edges and Grain Boundaries in Monolayer Molybdenum Disulfide. *Nat. Commun.* **2015**, *6* (1), 7993.
- (111) Zhang, Y.; Zhang, Y.; Ji, Q.; Ju, J.; Yuan, H.; Shi, J.; Gao, T.; Ma, D.; Liu, M.; Chen, Y.; et al. Controlled Growth of High-Quality Monolayer WS₂ Layers on

- Sapphire and Imaging Its Grain Boundary. *ACS Nano* **2013**, 7 (10), 8963–8971.
- (112) Huang, J.-K.; Pu, J.; Hsu, C.-L.; Chiu, M.-H.; Juang, Z.-Y.; Chang, Y.-H.; Chang, W.-H.; Iwasa, Y.; Takenobu, T.; Li, L.-J. Large-Area Synthesis of Highly Crystalline WSe₂ Monolayers and Device Applications. *ACS Nano* **2014**, 8 (1), 923–930.
- (113) Duan, X.; Wang, C.; Pan, A.; Yu, R.; Duan, X. Two-Dimensional Transition Metal Dichalcogenides as Atomically Thin Semiconductors: Opportunities and Challenges. *Chem. Soc. Rev.* **2015**, 44 (24), 8859–8876.
- (114) Tedstone, A. A.; Lewis, D. J.; O'Brien, P. Synthesis, Properties, and Applications of Transition Metal-Doped Layered Transition Metal Dichalcogenides. *Chem. Mater.* **2016**, 28 (7), 1965–1974.
- (115) Akinwande, D.; Petrone, N.; Hone, J. Two-Dimensional Flexible Nanoelectronics. *Nat. Commun.* **2014**, 5 (1), 5678.
- (116) Jariwala, D.; Marks, T. J.; Hersam, M. C. Mixed-Dimensional van Der Waals Heterostructures. *Nat. Mater.* **2017**, 16 (2), 170–181.
- (117) Deng, D.; Novoselov, K. S.; Fu, Q.; Zheng, N.; Tian, Z.; Bao, X. Catalysis with Two-Dimensional Materials and Their Heterostructures. *Nat. Nanotechnol.* **2016**, 11 (3), 218–230.
- (118) Mak, K. F.; Shan, J. Photonics and Optoelectronics of 2D Semiconductor Transition Metal Dichalcogenides. *Nat. Photonics* **2016**, 10 (4), 216–226.
- (119) Lim, H.; Yoon, S. I.; Kim, G.; Jang, A.-R.; Shin, H. S. Stacking of Two-Dimensional Materials in Lateral and Vertical Directions. *Chem. Mater.* **2014**, 26 (17), 4891–4903.
- (120) Wu, C.-C.; Jariwala, D.; Sangwan, V. K.; Marks, T. J.; Hersam, M. C.; Lauhon, L. J. Elucidating the Photoresponse of Ultrathin MoS₂ Field-Effect Transistors by Scanning Photocurrent Microscopy. *J. Phys. Chem. Lett.* **2013**, 4 (15), 2508–2513.
- (121) Behura, S.; Berry, V. Interfacial Nondegenerate Doping of MoS₂ and Other Two-Dimensional Semiconductors. *ACS Nano* **2015**, 9 (3), 2227–2230.
- (122) Komsa, H.-P.; Krasheninnikov, A. V. Two-Dimensional Transition Metal Dichalcogenide Alloys: Stability and Electronic Properties. *J. Phys. Chem. Lett.* **2012**, 3 (23), 3652–3656.
- (123) Kou, L.; Frauenheim, T.; Chen, C. Nanoscale Multilayer Transition-Metal Dichalcogenide Heterostructures: Band Gap Modulation by Interfacial Strain and Spontaneous Polarization. *J. Phys. Chem. Lett.* **2013**, 4 (10), 1730–1736.
- (124) Xi, J.; Zhao, T.; Wang, D.; Shuai, Z. Tunable Electronic Properties of Two-Dimensional Transition Metal Dichalcogenide Alloys: A First-Principles Prediction. *J. Phys. Chem. Lett.* **2014**, 5 (2), 285–291.
- (125) Duerloo, K.-A. N.; Ong, M. T.; Reed, E. J. Intrinsic Piezoelectricity in Two-

Dimensional Materials. *J. Phys. Chem. Lett.* **2012**, *3* (19), 2871–2876.

- (126) Chen, W.; Zhao, J.; Zhang, J.; Gu, L.; Yang, Z.; Li, X.; Yu, H.; Zhu, X.; Yang, R.; Shi, D.; et al. Oxygen-Assisted Chemical Vapor Deposition Growth of Large Single-Crystal and High-Quality Monolayer MoS₂. *J. Am. Chem. Soc.* **2015**, *137* (50), 15632–15635.
- (127) Cong, C.; Shang, J.; Wu, X.; Cao, B.; Peimyoo, N.; Qiu, C.; Sun, L.; Yu, T. Synthesis and Optical Properties of Large-Area Single-Crystalline 2D Semiconductor WS₂ Monolayer from Chemical Vapor Deposition. *Adv. Opt. Mater.* **2014**, *2* (2), 131–136.
- (128) Govind Rajan, A.; Warner, J. H.; Blankschtein, D.; Strano, M. S. Generalized Mechanistic Model for the Chemical Vapor Deposition of 2D Transition Metal Dichalcogenide Monolayers. *ACS Nano* **2016**, *10* (4), 4330–4344.
- (129) Yu, Y.; Li, C.; Liu, Y.; Su, L.; Zhang, Y.; Cao, L. Controlled Scalable Synthesis of Uniform, High-Quality Monolayer and Few-Layer MoS₂ Films. *Sci. Rep.* **2013**, *3* (1), 1866.
- (130) Samad, L.; Bladow, S. M.; Ding, Q.; Zhuo, J.; Jacobberger, R. M.; Arnold, M. S.; Jin, S. Layer-Controlled Chemical Vapor Deposition Growth of MoS₂ Vertical Heterostructures via van Der Waals Epitaxy. *ACS Nano* **2016**, *10* (7), 7039–7046.
- (131) Kong, D.; Wang, H.; Cha, J. J.; Pasta, M.; Koski, K. J.; Yao, J.; Cui, Y. Synthesis of MoS₂ and MoSe₂ Films with Vertically Aligned Layers. *Nano Lett.* **2013**, *13* (3), 1341–1347.
- (132) Kibsgaard, J.; Chen, Z.; Reinecke, B. N.; Jaramillo, T. F. Engineering the Surface Structure of MoS₂ to Preferentially Expose Active Edge Sites for Electrocatalysis. *Nat. Mater.* **2012**, *11* (11), 963–969.
- (133) Liu, Z.; Amani, M.; Najmaei, S.; Xu, Q.; Zou, X.; Zhou, W.; Yu, T.; Qiu, C.; Birdwell, a G.; Crowne, F. J.; et al. Strain and Structure Heterogeneity in MoS₂ Atomic Layers Grown by Chemical Vapour Deposition. *Nat. Commun.* **2014**, *5* (1), 5246.
- (134) Zhang, Q.; Xiao, X.; Zhao, R.; Lv, D.; Xu, G.; Lu, Z.; Sun, L.; Lin, S.; Gao, X.; Zhou, J.; et al. Two-Dimensional Layered Heterostructures Synthesized from Core-Shell Nanowires. *Angew. Chemie Int. Ed.* **2015**, *54* (31), 8957–8960.
- (135) DeGregorio, Z. P.; Yoo, Y.; Johns, J. E. Aligned MoO₂/MoS₂ and MoO₂/MoTe₂ Freestanding Core/Shell Nanoplates Driven by Surface Interactions. *J. Phys. Chem. Lett.* **2017**, *8* (7), 1631–1636.
- (136) Cain, J. D.; Shi, F.; Wu, J.; Dravid, V. P. Growth Mechanism of Transition Metal Dichalcogenide Monolayers: The Role of Self-Seeding Fullerene Nuclei. *ACS Nano* **2016**, *10* (5), 5440–5445.
- (137) Peng, D.-Y.; Zhao, J. Representation of the Vapour Pressures of Sulfur. *J. Chem. Thermodyn.* **2001**, *33* (9), 1121–1131.

- (138) Burton, J. C.; Sun, L.; Pophristic, M.; Lukacs, S. J.; Long, F. H.; Feng, Z. C.; Ferguson, I. T. Spatial Characterization of Doped SiC Wafers by Raman Spectroscopy. *J. Appl. Phys.* **1998**, *84* (11), 6268–6273.
- (139) Dieterle, M.; Mestl, G. Raman Spectroscopy of Molybdenum Oxides. *Phys. Chem. Chem. Phys.* **2002**, *4* (5), 822–826.
- (140) Zhou, L.; Xu, K.; Zubair, A.; Liao, A. D.; Fang, W.; Ouyang, F.; Lee, Y.-H.; Ueno, K.; Saito, R.; Palacios, T.; et al. Large-Area Synthesis of High-Quality Uniform Few-Layer MoTe₂. *J. Am. Chem. Soc.* **2015**, *137* (37), 11892–11895.
- (141) Keum, D. H.; Cho, S.; Kim, J. H.; Choe, D.-H.; Sung, H.-J.; Kan, M.; Kang, H.; Hwang, J.-Y.; Kim, S. W.; Yang, H.; et al. Bandgap Opening in Few-Layered Monoclinic MoTe₂. *Nat. Phys.* **2015**, *11* (6), 482–486.
- (142) Starke, U.; Schardt, J.; Bernhardt, J.; Heinz, K. Reconstructed Oxide Structures Stable in Air: Silicate Monolayers on Hexagonal SiC Surfaces. *J. Vac. Sci. Technol. A Vacuum, Surfaces, Film.* **1999**, *17* (4), 1688–1692.
- (143) Starke, U.; Bernhardt, J.; Schardt, J.; Heinz, K. SiC Surface Reconstruction: Relevancy of Atomic Structure for Growth Technology. *Surf. Rev. Lett.* **1999**, *06* (06), 1129–1141.
- (144) Heinz, K.; Bernhardt, J.; Schardt, J.; Starke, U. Functional Surface Reconstructions of Hexagonal SiC. *J. Phys. Condens. Matter* **2004**, *16* (17), S1705–S1720.
- (145) Wang, H.-C.; He, Y.-T.; Sun, H.-Y.; Qiu, Z.-R.; Xie, D.; Mei, T.; Tin, C. C.; Feng, Z.-C. Temperature Dependence of Raman Scattering in 4H-SiC Films under Different Growth Conditions. *Chinese Phys. Lett.* **2015**, *32* (4), 047801.
- (146) Tsuchida, H.; Kamata, I.; Izumi, K. Si-H Bonds on the 6H-SiC(0001) Surface after H₂ Annealing. *Jpn. J. Appl. Phys.* **1997**, *36* (Part 2, No. 6A), L699–L702.
- (147) Schönfeld, B.; Huang, J. J.; Moss, S. C. Anisotropic Mean-Square Displacements (MSD) in Single-Crystals of 2H- and 3R-MoS₂. *Acta Crystallogr. Sect. B Struct. Sci.* **1983**, *39* (4), 404–407.
- (148) Scanlon, D. O.; Watson, G. W.; Payne, D. J.; Atkinson, G. R.; Egdell, R. G.; Law, D. S. L. Theoretical and Experimental Study of the Electronic Structures of MoO₃ and MoO₂. *J. Phys. Chem. C* **2010**, *114* (10), 4636–4645.
- (149) Chhowalla, M.; Jena, D.; Zhang, H. Two-Dimensional Semiconductors for Transistors. *Nat. Rev. Mater.* **2016**, *1* (11), 16052.
- (150) Morkoç, H.; Strite, S.; Gao, G. B.; Lin, M. E.; Sverdlov, B.; Burns, M. Large-band-gap SiC, III-V Nitride, and II-VI ZnSe-based Semiconductor Device Technologies. *J. Appl. Phys.* **1994**, *76* (3), 1363–1398.
- (151) Casady, J. B.; Johnson, R. W. Status of Silicon Carbide (SiC) as a Wide-Bandgap Semiconductor for High-Temperature Applications: A Review. *Solid. State. Electron.* **1996**, *39* (10), 1409–1422.

- (152) Özgür, Ü.; Alivov, Y. I.; Liu, C.; Teke, A.; Reshchikov, M. A.; Doğan, S.; Avrutin, V.; Cho, S.-J.; Morkoç, H. A Comprehensive Review of ZnO Materials and Devices. *J. Appl. Phys.* **2005**, *98* (4), 041301.
- (153) Cahill, D. G.; Ford, W. K.; Goodson, K. E.; Mahan, G. D.; Majumdar, A.; Maris, H. J.; Merlin, R.; Phillpot, S. R. Nanoscale Thermal Transport. *J. Appl. Phys.* **2003**, *93* (2), 793–818.
- (154) Roy, K.; Mukhopadhyay, S.; Mahmoodi-Meimand, H. Leakage Current Mechanisms and Leakage Reduction Techniques in Deep-Submicrometer CMOS Circuits. *Proc. IEEE* **2003**, *91* (2), 305–327.
- (155) Pop, E. Energy Dissipation and Transport in Nanoscale Devices. *Nano Res.* **2010**, *3* (3), 147–169.
- (156) Allain, A.; Kang, J.; Banerjee, K.; Kis, A. Electrical Contacts to Two-Dimensional Semiconductors. *Nat. Mater.* **2015**, *14* (12), 1195–1205.
- (157) Wang, L.; Meric, I.; Huang, P. Y.; Gao, Q.; Gao, Y.; Tran, H.; Taniguchi, T.; Watanabe, K.; Campos, L. M.; Muller, D. A.; et al. One-Dimensional Electrical Contact to a Two-Dimensional Material. *Science* **2013**, *342* (6158), 614–617.
- (158) Khatami, Y.; Li, H.; Xu, C.; Banerjee, K. Metal-to-Multilayer-Graphene Contact—Part I: Contact Resistance Modeling. *IEEE Trans. Electron Devices* **2012**, *59* (9), 2444–2452.
- (159) Khatami, Y.; Li, H.; Xu, C.; Banerjee, K. Metal-to-Multilayer-Graphene Contact—Part II: Analysis of Contact Resistance. *IEEE Trans. Electron Devices* **2012**, *59* (9), 2453–2460.
- (160) Lv, R.; Robinson, J. A.; Schaak, R. E.; Sun, D.; Sun, Y.; Mallouk, T. E.; Terrones, M. Transition Metal Dichalcogenides and Beyond: Synthesis, Properties, and Applications of Single- and Few-Layer Nanosheets. *Acc. Chem. Res.* **2015**, *48* (1), 56–64.
- (161) Kappera, R.; Voiry, D.; Yalcin, S. E.; Branch, B.; Gupta, G.; Mohite, A. D.; Chhowalla, M. Phase-Engineered Low-Resistance Contacts for Ultrathin MoS₂ Transistors. *Nat. Mater.* **2014**, *13* (12), 1128–1134.
- (162) Duerloo, K.-A. N.; Li, Y.; Reed, E. J. Structural Phase Transitions in Two-Dimensional Mo- and W-Dichalcogenide Monolayers. *Nat. Commun.* **2014**, *5* (1), 4214.
- (163) Tang, Q.; Jiang, D. Stabilization and Band-Gap Tuning of the 1T-MoS₂ Monolayer by Covalent Functionalization. *Chem. Mater.* **2015**, *27* (10), 3743–3748.
- (164) Ruppert, C.; Aslan, O. B.; Heinz, T. F. Optical Properties and Band Gap of Single- and Few-Layer MoTe₂ Crystals. *Nano Lett.* **2014**, *14* (11), 6231–6236.
- (165) Arora, A.; Schmidt, R.; Schneider, R.; Molas, M. R.; Breslavetz, I.; Potemski, M.; Bratschitsch, R. Valley Zeeman Splitting and Valley Polarization of Neutral and Charged Excitons in Monolayer MoTe₂ at High Magnetic Fields. *Nano Lett.* **2016**,

16 (6), 3624–3629.

- (166) Lezama, I. G.; Arora, A.; Ubaldini, A.; Barreteau, C.; Giannini, E.; Potemski, M.; Morpurgo, A. F. Indirect-to-Direct Band Gap Crossover in Few-Layer MoTe₂. *Nano Lett.* **2015**, *15* (4), 2336–2342.
- (167) Zhang, Q.; Yang, S. A.; Mi, W.; Cheng, Y.; Schwingenschlögl, U. Large Spin-Valley Polarization in Monolayer MoTe₂ on Top of EuO(111). *Adv. Mater.* **2016**, *28* (5), 959–966.
- (168) Cho, S.; Kim, S.; Kim, J. H.; Zhao, J.; Seok, J.; Keum, D. H.; Baik, J.; Choe, D.-H.; Chang, K. J.; Suenaga, K.; et al. Phase Patterning for Ohmic Homojunction Contact in MoTe₂. *Science* **2015**, *349* (6248), 625–628.
- (169) Song, S.; Keum, D. H.; Cho, S.; Perello, D.; Kim, Y.; Lee, Y. H. Room Temperature Semiconductor–Metal Transition of MoTe₂ Thin Films Engineered by Strain. *Nano Lett.* **2016**, *16* (1), 188–193.
- (170) Huang, L.; McCormick, T. M.; Ochi, M.; Zhao, Z.; Suzuki, M.-T.; Arita, R.; Wu, Y.; Mou, D.; Cao, H.; Yan, J.; et al. Spectroscopic Evidence for a Type II Weyl Semimetallic State in MoTe₂. *Nat. Mater.* **2016**, *15* (11), 1155–1160.
- (171) Guimarães, M. H. D.; Gao, H.; Han, Y.; Kang, K.; Xie, S.; Kim, C.-J.; Muller, D. A.; Ralph, D. C.; Park, J. Atomically Thin Ohmic Edge Contacts Between Two-Dimensional Materials. *ACS Nano* **2016**, *10* (6), 6392–6399.
- (172) Yoo, Y.; DeGregorio, Z. P.; Su, Y.; Koester, S. J.; Johns, J. E. In-Plane 2H-1T' MoTe₂ Homojunctions Synthesized by Flux-Controlled Phase Engineering. *Adv. Mater.* **2017**, *29* (16), 1605461.
- (173) Xie, S.; Tu, L.; Han, Y.; Huang, L.; Kang, K.; Lao, K. U.; Jr, R. A. D.; Park, J. Coherent, Atomically Thin Transition-Metal Dichalcogenide Superlattices with Engineered Strain. **2018**, *1136* (March), 1131–1136.
- (174) Kang, K.; Lee, K. H.; Han, Y.; Gao, H.; Xie, S.; Muller, D. A.; Park, J. Layer-by-Layer Assembly of Two-Dimensional Materials into Wafer-Scale Heterostructures. *Nature* **2017**, *550* (7675), 229–233.
- (175) Ling, X.; Lin, Y.; Ma, Q.; Wang, Z.; Song, Y.; Yu, L.; Huang, S.; Fang, W.; Zhang, X.; Hsu, A. L.; et al. Parallel Stitching of 2D Materials. *Adv. Mater.* **2016**, *28* (12), 2322–2329.
- (176) Naylor, C. H.; Parkin, W. M.; Gao, Z.; Berry, J.; Zhou, S.; Zhang, Q.; McClimon, J. B.; Tan, L. Z.; Kehayias, C. E.; Zhao, M.-Q.; et al. Synthesis and Physical Properties of Phase-Engineered Transition Metal Dichalcogenide Monolayer Heterostructures. *ACS Nano* **2017**, *11* (9), 8619–8627.
- (177) Fisher, W. G.; Sienko, M. J. Stoichiometry, Structure, and Physical Properties of Niobium Disulfide. *Inorg. Chem.* **1980**, *19* (1), 39–43.
- (178) Seguini, G.; Llamoya Curi, J.; Spiga, S.; Tallarida, G.; Wiemer, C.; Perego, M. Solid-State Dewetting of Ultra-Thin Au Films on SiO₂ and HfO₂. *Nanotechnology* **2014**,

25 (49), 495603.

- (179) Naylor, C. H.; Parkin, W. M.; Ping, J.; Gao, Z.; Zhou, Y. R.; Kim, Y.; Streller, F.; Carpick, R. W.; Rappe, A. M.; Drndić, M.; et al. Monolayer Single-Crystal 1T'-MoTe₂ Grown by Chemical Vapor Deposition Exhibits Weak Antilocalization Effect. *Nano Lett.* **2016**, *16* (7), 4297–4304.
- (180) Chen, S.-Y.; Goldstein, T.; Venkataraman, D.; Ramasubramaniam, A.; Yan, J. Activation of New Raman Modes by Inversion Symmetry Breaking in Type II Weyl Semimetal Candidate T'-MoTe₂. *Nano Lett.* **2016**, *16* (9), 5852–5860.
- (181) Li, H.; Tsai, C.; Koh, A. L.; Cai, L.; Contryman, A. W.; Fragapane, A. H.; Zhao, J.; Han, H. S.; Manoharan, H. C.; Abild-Pedersen, F.; et al. Activating and Optimizing MoS₂ Basal Planes for Hydrogen Evolution through the Formation of Strained Sulphur Vacancies. *Nat. Mater.* **2016**, *15* (1), 48–53.
- (182) Zhou, L.; Zubair, A.; Wang, Z.; Zhang, X.; Ouyang, F.; Xu, K.; Fang, W.; Ueno, K.; Li, J.; Palacios, T.; et al. Synthesis of High-Quality Large-Area Homogenous 1T' MoTe₂ from Chemical Vapor Deposition. *Adv. Mater.* **2016**, *28* (43), 9526–9531.
- (183) Brooks, L. S. The Vapor Pressures of Tellurium and Selenium. *J. Am. Chem. Soc.* **1952**, *74* (1), 227–229.
- (184) Neff, J. L.; Rahe, P. Insights into Kelvin Probe Force Microscopy Data of Insulator-Supported Molecules. *Phys. Rev. B* **2015**, *91* (8), 085424.
- (185) Pour, N. H.; Anugrah, Y.; Wu, S.; Xu, X.; Koester, S. J. Chemical Doping for Threshold Control and Contact Resistance Reduction in Graphene and MoS₂ Field Effect Transistors. In *71st Device Research Conference*; IEEE, 2013; pp 101–102.
- (186) Fathipour, S.; Ma, N.; Hwang, W. S.; Protasenko, V.; Vishwanath, S.; Xing, H. G.; Xu, H.; Jena, D.; Appenzeller, J.; Seabaugh, A. Exfoliated Multilayer MoTe₂ Field-Effect Transistors. *Appl. Phys. Lett.* **2014**, *105* (19), 192101.
- (187) Kim, C.; Moon, I.; Lee, D.; Choi, M. S.; Ahmed, F.; Nam, S.; Cho, Y.; Shin, H.; Park, S.; Yoo, W. J. Fermi Level Pinning at Electrical Metal Contacts of Monolayer Molybdenum Dichalcogenides. *ACS Nano* **2017**, *11* (2), 1588–1596.
- (188) Mott, N. F. The Theory of Crystal Rectifiers. *Proc. R. Soc. A Math. Phys. Eng. Sci.* **1939**, *171* (944), 27–38.
- (189) Zhang, J.; Xie, W.; Zhao, J.; Zhang, S. Band Alignment of Two-Dimensional Lateral Heterostructures. *2D Mater.* **2016**, *4* (1), 015038.
- (190) Berkdemir, A.; Gutiérrez, H. R.; Botello-Méndez, A. R.; Perea-López, N.; Elías, A. L.; Chia, C.-I.; Wang, B.; Crespi, V. H.; López-Urías, F.; Charlier, J.-C.; et al. Identification of Individual and Few Layers of WS₂ Using Raman Spectroscopy. *Sci. Rep.* **2013**, *3* (1), 1755.
- (191) McMullan, W. G.; Irwin, J. C. Raman Scattering from 2H and 3R-NbS₂. *Solid State Commun.* **1983**, *45* (7), 557–560.

- (192) Carmalt, C.; Peters, E.; Parkin, I.; Manning, T.; Hector, A. Chemical Vapor Deposition of Niobium Disulfide Thin Films. *Eur. J. Inorg. Chem.* **2004**, 2004 (22), 4470–4476.
- (193) Farmanbar, M.; Brocks, G. Ohmic Contacts to 2D Semiconductors through van Der Waals Bonding. *Adv. Electron. Mater.* **2016**, 2 (4), 1500405.
- (194) Peimyoo, N.; Shang, J.; Cong, C.; Shen, X.; Wu, X.; Yeow, E. K. L.; Yu, T. Nonblinking, Intense Two-Dimensional Light Emitter: Monolayer WS₂ Triangles. *ACS Nano* **2013**, 7 (12), 10985–10994.
- (195) Sun, Q. C.; Yadgarov, L.; Rosentsveig, R.; Seifert, G.; Tenne, R.; Musfeldt, J. L. Observation of a Burstein–Moss Shift in Rhenium-Doped MoS₂ Nanoparticles. *ACS Nano* **2013**, 7 (4), 3506–3511.
- (196) Kumar, P.; Chatterjee, D.; Maeda, T.; Roy, A.; Kaneko, K.; Balakrishnan, V. Scalable Faceted Voids with Luminescent Enhanced Edges in WS₂ Monolayers. *Nanoscale* **2018**.

Appendix A

MATLAB Script for HRTEM Diffusion Analysis

A.1 HRTEM Diffusion Analysis MATLAB Script

```
line_x_min=(pixel_nm_conv).*((height-line_pixels(1,2))./m)+line_pixels(1,1);
line_x_max=(pixel_nm_conv).*((-line_pixels(1,2))./m)+line_pixels(1,1);
line_width=((line_x_max)-(line_x_min));
height_nm=height*(pixel_nm_conv);
width_nm=width*(pixel_nm_conv);
line_length=sqrt(((height_nm).^2)+(line_width.^2));
step=1;
%in units of nm
start=-25;
finish=25;
total_steps=((finish)-(start))./(step);
area_atom_nm=(3.16^2)*(10^-2);
%in units of nm^2/atom
area_atom_cm=(3.16^2)*(10^-16);
%in units of cm^2/atom

for iii = 1:((finish)-(start))./(step));
    step_width=((step).*(line_length))./(height_nm);
    x_bot_coord(1,iii)=(line_x_min)+((start)-(step)).*(step_width)./(step)...
    ...)+(iii.*(step_width));
    x_top_coord(1,iii)=(line_x_max)+((start)-(step)).*(step_width)./(step)...
    ...)+(iii.*(step_width));
    if (x_bot_coord(1,iii) > 0 & (x_top_coord(1,iii) < (width_nm));
        area(1,iii)=(step).*(line_length);
    elseif (x_bot_coord(1,iii) < 0 & (abs(x_bot_coord(1,iii))) < (step);
        side_y_coord_l=m.*(-x_bot_coord(1,iii))+(height_nm);
        area(1,iii)=((step).*(line_length))-((0.5).*(step)-(abs(...
        ...x_bot_coord(1,iii))))*(height_nm)-(side_y_coord_l));
    elseif (x_bot_coord(1,iii) < 0 & (abs(x_bot_coord(1,iii))) > (step);
        y_bot_coord_l(1,iii)=m.*(-x_bot_coord(1,iii)+(step))+(height_nm);
        y_top_coord_l(1,iii)=m.*(-x_bot_coord(1,iii)+(height_nm);
        top_diag=sqrt(((x_top_coord(1,iii)).^2)+((-y_top_coord_l(1,iii)...
        ...).^2));
        bot_diag=sqrt(((x_top_coord(1,iii)+(step)).^2)+((-...
        ...y_bot_coord_l(1,iii)).^2));
        area(1,iii)=((0.5).*(step).*(top_diag)+(bot_diag));
    elseif (x_bot_coord(1,iii) < 0 & (abs(x_top_coord(1,iii))) < (step);
        area(1,iii)=(0.5).*(abs(x_top_coord(1,iii))).*(abs...
        ... (y_top_coord_l(1,iii)));
    elseif (x_top_coord(1,iii) > (width_nm) & (abs((x_top_coord(1,iii))-...
    ... (width_nm))) < (step);
        side_y_coord_r=m.*((width_nm)-x_top_coord(1,iii));
        area(1,iii)=((step).*(line_length))-((0.5).*(abs(x_top_coord...
        ... (1,iii)-(width_nm))).*(side_y_coord_r));
    elseif (x_top_coord(1,iii) > (width_nm) & (abs((height_nm)-...
    ...x_bot_coord(1,iii))) < (step);
        y_top_coord_r(1,iii)=m.*((width_nm)-x_top_coord(1,iii)+(step));
        area(1,iii)=(0.5).*(abs((width_nm)-x_bot_coord(1,iii))).*(abs...
        ... ((height_nm)-y_top_coord_r(1,iii)));
    elseif (x_top_coord(1,iii) > (width_nm) & (abs((x_top_coord(1,iii))-...
    ... (width_nm))) > (step);
        y_top_coord_r(1,iii)=m.*((width_nm)-x_top_coord(1,iii)+(step));
        y_bot_coord_r(1,iii)=m.*((width_nm)-x_top_coord(1,iii));
        top_diag=sqrt(((width_nm)-x_bot_coord(1,iii)).^2)+...
        ... ((y_top_coord_r(1,iii)-(height_nm)).^2));
        bot_diag=sqrt(((width_nm)-x_bot_coord(1,iii)+(step)).^2)+...
        ... ((y_bot_coord_r(1,iii)-(height_nm)).^2));
        area(1,iii)=((0.5).*(step).*(top_diag)+(bot_diag));
    else
        area(1,iii)=0;
```

```

end
end

d_l=csvread('8_1_d_left_6-9-15.csv');
d_r=csvread('8_1_d_right_6-9-15.csv');
edges_l=[(start):(step):0];
edges_r=[0:(step):(finish)];
xaxis=[((start)+((step)./2)):(step):(((finish)-(step))+((step)./2))];
[h_l,edges_l]=histcounts(d_l,edges_l);
[h_r,edges_r]=histcounts(d_r,edges_r);
all_counted=cat(2,h_l,h_r);
for iii = 1:((finish)-(start))./(step);
    if iii <= ((-start)./(step));
        h_l_norm(iii)=(1/(area_atom_cm))-(h_l(iii).*(10^14)./(area(1,iii)));
    elseif iii > ((-start)./(step)) & iii <= ((finish-start)./(step));
        h_r_norm(iii+((start)./(step)))=(h_r(iii+((start)./(step))...
        ... (step))).*(10^14)./(area(1,iii)));
    else
        h_wrong=(area(1,iii))
    end
end
end
h_combined=cat(2,h_l_norm,h_r_norm);
error=sqrt((all_counted.*(10^14))./(area(1,iii)));
errorbar(xaxis,h_combined,error,'-o')
xlabel('Distance (nm)')
ylabel('Concentration (atoms/cm^2)')
hold on;
h_l_norm_atom2=(1/(area_atom_cm))-h_l_norm;
h_r_norm_atom2=(1/(area_atom_cm))-h_r_norm;
h_combined_atom2=cat(2,h_l_norm_atom2,h_r_norm_atom2);
errorbar(xaxis,h_combined_atom2,error,'-o')
legend({'[W]', '[Mo]'}, 'FontSize', 12, 'Location', 'northwest')

```